

**From Well Log to Formation Model: A Novel Laboratory Calibrated Methodology with
Demonstration**

by

Margaret Bengé

BS and MS in Mechanical Engineering, Baylor University, 2014

PhD in Civil/Materials Engineering, University of Pittsburgh

Submitted to the Graduate Faculty of the
Swanson School of Engineering in partial fulfillment
of the requirements for the degree of
Doctor of Philosophy

University of Pittsburgh

2023

UNIVERSITY OF PITTSBURGH
SWANSON SCHOOL OF ENGINEERING

This thesis was presented

by

Margaret Bengé

It was defended on

October 31, 2023

and approved by

Dr John Brigham, Associate Professor, Civil & Environmental Engineering

Dr Jeen-Shang Lin, Associate Professor, Civil & Environmental Engineering

Dr William Harbert, Professor, Geology & Environmental Science

Dissertation Director: Dr Andrew P Bungler, Associate Professor and Director of Graduate
Studies, Civil & Environmental Engineering, Chemical & Petroleum Engineering

Copyright © by Margaret Benge

2023

From Well Log to Formation Model: A Novel Laboratory Calibrated Methodology with Demonstration

Margaret Bengé, PhD

University of Pittsburgh, 2023

This work demonstrates how the characterization and modeling of both elastic and creep properties are essential to describe zones in layered rock formations as either low-stress targets for stimulation or high-stress barriers to fracture growth. Prediction of fracture height is critical for designing stimulation operations in oil and gas wells. Ideally, fractures are placed in target zones which will produce hydrocarbons and should not propagate into zones expected to be unproductive or to produce unwanted fluids such as water which in turn must be treated and/or disposed. The essential task in designing stimulation plans is predicting which zones have low horizontal stresses and which will be high-stress barriers to fracture growth. Despite this importance, there are gaps in current knowledge and a complete workflow from laboratory characterization to a finite element model which includes time-dependent rock deformation is required.

While the research and methodology presented here also have application to CO₂ or hydrogen storage, wastewater injection, and geothermal applications, the focus will be on hydrocarbon extraction. This thesis presents the results of a characterization-to-prediction workflow for the Caney shale, which is an emerging hydrocarbon resource in Oklahoma, USA. It begins with an investigation to enable critical evaluation of the Caney zonation into nominally “brittle” and “ductile” zones based on properties observed from well logs. It shows none of the zones are consistently “brittle” or “ductile” mechanical behavior based on the variety of definitions of these terms. However, the nominally ductile zones are weaker and more prone to creep.

A laboratory investigation of samples including strength, elastic, and creep properties, is then used in a finite element model of stress evolution. The model includes both elastic deformation and viscoplastic creep. Results predict the least creep-prone layers to have the lowest horizontal stresses, therefore comprising hydraulic fracturing targets. The most creep-prone layers attain a horizontal stress similar to the vertical stress and therefore are predicted to be high-stress barriers to hydraulic fracture stimulation. In addition to defining stimulation target intervals, the model shows how as tectonic strain rate increases, there is a transition from creep-dominated stresses to stresses dominated by elasticity.

Table of Contents

Preface.....	xvi
1.0 Introduction.....	1
1.1 Fracture Growth and Propagation.....	3
1.2 Current Practices.....	6
1.2.1 Brittleness Index.....	6
1.2.2 In-Situ Stress Prediction.....	7
1.3 Problem Statement and Structure	8
2.0 Experimental Procedures.....	11
2.1 Sample Description.....	11
2.2 Test Procedures	13
2.2.1 Unconfined Compressive Strength	13
2.2.2 Indirect Tensile Strength.....	13
2.2.3 Fracture Toughness	15
2.2.4 Creep and Triaxial Testing Sample Preparation	17
2.2.5 Single-Stage Triaxial Testing	19
2.2.6 Creep Testing.....	23
2.2.7 Young’s Modulus Determination from Creep Testing.....	26
3.0 Brittleness Index and Mechanical Behavior.....	29
3.1 Abstract	Error! Bookmark not defined.
3.2 Introduction	31
3.3 Log Analysis and Sample Quality Control.....	33

3.4 Characterization Methods	35
3.4.1 Mineralogy	35
3.4.2 Strength Tests at Ambient Conditions	35
3.4.3 Triaxial Tests at 90°C	37
3.5 Results.....	39
3.5.1 Mineralogy	39
3.5.2 Strength Tests at Ambient Conditions	40
3.5.3 Triaxial Properties	41
3.6 Brittleness Index	43
3.7 Discussion	47
3.8 Conclusions	51
4.0 Creep Properties and Proppant Embedment.....	54
4.1 Abstract	Error! Bookmark not defined.
4.2 Introduction	56
4.3 Core Description.....	59
4.3.1 Well Location and Sampling Program.....	59
4.3.2 Mineralogy and Microstructure	64
4.4 Rock Mechanical Properties.....	72
4.5 Creep Compliance	77
4.5.1 Reservoir 1	80
4.5.2 Reservoir 2	81
4.5.3 Reservoir 3	82
4.5.4 Ductile 1 and Ductile 2.....	82

4.5.5 Creep Compliance Calculation	82
4.6 Simulation of Proppant Embedment	86
4.7 Discussion	92
4.8 Conclusions	97
4.9 Creep Testing of Additional Orientations	99
4.9.1 Creep of Horizontal Samples	99
4.9.2 Creep of 45° Samples	101
4.9.3 Creep Behavior and Bedding Plane Orientation	102
4.9.4 Long-Term Deformation of Horizontal Samples	103
4.9.5 Long-Term Deformation of 45° Samples	105
4.9.6 Creep and Bedding Planes	108
5.0 Formation Stress Model	110
5.1 Introduction	110
5.2 Background	111
5.3 Baseline Geomechanical Model	113
5.3.1 Model Assumptions	114
5.3.2 Formation Stress Model Setup	116
5.3.3 Formation Model Verification	121
5.4 Inclusion of Tectonic Strains	123
5.5 Inclusion of Creep in Geomechanical Model	126
5.5.1 Analytical Creep Model	127
5.5.1.1 Parameters for Analytical Creep Model	129
5.5.1.2 Analytical Prediction of In-Situ Stresses	131

5.5.2 Finite Element Simulation	133
5.5.2.1 Laboratory Scale Model and Creep Parameter Calibration	135
5.5.2.2 Influence of Creep on Formation Model	140
5.5.2.3 Impact of Tectonic Strain Magnitude and Application Rate	142
5.5.2.4 Conclusions of Finite Element Model	155
5.6 Conclusions	156
6.0 Conclusions and Future Work.....	160
6.1 Brittleness Index	160
6.2 Creep Behavior	161
6.3 Formation Stress Modeling	162
6.4 Workflow and Global Impact.....	163
6.5 Closing Remarks.....	164
6.6 Future Work	165
7.0 Bibliography	167

List of Tables

Table 1 Brittleness Indices and Irwin length for each formation, triaxial test results values are taken from 20.7 MPa (3000 psi) confinement	45
Table 2 Expected confined compressive strength at 20.7 MPa confinement, shown with applied axial stress during creep testing	79
Table 3 Power-Law creep model parameters, valid for stresses in MPa and time in seconds	85
Table 4 Formation model input parameters for each zone.....	121
Table 5: Horizontal creep parameters calculated without elastic strain offset.....	130
Table 6 Creep values adjusted to match laboratory results	139

List of Figures

Figure 1 Illustration of fracture growth patterns due to (A) a uniform stress field and (b) a variable stress field (based on Economides and Nolte, 1987)	5
Figure 2 Tensile sample loaded in frame	14
Figure 3 Fracture toughness sample with dimensions marked	15
Figure 4 Fracture testing sample placed in load frame.....	16
Figure 5 Post-Test photograph demonstrating placement of sensors and filter paper	18
Figure 6 Schematic of triaxial test cell (heated externally) (from Bengte et al., 2023)	19
Figure 7 Hoek cell placed in instron load frame with heating tape, data acquisition wires, and connection to ISCO pump (modified from Bengte et al., 2023).....	20
Figure 8 Dynamic and static Young’s modulus and Poisson’s ratio from average of well log and 20.7 MPa (3000 psi) traixial testing.....	22
Figure 9 Diagram of applied axial stress during creep testing	26
Figure 10 Young’s modulus values for different sample orientations, from first 12-hour load stage of creep testing.....	28
Figure 11 Example photograph of 1/3 core from Reservoir 1	34
Figure 12 Example CT images from Reservoir 1 (left), Ductile 1 (center), and Reservoir 3 (right)	34
Figure 13 Orientation of bedding planes and indication of loading directions for (A) compressive (B) tensile and (C) fracture testing	36
Figure 14 Schematic of triaxial test cell (heated externally) (from Bengte et al., 2023)	37
Figure 15 Ternary diagram of caney sample mineralogy	39

Figure 16 Summary graphs of unconfined properties.....	40
Figure 17 Axial failure stress vs confining stress for all zones (A) and average properties for each zone (B).....	42
Figure 18 Example tests with plastic axial strain ($\epsilon_{plastic}$), and total axial strain ϵ_{total}, for (A) Reservoir 2 and (B) Ductile 1 tested at 20.7 MPa (3000 psi) confining pressure	44
Figure 19 Cross-Plot of various Brittleness Index values, noting the relative Irwin Length gives the absolute value of the difference between the Irwin Length and the smallest Irwin Length, normalized by the difference between maximum and minimum Irwin Length, mapping to the range 0 to 1 with 1 being the most brittle	51
Figure 20 Well log with identified zones indicated by different colored name boxes, note the variation in Poisson’s ratio between the Ductile and Reservoir zones.....	61
Figure 21 Photographic images of the section of 10.2 cm core sampled by core plugging for each zone along with X-Ray computer tomography scans of example 30 mm diameter core plugs used for quality control during sample preparation	63
Figure 22 Mineralogical composition of the Caney shale samples in the identified zones...	65
Figure 23 Reservoir 1 SEM backscatter electron (BSE) micrographs at 20 kV and 1000 X magnification	67
Figure 24 Ductile 1 SEM backscatter electron (BSE) micrograph at 20 kV and 1000 X magnification.....	68
Figure 25 Reservoir 2 SEM backscatter electron (BSE) micrograph at 20 kV and 1000 X magnification.....	69
Figure 26 Ductile 2 SEM backscatter electron (BSE) micrograph at 20k V and 1000 X magnification.....	70

Figure 27 Reservoir 3 SEM backscatter electron (BSE) micrograph at 20kV and 1000X magnification	71
Figure 28 (A) Diagram of Hoek triaxial cell experimental setup and (B) cell set in load frame with heating tape wrapped around cell (external LVDTs not shown).....	73
Figure 29 Stress vs axial strain (solid) and radial strain (dashed) for (A) 10.5 Mpa and (B) 20.7 MPa confined (1500 and 3000 psi) samples	75
Figure 30: Average Young’s modulus at 20.7 Mpa (MPa), average Poisson’s ratio at 20.7 MPa (-), tangent of friction angle (-), and Cohesion (kpsi) for each zone as calculated from triaxial results	76
Figure 31 Axial stress for each zone at various confining pressures with linear fit shown to calculate friction angle and cohesion.....	77
Figure 32 Evolution of compliance (total axial strain divided by deviatoric stress) from creep tests.....	80
Figure 33 (A) Creep compliance (axial creep strain divided by deviatoric stress) as a function of time, with power law fitted equations and (B) power law fit equations extended to five years	84
Figure 34 Axisymmetric model geometry with boundary conditions and mesh discretization applied for modeling proppant embedment and fracture closure	88
Figure 35 Simulation results of elasto-plastic and creep compaction with calculated fracture aperture evolution as a result of proppant embedment for Reservoir 2 and Ductile 1 properties	89
Figure 36 Simulation results of proppant embedment after elasto-plastic and five years of creep compaction for (A) Reservoir 2 properties and (B) Ductile 1 properties	90

Figure 37 Fracture opening width for Ductile 1 formation and 0.15 mm diameter proppant, plotted as a function of time with diagrams of final fracture geometry after 5 years of simulated time	91
Figure 38 Simulation results of two different proppant diameters (0.15 and 0.30 mm) and with proppant spacing twice the proppant diameter for the case of Ductile 1 properties	92
Figure 39 Creep compliance over time for horizontal samples	100
Figure 40 Creep compliance over time for 45° samples	101
Figure 41 Power-Law fit to horizontal samples	104
Figure 42 Predicted creep compliance for horizontal samples over five years	105
Figure 43 Power-Law fit to 45° samples	106
Figure 44 Predicted creep compliance for 45° samples over five years	107
Figure 45 (A) Analog formation stress model colored by zone and (B) the mesh used in the analysis of the analog formation model	117
Figure 46 Diagram of formation stress model boundary conditions	118
Figure 47 Highlighted nodes used for analysis to determine stress with respect to depth through the formation	120
Figure 48 Verification of initial horizontal stress for baseline geomechanical model.....	122
Figure 49 Recovery of Young’s modulus values for baseline geomechanical model.....	123
Figure 50 Baseline geomechanical finite element models with 100 and 1,000 μstrain for vertical (dashed) and horizontal (solid) properties.....	124
Figure 51 Example calculation of creep parameters without elastic offset (horizontal samples).....	130

Figure 52 Predicted horizontal stress ranges for analytical model with various stress ratios, maximum stress (dark) and minimum stress (light) plotted with vertical stress....	132
Figure 53 Validation of vertical creep model using laboratory scale model	137
Figure 54 Validation of horizontal creep model using laboratory scale model.....	138
Figure 55 Comparison of horizontal (solid) and vertical (dashed) models with and without creep with 100 μstrain applied.....	141
Figure 56 Final horizontal stresses influenced by tectonic strain.....	143
Figure 57 Stress development over time for 100 μstrain model simulated over 350 million years, (A) with logarithmic time scale and (B) with linear time scale.....	146
Figure 58 Stress development over time for 1000 μstrain model simulated over 350 million years, (A) with logarithmic time scale and (B) with linear time scale.....	148
Figure 59 Final horizontal stresses influenced by tectonic strain and time, simulated for 350 million years (solid) and 3.5 million years (dashed).....	150
Figure 60 Stress development over time for 100 μstrain model simulated over 3.5 million years, (A) with logarithmic time scale and (B) with linear time scale.....	152
Figure 61 Stress development over time for 1000 μstrain model simulated over 3.5 million years, (A) with logarithmic time scale and (B) with linear time scale.....	154

Preface

This thesis is dedicated to my family and friends. Without their support I would not have completed my degree. Specifically I would like to thank my parents, who have been supportive of me my entire life. I also want to thank my fellow graduate students, Katelyn Kosar, Basher El-Hajj, Delal Gunaydin, and Yunxing Lu.

Thank you to the faculty and staff of the University of Pittsburgh. Dr Bungler, who has been not only an advisor but a mentor to me. Scooter Hagar, who taught me how to safely operate the equipment in the lab and gave me the knowledge to start diagnosing issues with equipment and the confidence to perform repairs. Cheryl Morand, Alisia Grogan, Cheryl Paul, and all the office staff who help the graduate students with so many things.

Special thanks to the collaborators on this project, Dr Radonjic from Oklahoma State University and Jonny Rutqvist from LBNL. Also thank you to all the faculty and students who have worked together to finish this project.

This project was funded by the United States Department of Energy's Office of Fossil Energy and Carbon Management under Cooperative Agreement DE-FE0031776 and DE-AC02-05CH11231. Recognition of copyright to Springer and the American Rock Mechanics Association for portions of Chapters 3 and 4. Thank you for allowing me to reproduce these papers in this thesis.

1.0 Introduction

To extract hydrocarbons from formations deep in the earth, the only viable method available is to drill a well into the formation. For some formations, where the rock itself is permeable and there is sufficient pressure in the formation to drive the flow of hydrocarbons, simply drilling a well in the correct location is sufficient to extract hydrocarbons. However, stimulation in the form of hydraulic fracturing can be used to improve the rate of hydrocarbon extraction and can be used in formations with extremely low permeability where otherwise hydrocarbons would not be able to be extracted. Therefore, analysis and prediction of fracture growth and orientation are vital to improve hydrocarbon extraction.

A major factor in predicting fracture growth for stimulation are the in-situ stresses in the formation. Fractures will preferentially grow in formations with lower stresses (see for example Nolte and Smith, 1981). An example of this would be if a fracture initiated in one zone will propagate approximately uniformly until it contacts another zone with lower stress. Once the fracture reaches the lower stress zone, growth in the higher-stress zone will essentially stop, and the fracture will preferentially grow into the lower-stress zone.

Therefore, prediction of in-situ stresses, and especially the prediction of stresses relative to the stresses in the surrounding zones, is essential for predicting the growth of fractures in a formation. Ideally, fractures would be contained to areas of a formation with high concentrations of hydrocarbons and would avoid areas with lower concentrations or areas which produce unwanted products. Fractures would be targeted to the zones with higher concentrations of hydrocarbons and ideally not propagate into zones of lower concentrations to maximize the hydrocarbon extraction of the fracture and the well.

This thesis focuses on the determination of in-situ stresses in a shale formation, beginning with laboratory determined and calibrated mechanical characterization, testing of creep properties of samples, and concluding with incorporating these properties into a complete and predictive geomechanical stress model to accurately predict stresses in each layer. While the focus is placed on the specific formation of the Caney, located in Oklahoma, the methodology and overall discussion of behavior could be applied to any formation. Of specific interest is the influence of creep properties on the in-situ stresses, as this is an area which has not been thoroughly examined. This work will show how failure to account for creep can fundamentally change the predictions of which layers will have lower stresses, and hence be targets for fracture growth, and which will have higher stresses and hence be barriers to fracture growth.

In addition to hydraulic fracturing applications, the prediction of in-situ stresses is also vital for any operations which impact the stress field around a wellbore. Injection of fluids such as wastewater or CO₂ can cause induced seismicity due to a change in the stress field for the critically stressed crust (Amemoutou et al., 2021, White and Foxall, 2016). The same concerns are present when examining geothermal or hydrogen storage applications (Zang et al., 2014, Burtonshaw et al., 2022). While this thesis will focus on the hydraulic fracturing aspect of stress prediction, these other scenarios are also applicable for the methods and conclusions discussed in this thesis.

1.1 Fracture Growth and Propagation

While a full discussion on hydraulic fracturing, which includes fracture propagation models is outside the scope of this thesis, a brief review of the basics is useful for context when discussing how in-situ stresses influence fracture growth and propagation.

By definition, a hydraulic fracture is a fracture caused by a high-pressure fluid (Economides and Nolte, 1987). The fluid pressure is sufficient to overcome the strength of the rock, essentially splitting it apart as the fluid moves along the induced fracture. This pressure is achieved by isolating the area to be fractured, typically with an inflatable packer above and below. A packer fills the diameter of the wellbore (the drilled hole with metal pipe called casing) and prevents pressure from escaping into the entire well, instead focusing it into the specific section of casing and formation.

Once the section to be fractured is isolated, a fracturing fluid is pumped into the section. This fluid is typically a higher viscosity than water so it can carry small particles called proppant into the formation. Proppant is a material, typically sand, which is pumped into the formation as suspended particles in the fracturing fluid. As the fluid propagates into the formation, the proppant is transported along with it. The proppant is then left behind as the fracturing fluid is removed from the formation. Ideally, the proppant will keep the fracture propped open, and not become embedded in the formation, as embedment will allow the fracture to close and the overall flow area will be reduced.

The mechanism of importance for this thesis is the growth of the hydraulic fracture. If the fracture is placed in a region with a uniform stress field, the fracture will grow in a relatively uniform pattern out from the initiation point. As a fracture grows in this way, if there is no change in the overall stress field the fracture will continue to grow in a uniform direction. If, however, it

reaches an area with lower stresses, the growth of the fracture in the higher-stress zone will essentially stop, and the fracture will instead propagate faster in the lower-stress zone. Fractures grow preferentially in lower-stress zones, and therefore predicting relative stresses between areas of a formation helps predict the growth of fractures (see for example Economides and Nolte, 1987).

The vertical distance a fracture grows is referred to as “height”, while the horizontal distance is “length” and the amount of opening the fracture as “width”. In this thesis, the fracture height is the parameter of interest. As the fracture grows, the fracture height will be controlled by the stress in the surrounding formations (see for example Economides and Nolte, 1987). A formation with comparatively high stress will prevent the fracture from propagating into the higher-stress zone, while an area with comparatively lower stress will encourage fracture growth into the section. As an example, Figure 1 is an illustration of how fractures will propagate from a medium-stress zone into a zone with low stress but not grow into a zone with high stress.

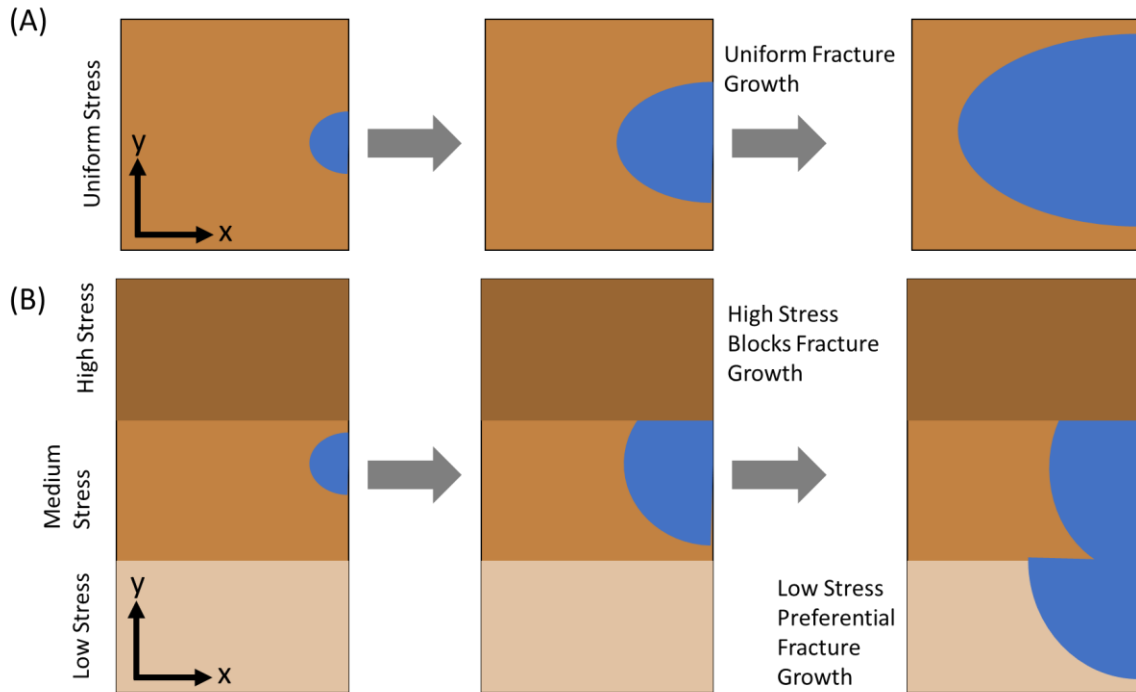


Figure 1 Illustration of fracture growth patterns due to (A) a uniform stress field and (b) a variable stress field (based on Economides and Nolte, 1987)

The main reason for wanting to predict the growth of fractures is to target specific areas for stimulation and production. If the zone which contains the most hydrocarbons is also the zone with the highest stress, it will be difficult to create fractures in this zone, and the fractures will preferentially grow into the surrounding lower-stress zones. However, if the surrounding zones have higher stress, then the fracture will be well contained, and a large fracture can be created in the target zone without propagating into surrounding zones.

Related to fracture growth, the role of long-term deformation of the formation also plays a role in hydrocarbon production. As will be discussed in Chapter 3.0, a formation which is very prone to creep is also prone to proppant embedment. Ideally, the proppant will keep the fracture propped open, and not become embedded in the formation, as embedment will allow the fracture to close and the overall flow area will be reduced. Predicting the embedment of the fracture, and

the deformation of the formation due to creep, is critical for predicting the long-term fracture closure.

1.2 Current Practices

Accurate prediction of how well a formation may be depends on knowledge of brittle/ductile differentiation within the target formations and prediction of relevant stresses. These factors are not mutually exclusive, as ductile zones are thought to be barriers to fracture growth not only because they do not fracture as easily but also because their nominally ductile nature lends them to be areas of higher stress in a formation. However, there are significant issues with defining a formation as “ductile” or “brittle” and assigning fracture properties based on these distinctions.

1.2.1 Brittleness Index

While ideally the in-situ stresses and properties of a formation are known, the determination of these can be cost and time prohibitive. Therefore, several correlations to more easily obtainable data have been made, such as a correlation between compressive strength and acoustic velocity (Bai, 2016). Along these lines, Brittleness Index is a common index used to predict if a formation would be a good target for stimulation or a potential barrier to fracture growth. “Ductile” materials will not fracture well and may act as barriers, while “Brittle” zones should be targeted for fracture growth. However, this method does not take into account the applied stresses,

and as will be demonstrated, can provide conflicting results depending on which definition of Brittleness Index is used.

An additional issue with this method is the inherent definitions of “Ductile” and “Brittle” which are associated with Brittleness Index (Benge et al., 2021a). The proposed meaning hidden in the definition is ductile zones will act as fracture barriers while brittle zones should be targeted for stimulation. This, however, also has the confusion with ductile and brittle behavior and failure, neither of which is the intended comparison when discussing fracture growth.

1.2.2 In-Situ Stress Prediction

Currently, there are methods to measure in-situ stresses in the field. The minimum horizontal pressure can be determined using a mini-frac test, where the formation is hydraulically fractured and the fracture is propagated while monitoring pressure equipment on the surface. Obviously, this has the disadvantage of requiring specific equipment at the rig and requires the time and operational expertise needed to run and analyze the data.

One of the oldest methods is to estimate the stresses based on factors such as the overburden pressure (Bourgoyne et al., 1986). Eaton (1969) proposed a calculation of horizontal stress based on the vertical stress and Poisson’s ratio. The Poisson’s ratio of a formation could be estimated based on the acoustic velocities obtained using a sonic log, and vertical stress could be estimated either using a general gradient for a region or by accounting for the density and thickness of the overlying formations called the overburden. However, this method does not take into account factors such as tectonic strains or any properties of the formation other than Poisson’s ratio which may impact the in-situ stresses.

A method presented by Sone and Zoback (2014a and 2014b) attempts to account for both tectonic strain and creep behavior of the formation. By accounting for tectonic strains, the model acknowledges the forces in the earth acting on the formation which would change the stress state away from being simply the overlying rock pressing down vertically. Creep behavior, or more specifically stress relaxation, accounts for long-term deformation in the system, leading to changes in stress as the formation deforms and relieves those stresses.

This thesis proposes another method to calculate the in-situ stresses, a finite element model which includes both tectonic stresses and creep properties. Unlike the method proposed by Sone and Zoback (2014a and 2014b), this method does not rely on preexisting knowledge of the stress state of the formation. Instead, an estimate of potential tectonic strain rates can be examined to determine an upper and lower limit to the stresses. Another advantage of this method is the parameters of the model can easily be verified with a mini-frac test, and depending on the propagation of the fracture the relative stresses in different areas of the formation can be verified. The magnitude of the stresses is also verified during the mini-frac test, as the traditional analysis of this test calculates the minimum principal stress acting on the formation.

1.3 Problem Statement and Structure

Current practices do not clearly identify formations which will act as barriers to fracture growth and which should be targeted for stimulation due to lower stresses. To address this issue, this thesis takes the Caney shale as a case study, performing laboratory testing and finite element analysis to answer the questions “Is the identification of a material as ‘Ductile’ or ‘Brittle’

applicable to hydrocarbon-bearing formations?” and “Based on the data obtained from laboratory testing, can zones be identified as targets for stimulation or barriers to fracture growth?”

Prior to examining these questions, samples needed to be tested to determine their mechanical properties. A ductile material is typically described as a material which will yield before failure, while a brittle material fails quickly. Chapter 2.0 details the experimental procedures used not only to determine the failure behavior of the samples, but also the strength of the samples at different conditions. Of particular importance to answering the questions posed in this thesis is the testing of long-term creep deformation.

The first question, if a formation can be identified as “Ductile” or “Brittle” and the applicability of this label to a formation, is addressed in Chapter 3.0. This chapter focuses on the definitions of ductile and brittle formations as defined by the Brittleness Index. The main focus is on defining the obtained Caney shale samples based on these definitions, and to highlight any clear differences in behavior which correspond to these definitions.

In terms of the applicability of defining a formation as nominally ductile or nominally brittle, Chapter 4.0 presents long-term creep tests performed on the Caney shale samples. The properties obtained from creep testing provide additional insight into the initial definition of zones identified as “Ductile” or “Brittle”. As a demonstration of the importance of including creep properties when examining the long-term behavior of formations, a model is presented to predict proppant embedment and fracture closure which includes the creep properties predicted using laboratory data.

Finally, Chapter 5.0 presents a finite element model to predict the in-situ stresses in the formation. This chapter compares both the current practices such as Eaton (1969) and Sone and Zoback (2014a and 2014b) with a finite element model which includes both elastic properties and

creep deformation. As discussed, the in-situ stresses have a significant influence on the growth of fractures in a formation, and this chapter asks the question of which zones are identified as barriers to fracture growth or targets for stimulation based on the in-situ stresses.

Chapter 6.0 concludes this thesis, providing a summary of results and recommendations for additional research to improve the understanding of how formation properties contribute to the in-situ stresses and fracture growth.

2.0 Experimental Procedures

This chapter is a presentation of laboratory procedures used to determine the mechanical properties of the Caney shale samples. Testing procedures are detailed to provide a guideline for similar laboratory testing and for result reproduction if necessary. While other chapters review the test procedures as needed for discussion, this section provides the most in-depth description of all practices used in the determination of mechanical properties.

2.1 Sample Description

Approximately 152 m (500 feet) of core was obtained from a pilot well drilled through the Caney formation. After analysis of the well log identified five zones of interest, these zones were marked for plugging to obtain cylindrical samples which could be used for laboratory testing.

Based on the identified zones from the well log, 30 mm (1.18 inches) diameter by 60 mm (2.36 inches) long cylindrical samples were obtained from each of the five zones. Samples were obtained in multiple orientations, vertical (drilled perpendicular to bedding planes), horizontal (drilled parallel to bedding planes) and 45° relative to bedding planes. An intact 45° sample for the second ductile zone could not be obtained. All samples were drilled and surfaced at the coring facility prior to being sealed in plastic bags for storage. Samples were stored in air-tight conditions to prevent additional surface drying and tested in an “as received” state assuming no significant surface drying.

While samples used for unconfined, triaxial, and creep testing did not need additional preparation work, samples used for tensile and fracture toughness testing needed to be cut from the 30 mm by 60 mm (1.81 by 2.36 inches) cylinders. A tile saw was used to cut the sample into approximately four equal samples, leaving smaller discs 30 mm in diameter by approximately 15 mm length (0.59 inches). No fluid was used with the tile saw to prevent any swelling of clay components due to water or intrusion of oil. Fracture toughness discs were obtained from a separate 30 mm by 60 mm cylinder than the tensile samples. These samples were first cut into the same dimensions as the tensile samples before they were cut in half along their diameter and a coping saw was used to cut a 6 mm (0.24 inch) notch in the center of the sample to create the semi-circular notched bending samples as recommended in the procedure provided by Lim et al. (1994).

Sample preparation for triaxial and creep testing was essentially the same. First, four strain sensors would be attached to the sample using an adhesive specifically made for attaching strain sensors. Small wires would then be soldered to the strain sensors and these would be attached to larger wires to connect to the strain recorder. The smaller wires were needed to prevent the wires from interfering with or being damaged by the loading platens used in the Hoek-type triaxial cell. Each pair of sensors was placed on opposite sides of the sample to provide an accurate depiction of strain on the sample. For triaxial testing, each pair of sensors consisted of a vertical sensor to measure axial strain and a horizontal sensor to measure radial strain. During creep testing it was found there was negligible creep in the radial direction so all sensors were oriented to capture axial strain. With the sample prepared, it was placed in a polymer sleeve which would prevent contact with the confining oil when the sleeve and sample were installed in the Hoek cell.

2.2 Test Procedures

2.2.1 Unconfined Compressive Strength

Unconfined compressive testing was completed at an external laboratory. Results from unconfined testing consisted only of the ultimate compressive strength.

2.2.2 Indirect Tensile Strength

Tensile samples were supplied initially as 30 mm by 60 mm (1.18 by 2.36 inches) cylinders. To prepare the samples for testing, a tile saw was used to slice the samples into four discs of approximately equal length, resulting in samples 30 mm in diameter by 15 mm (0.59 inches) in length. The length, diameter, and mass of each sample were recorded and samples were photographed prior to testing. A center line was marked on the sample to compare the tensile fracture pattern to the ideal center fracture.

The tensile test procedure was based on ASTM D3967-08. The load frame used for testing the tensile samples was a small pump-driven piston with a force sensor attached to the top platen of the frame. As the pump pressure increased, this would displace the piston and apply a load to the sample which was recorded by the force sensor. Samples were placed in the frame with the centerline vertically aligned to the loading platen. A preload of up to 44 N (10 lbf) was allowed to keep the sample in position while setting up for the test. Small pieces of cardboard were placed between the tensile sample and the loading platens to minimize edge effects. A photograph of the sample in the frame is provided in Figure 2.



Figure 2 Tensile sample loaded in frame

The sample was loaded at a constant pump flow rate of 0.70 mL/min (0.023 oz/min), which produced a load rate between 16.9 and 19.1 N/s (3.8 and 4.3 lb_f/s), until failure was detected. This rate was chosen based on the ASTM standard to reach failure within approximately five minutes of starting the test. The maximum force applied to the sample was recorded from the force transducer in the frame. After testing was complete, the sample was removed from the machine and photographed. The tensile strength of the sample was calculated using Equation (2.1).

$$TS = \frac{2 * F}{\pi * D * L} \quad (2.1)$$

where TS is the calculated tensile strength (in MPa or psi), F is the maximum applied force (in N or lb_f), D is the diameter of the sample (in mm or in), and L is the length of the sample (in mm or in).

2.2.3 Fracture Toughness

A semi-circular notched bending test was selected as the method to determine fracture toughness (see Lim et al., 1994). As multiple cylinders were marked for tensile testing one was selected to be used for fracture toughness testing. The cylinders were cut first into 30 mm (1.18 inches) diameter by 15 mm (0.59 inches) width discs, and these were cut in half along their diameter to produce half-circle discs. The same cutting procedure was used as for the tensile samples, a tile saw with no fluid to avoid introducing fluid into the samples. Dimensions of the cut sample are shown in Figure 3. The small notch was cut by hand into each using a coping saw with a diamond cutting wire. The notch was created perpendicular to the cut flat surface of the sample and made to a depth of 6 mm (0.24 inches). The width of the notch was the same as the bade of the coping saw.

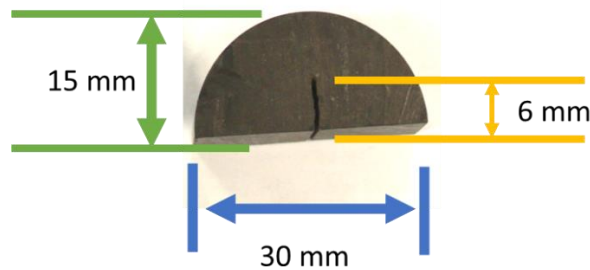


Figure 3 Fracture toughness sample with dimensions marked

The dimensions of each sample were noted and the mass of each sample recorded prior to testing. Samples were loaded into a Test Resources load frame as shown in Figure 4, with a small preload up to 44 N (10 lbf) applied to the sample to keep it in place as the test was started.

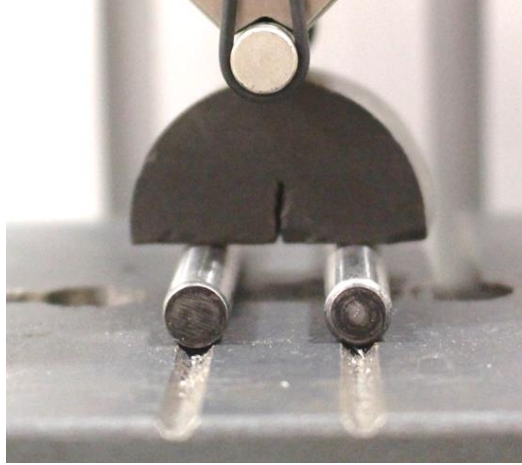


Figure 4 Fracture testing sample placed in load frame

Fracture samples were loaded at a constant displacement rate of 0.02 mm/min (0.008 inches/minute) until failure was detected. This rate was selected to match the axial load rate of the triaxial test procedure. The maximum force was recorded and the value of K_{IC} was calculated using Equations (2.2) and (2.3) (Lim et al., 1994).

$$K_{IC} = Y' * F_{max} * \frac{\sqrt{\pi * a}}{2 * r * W} \quad (2.2)$$

$$Y' = -1.297 + 9.516 * \left(\frac{S}{L}\right) - \left(0.47 + 16.457 * \left(\frac{S}{L}\right)\right) * M + \left(1.071 + 34.401 * \left(\frac{S}{L}\right)\right) * (M)^2 \quad (2.3)$$

where L is the length of the sample along the flat edge, r is the radius of the sample, W is the width of the sample, a is the length of the notch in the sample, s is the distance between the two bottom supports of the loading platen, and M is the length of the notch divided by the radius of the sample ($M = \frac{a}{r}$).

2.2.4 Creep and Triaxial Testing Sample Preparation

Additional sample preparation was required for triaxial and creep testing. First, the 30 mm by 60 mm (1.18 by 2.36 inches) cylinders were removed from their storage bags and examined for any apparent issues such as cracks, dents, or parting. Any imperfections were noted. To measure the axial and radial strains during testing, strain gauges were attached to the outer surface of the sample. For triaxial testing, each pair of axial and radial sensors were placed opposite each other. An initial test determined the amount of radial deformation during creep testing was negligible, and therefore all strain gauges were oriented axially for creep testing.

In addition to attaching strain sensors, filter paper was wrapped around the top and bottom edges of the sample and two strips were placed axially between the two sets of strain sensors. The test equipment did not include pore pressure control, and therefore the filter paper would allow pore fluid to move away from the sample during testing, maintaining the system as a drained pore condition test. The paper was carefully placed to avoid edge effects and to not interfere with any measurements. The sample was also wrapped in clear sellotape to keep the filter paper in place, help keep the wires from becoming wedged between the sample and the confining sleeve, and to hold any samples which had parted at bedding planes in place. An example of a sample with strain gauges and filter paper is provided in Figure 5. Note this photograph is post-test, and the wires connecting the strain gauges to the data acquisition system have been cut.

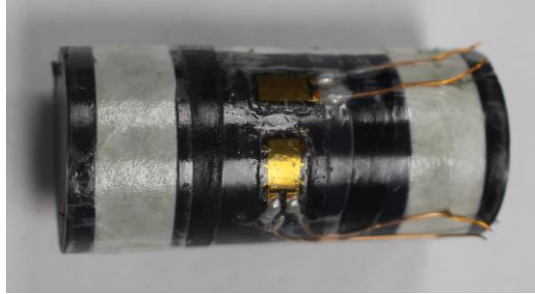


Figure 5 Post-Test photograph demonstrating placement of sensors and filter paper

Both triaxial and creep procedures employed a Hoek triaxial cell, where the sample is loaded into a polymer sleeve prior to the sleeve being placed in a cell. The external surface of the sleeve can then be pressurized using an external pump, in this case an ISCO syringe pump, which provides confining pressure for the samples. A diagram of the Hoek cell setup is provided in Figure 6.

Small spacer platens were inserted into the polymer sleeve above and below the sample to ensure the sample would remain centered in the sleeve during testing. This avoided any issues with the edge of the cell which might interfere with the application of the confining pressure. The topmost platens of the Hoek cell were a pair of semi-hemispherical seated cylinders. These would automatically adjust and account for the small amount of tolerance allowed in the sample dimensions, adjusting to samples whose ends were not perfectly flat and parallel.

Since temperature and confining pressure can influence the properties of a core sample (Roberts et al., 2023), it was decided to test the samples at 90°C (194°F), a temperature as close to the in-situ temperature as was possible in the laboratory. This temperature was chosen because there was no method to provide additional pore pressure to the sample. Without a way to control the pore pressure, higher temperatures would mean any water in the pores of the sample could boil, and therefore the temperature was limited to 90°C. To achieve the desired test temperature, heating

tape was wrapped around the cell and controlled using a BriskHeat temperature controller and a thermocouple located near the top of the sample.

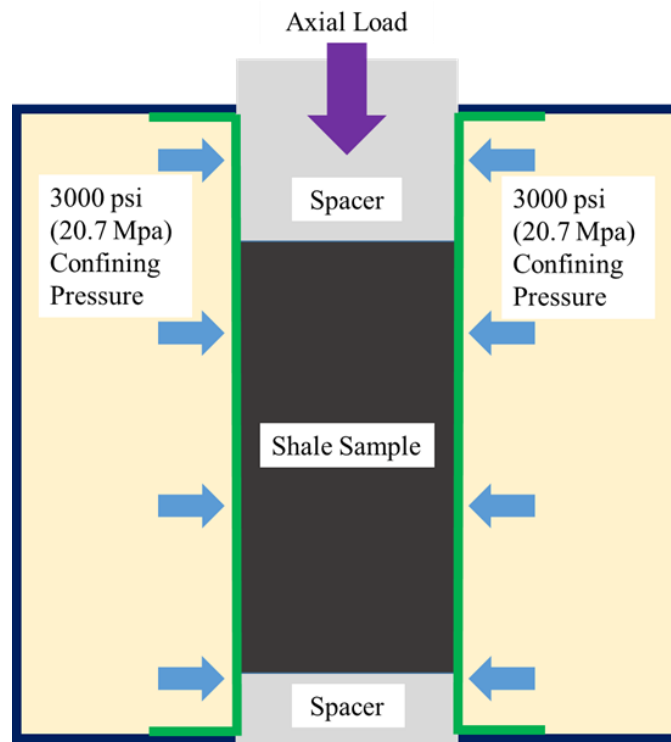


Figure 6 Schematic of triaxial test cell (heated externally) (from Benge et al., 2023)

2.2.5 Single-Stage Triaxial Testing

Triaxial testing was conducted in a single stage using an Instron load frame controlled using Partner software, with the procedure based on ASTM D7012 (2014). Before starting the test, the Hoek cell and sample were placed in the load frame and a small preload was applied, approximately 444 N (100lbf). This preload kept the test setup in place while the monitoring equipment was set up and the heating tape was wrapped around the cell. A small confining

pressure of 0.68 MPa (100 psi) was applied to check the cell for any leaks prior to starting the test. Figure 7 is a photograph of the test setup with the heating tape applied.

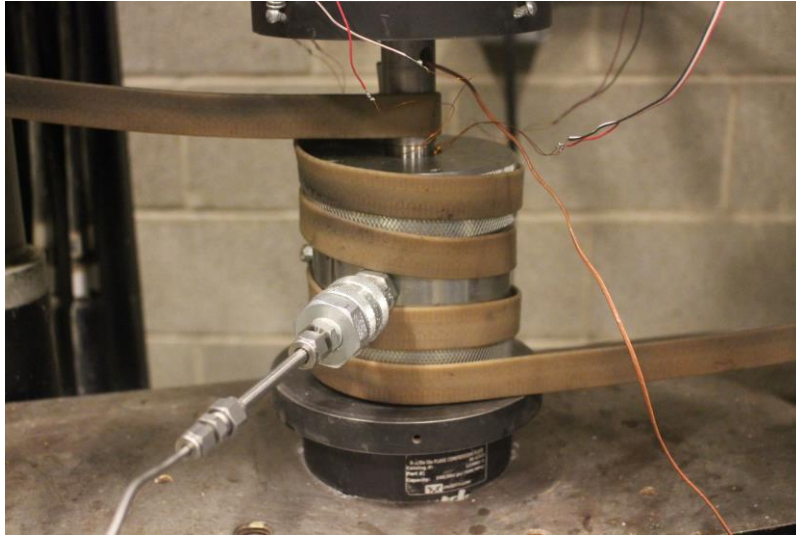


Figure 7 Hoek cell placed in instron load frame with heating tape, data acquisition wires, and connection to ISCO pump (modified from Bengtson et al., 2023)

While the sample was heating to the desired temperature of 90°C, an initial axial load and confining pressure was applied to the sample to ensure no air would enter the system and to provide a hydrostatic stress state during the temperature ramp. For tests conducted above 3.4 MPa (500 psi) confining pressure, this initial stress was 3.4 MPa. For the 3.4 MPa test, 1.7 MPa (250 psi) of hydrostatic pressure was applied to maintain uniform conditions to the other samples. For the 0.34 MPa (50 psi) tests performed to simulate unconfined testing, the pressure was set to 0.34 MPa and remained constant throughout the test.

During the temperature ramp, the axial load, confining pressure, and pump reservoir volume were noted. This was to ensure there were no slow leaks in the system which would

compromise the application of the confining pressure and to keep the applied axial load constant to avoid removing the applied hydrostatic pressure.

Once the sample reached the test temperature, the hydrostatic pressure was increased to the test pressure. Depending on the test, this would be 3.4, 10.34, or 20.68 MPa (500, 1500 or 3000 psi). No increase was needed for the 0.34 MPa test. The sample was then allowed to equalize for one hour before starting the test to ensure the sample was at a constant temperature and load.

Compressive testing was conducted using a constant axial displacement rate of 0.2 mm/min (0.008 inches/minute) until the sample failed. This rate was chosen to ensure the sample would fail within the time requirements of ASTM D7012 (2014). During the loading, the strains, load, and axial displacement of the load frame were measured at a rate of one sample every second until the sample failed. After failure, additional loading would cause the confining membrane to fail and result in a loss of confining pressure, so post-test failure analysis was not possible with the test equipment. The sample was slowly brought back to ambient conditions after the completion of the test. Samples were photographed and stored in mineral oil in case additional analysis was requested.

The dynamic and static determinations of Young's modulus and Poisson's ratio differ significantly. As will be discussed in Chapter 3.0, there is not as clear of a differentiation between the static values of Poisson's ratio as was identified using the dynamic properties from the well log. Figure 8 provides a reference graph to compare the dynamic and static Young's modulus and Poisson's ratio. The average value from the well log is presented alongside the results from the 20.7 MPa (3000 psi) triaxial results.

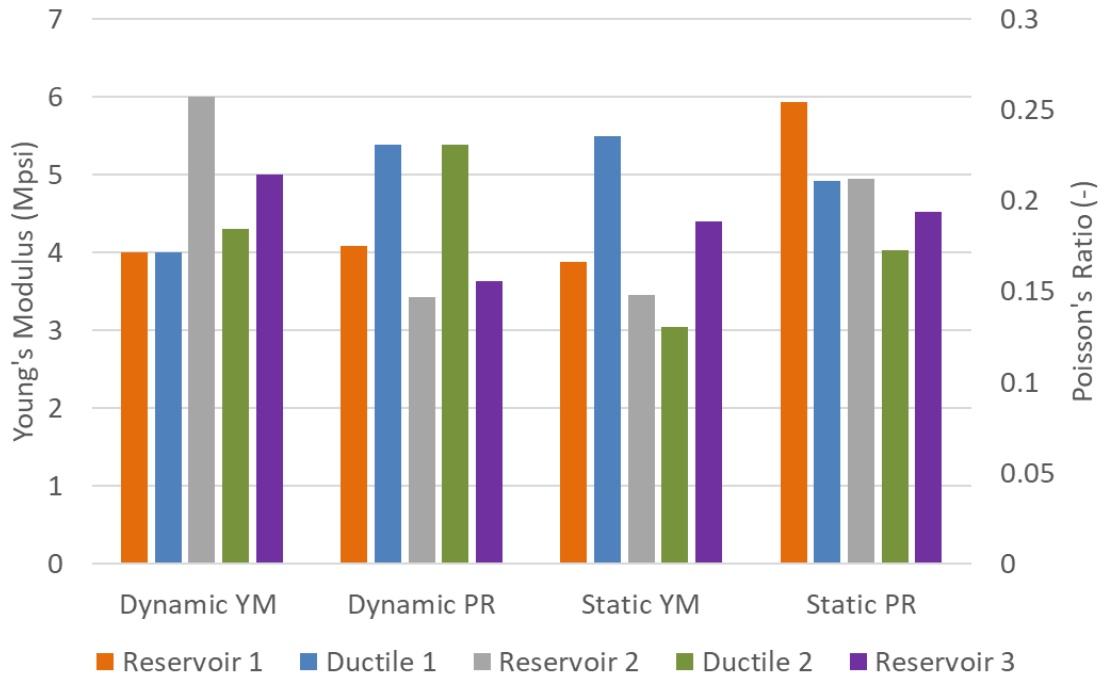


Figure 8 Dynamic and static Young's modulus and Poisson's ratio from average of well log and 20.7 MPa (3000 psi) triaxial testing

Overall, there is not a clear correlation between the static and dynamic Young's modulus and Poisson's ratio values for these samples. Only Reservoir 1 appears to have similar dynamic and static Young's modulus values. The static Young's modulus of Ductile 1 is higher than predicted using the dynamic properties, while the static moduli for Reservoir 2, Ductile 2, and Reservoir 3 are all lower than their dynamic counterparts. There is also a clear difference between the static and dynamic Poisson's ratios, with the reservoir zones providing higher static ratios and the ductile zones providing lower ratios than would be predicted using the dynamic Poisson's ratio values.

There are several adjustment parameters which can be used to calculate the correlation between the static and dynamic Young's modulus values as the correlation is not typically one-to-one (Brotons et al., 2016, Martínez-Martínez et al., 2012). However, as demonstrated by

comparing the static and dynamic Young's modulus values for the ductile and reservoir zones, a numerical adjustment based on the dynamic modulus or acoustic velocity would not correctly predict the static modulus values. The first Ductile zone would need to have a correlation with a higher static Young's modulus compared to the dynamic modulus while Reservoir 1 would have very little adjustment and all other zones would require a correlation which provides a lower static Young's modulus than the dynamic modulus.

2.2.6 Creep Testing

Creep testing used the same equipment as described for the triaxial testing with the addition of three external LVDTs to measure axial displacement and the transition to an MTS 810 load frame to provide better load control during the long-term test. It was found the LVDTs were necessary because the adhesive used to attach the strain sensors to the sample would fail after prolonged exposure to the test temperature. While the time frame of the adhesive deformation was long enough not to interfere with the triaxial testing, the nearly week-long creep test provided enough time for the decrease in measured axial strain to significantly impact the results. Therefore, to provide accurate measurements of the displacement of the sample, three LVDTs were placed 130° apart and measured the displacement of the top piston of the load frame relative to the plate the sample was sitting on. It was assumed the deformation of the sample would be significantly higher than the deformation of the steel platens, and therefore the LVDTs would measure the displacement of the shale sample during creep testing.

The MTS 810 load frame was chosen as the load frame used during creep testing because the FlexTest SE controller provided more precise load control. Load control is critical to maintain

the desired applied axial stress when measuring the creep deformation over time. Controlling using the load instead of the displacement ensured the sample would maintain the specified 30% stress level, as a changing load would add additional complication to the later calculation of creep parameters.

While triaxial testing used a constant displacement rate to apply increasing stress until failure, creep testing would use 5-minute stress ramps to reach predefined stress conditions. As the exact axial strain needed to apply the necessary axial stress could not be exactly calculated due to factors such as small gaps between the platens and the sample or the slow deformation of the sample resulting in a slight decrease in sample length, this method allowed an exact load to be applied. Controlling the axial force instead of the displacement of the piston resulted in a different axial strain rate applied to the creep samples, which will be factored in when examining results obtained during times when the applied stress was increasing or decreasing.

As with the triaxial testing, the sample was placed at a lower confining pressure of 3.4 MPa (500 psi) while the sample reached temperature. The confining and axial stress were then increased hydrostatically to 20.68 MPa (3000 psi) after the approximately two hours it would take for the sample to reach 90 °C. After reaching temperature, the sample was allowed to equalize for 24 hours, a step found to be necessary to remove any additional drift in the strain values due to the temperature or sample settling.

Due to the aforementioned slow deformation of the adhesive used to attach the strain sensors to the sample, the strain sensors were not intended to be used for the long-term creep. Instead, they were only used to measure the change in axial strain during the load/unload cycles of the procedure. While data was continually recorded during testing, the strain sensor data was collected once every three seconds. Meanwhile, the load, LVDT displacements, and crosshead

displacement were measured twice every second. Temperature was also monitored during this long-term test, with data recorded once every second.

During creep testing, the load was increased or decreased using a 5-minute ramp based on the applied axial stress. This time frame was chosen to provide a consistent load/unload regime for all samples which matched the 5-minute ramp used to apply the increased hydrostatic stress after reaching temperate. The minimum stress applied was equal to the 20.68 MPa confining pressure, and the maximum stress applied to the sample was 30% of the expected maximum stress based on the triaxial testing results at 20.68 MPa confining pressure. This 30% was chosen to load the sample with enough force to allow creep deformation in a measurable amount of time while not loading the sample to yielding or failure. The loading regime was modified from the procedures described by Sone and Zoback (2014a and 2014b). Due to time restrictions, the interval of loading cycles was shortened and the test was stopped after 72 hours of loading as the LVDT sensors did not register any significant deformation after this point in time.

Creep testing began with a 20-minute load/unload cycle. This provided an estimation of the elastic strain in the sample which could later be subtracted from the total strain to determine the plastic portion of the strain, providing an estimate of the recoverable and non-recoverable components of the strain. Longer-term elastic and plastic creep components were determined using a 12-hour load, 12-hour relaxation, second 12-hour load, and a 2-hour unload creep test cycle. Examining the difference between the initial strain and final strain for each loading cycle and the difference between the initial strain of a relaxation cycle and the final strain of the previous loading cycle were used to calculate the recoverable and non-recoverable strain components. These multiple load/unload cycles therefore provided the necessary data to determine the elastic and plastic portions of strain. Finally, the sample was loaded to the 30% of the expected confined

compressive strength at 20.68 MPa confinement based on single stage triaxial test and remained loaded for 72 hours to provide data to calculate the long-term creep deformation of the sample. After this final loading stage, the sample was slowly brought back to ambient conditions and the test was complete. This procedure is demonstrated in Figure 9, where the applied axial stress is shown over time.

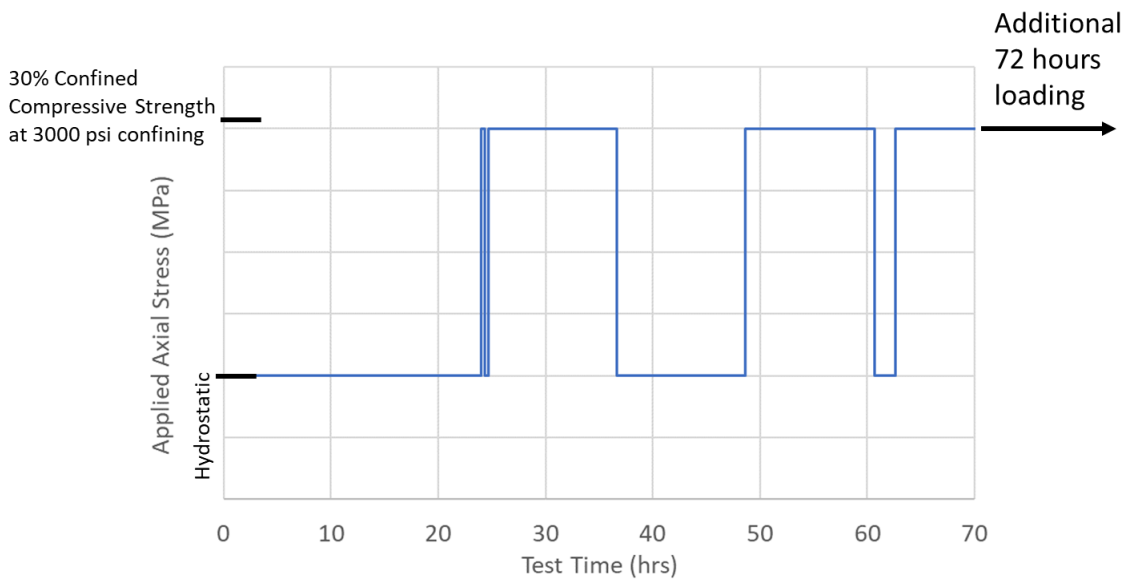


Figure 9 Diagram of applied axial stress during creep testing

2.2.7 Young’s Modulus Determination from Creep Testing

Due to the limited number of available samples, triaxial tests could not be completed using the samples drilled parallel to bedding and at 45° relative to bedding. However, the five-minute load/unload cycles provide the opportunity to calculate Young’s modulus from the creep tests.

The calculation of Young’s modulus from the five-minute loading cycles in the creep procedure is straightforward and used the same method as for the triaxial testing. However, creep

testing used a force-controlled load while the triaxial test used a constant displacement rate. As previously mentioned, the force-controlled ramp resulted in a different displacement rate than triaxial test. Because Young's modulus can be impacted by the rate of loading, this was accounted for by comparing the Young's modulus values of the vertical samples.

Taking the Reservoir 1 as an example, the first 12-hour load cycle provided a vertical Young's modulus of 33.4 GPa (4.84 Mpsi) and a horizontal Young's modulus of 37.7 GPa (5.47 Mpsi). The ratio of the vertical and horizontal Young's modulus values from the creep tests is 1.13. So the vertical sample had a Young's modulus 1.13 times lower than the horizontal sample. The triaxial test on the vertical sample provided a Young's modulus value of 26.8 GPa (3.89 Mpsi). Multiplying this by the ratio determined using the creep testing, 1.13, gives a predicted horizontal Young's modulus of 30.2 MPa (4.38 Mpsi).

This method was used to calculate the Young's modulus values of the horizontal and 45° samples as if they had been tested using the triaxial test setup. For reference, Figure 10 provides a comparison of Young's modulus values calculated from the first 12-hour load cycle for each orientation.

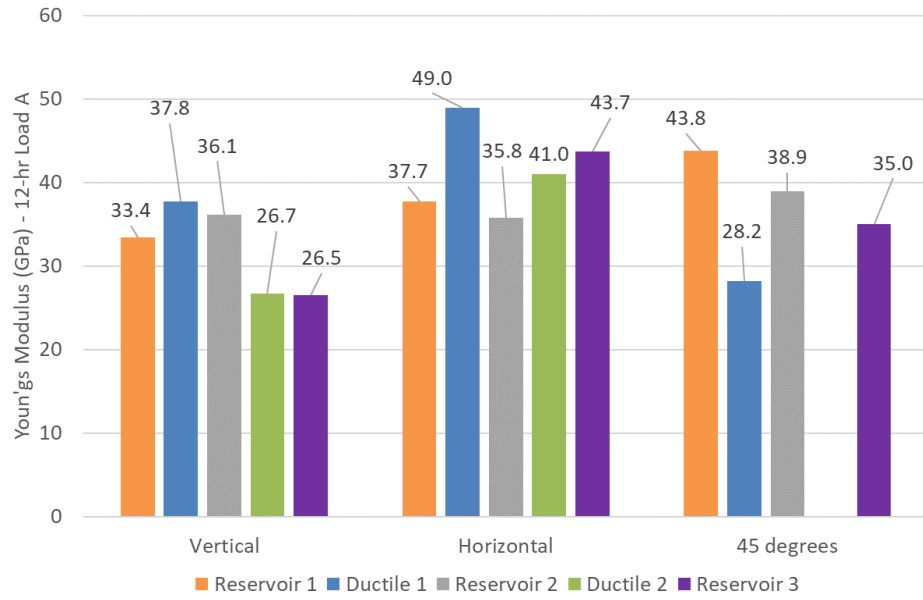


Figure 10 Young's modulus values for different sample orientations, from first 12-hour load stage of creep testing

3.0 Brittleness Index and Mechanical Behavior

This chapter contains an analysis of the mechanical properties of the Caney shale samples. As this work was completed prior to the completion of the creep testing, the main focus is on determining if the initial analysis of “ductile” and “brittle” based on the acoustic well log is applicable to the Caney shale, using Brittleness Index calculations as an indication of the nominally more brittle or ductile behavior of each identified zone in the formation. Brittleness Index is chosen as the metric to predict the behavior of the formation. This is a common metric used in industry to identify areas of a formation which should be targeted for stimulation and which areas may act as barriers to fracture growth. While the previous chapter provided an overview of all laboratory testing, this chapter is a reproduction of a previously published work and therefore includes a recurrence of any testing relevant to the calculation of Brittleness Index.

The relative ductile or brittle behavior of a formation is important for stimulation, as brittle materials will fracture easily and have more complex fracture growth compared to relatively ductile materials. With respect to the oil and gas industry, brittle zones are seen as ideal targets for stimulation, and an ideal brittle formation will fracture easily with highly complex fractures to maximize the area stimulated and therefore maximize hydrocarbon extraction. In addition to fracturing in less ideal ways, ductile formations are also seen as potential barriers to fracture growth. It is assumed for a given horizontal stress a fracture initiated in a brittle zone will not typically propagate into a ductile zone. For this reason, the prediction of a formation as “ductile” or “brittle” is very important for planning not only the location and trajectory of wells but also the stimulation of those wells.

While ideally the ductile or brittle nature of a material would be determined using laboratory tests specifically tailored to the application of the material, it is not always possible to test samples from formations, either due to testing resources or a lack of samples to test in the laboratory. For example, formations under high in-situ stresses experience significant changes in stress after they are brought to the surface, and while an intact core may be obtained in the well it may fracture due to the relative increase in pore pressure when the core is brought to the surface. Obtaining core is also very expensive, both in terms of equipment and time, and there may not be sufficient budget to obtain in-situ core samples. Factors such as these mean there is a significant advantage to obtain a correlation between the behavior of the formation and parameters which can be much more easily measured. For example, mineralogy can be obtained from the formation cuttings naturally produced during drilling, or acoustic properties can be obtained from a logging tool run into the well. This is the motivation behind the brittleness index, and why determination of the brittleness index and its relationship to the true behavior of the formation is a critical aspect of characterizing and understanding the Caney formation.

This chapter presents work previously published in a paper titled “Mechanical Properties of Nominally Ductile and Brittle Zones Within the Caney Shale Formation”, presented at the 55th US Rock Mechanics/Geomechanics Symposium held in Houston, Texas, USA, 20-23 June, 2021. While minor modifications have been made, the copyright remains with the American Rock Mechanics Association, and all material has been reprinted with permission.

3.1 Chapter Summary

This chapter presents a case study from the Caney Shale, which is an emerging hydrocarbon-bearing formation in Oklahoma. Open hole logs lead to a nominal distinction of five zones in an exploration well, two of which are designated “ductile” and three of which are designated as less ductile “reservoir” zones. Subsequently, a detailed mechanical characterization was carried out on core plugs taken from each of these zones. Results show nominally “ductile” zones are weaker in terms of unconfined compressive strength, tensile strength, fracture toughness, and confined compressive strength. However, by a variety of brittleness indices, it is found the nominally “ductile” regions do not behave as expected. They are weaker, but not consistently more ductile. Furthermore, some brittleness indices lead to contradictory conclusions. For example, zones which would be considered the most brittle according to the proportion of nonlinear stress-strain behavior prior to failure and/or by indices based on elastic properties would be considered the least brittle according to their internal friction angle.

3.2 Introduction

Ductility is the ability of a material to sustain large inelastic deformation without loss of bearing capacity (e.g. Hajiabdolmajid and Kaiser 2003). Brittleness is most commonly defined as a lack of ductility (e.g. Hetenyi, 1950 as cited by Hucka and Das, 1974). Rock engineering inevitably deals with the behavior of rock beyond its elastic limit, thereby invoking a widespread desire to characterize whether such behavior is “brittle” or “ductile”. The proper answer is rock should be considered a quasi-brittle material because, like concrete (Bazant, 1999), it exhibits

some brittle-like qualities and some ductile-like qualities. The purpose of this chapter is not to delve into this issue, but rather to adopt a starting point wherein it is recognized the petroleum industry has, over the years, adopted a variety of metrics ascribed to characterize brittleness of rock (Bai, 2016).

Therefore this chapter presents a case study from the Caney Shale, which is an emerging hydrocarbon-bearing formation in Oklahoma. The opportunity arises because five subunits of the Caney were originally identified as nominally “ductile” and “reservoir” (i.e. less ductile) layers based on interpretation of open-hole well logs. This was a “blind” identification, documented prior to testing of rock mechanical properties using core from the same borehole. Subsequently, a detailed mechanical characterization was carried out on core plugs taken from each of these five zones. The basic question is whether the log-based demarcation of nominally ductile zones corresponds in a predictive and useful way to mechanical properties and behavior of the rock.

The chapter is therefore comprised firstly of a brief description of the log-based method for identifying nominally “ductile” and “reservoir” zones. The second component of this chapter details experiments consisting firstly of classical mechanical tests at ambient conditions (unconfined compressive strength, Brazilian indirect tensile strength, and fracture toughness from notched semi-circular beam tests). Then triaxial tests carried out at 90 °C are presented. From these experiments, rock mechanical properties are compared among the various zones. Finally there is a discussion of relationships among several indices proposed to embody brittleness.

3.3 Log Analysis and Sample Quality Control

A suite of open-hole petrophysical logs were carried out in an exploration borehole penetrating the Caney shale and from which core was extracted for characterization and testing. Based on a sonic log, the Poisson's ratio was estimated throughout the formation. Additionally, the logging included resistivity and gamma tracks. Analysis of the petrophysical logs led to identification of five zones. Three of these have Poisson's ratio ν in the range $0.15 < \nu < 0.25$. These zones also have the highest values of resistivity and lowest values of gamma. Based on this evidence, these sections are identified as "reservoir" sections and are predicted to be less ductile when compared with other subunits of the Caney formation.

In contrast, two zones have Poisson's ratio in the range $0.25 < \nu < 0.3$ with high gamma and low resistivity. These zones are identified as "ductile", predicted to have higher clay content and behave in a manner less brittle compared to other subunits of the Caney formation.

These five zones are, in order of shallowest to deepest interval, named Reservoir 1 (R1), Ductile 1 (D1), Reservoir 2 (R2), Ductile 2 (D2), and Reservoir 3 (R3).

Samples selected for testing were collected from areas of the identified zones with the most uniform bedding and which would have the highest likelihood of surviving sampling and shipment. An example is shown in Figure 11, where the 1/3 core from Reservoir 1 is photographed.

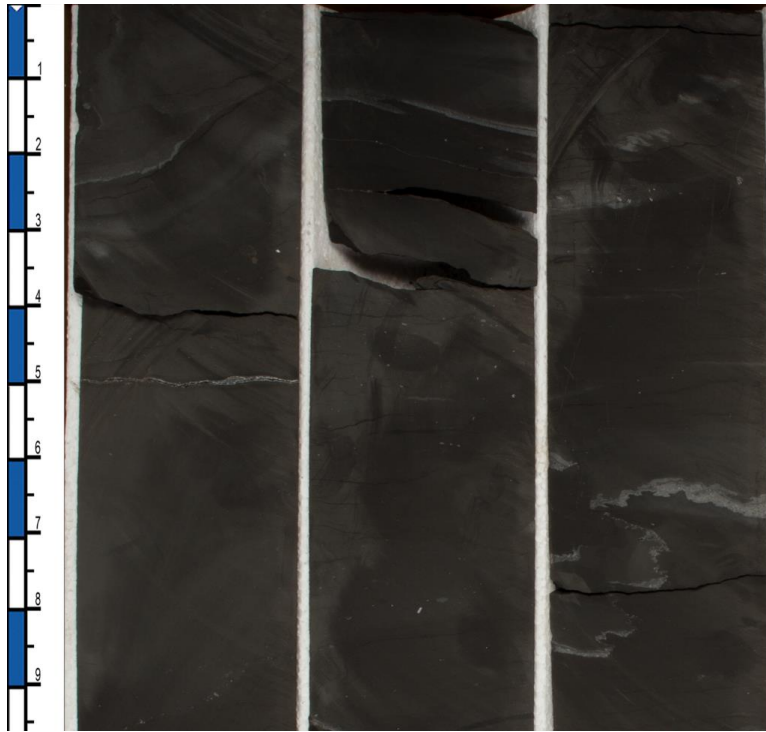


Figure 11 Example photograph of 1/3 core from Reservoir 1

Prior to testing samples were examined using a CT scanner. Any significant separation or internal inclusions were noted prior to testing. An example CT image is provided in Figure 12.

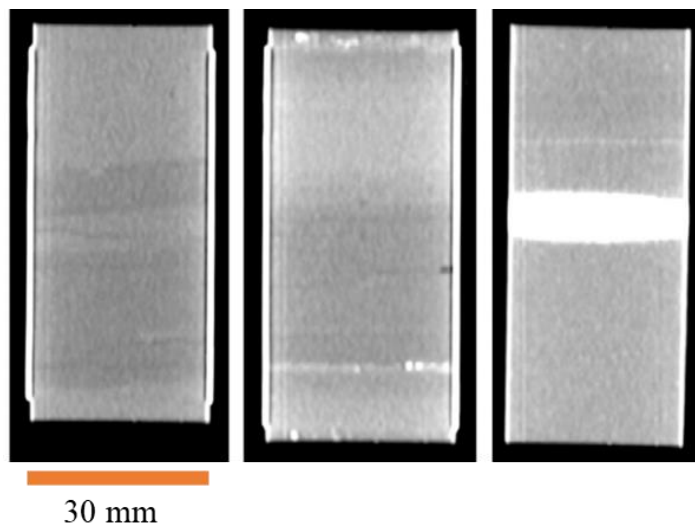


Figure 12 Example CT images from Reservoir 1 (left), Ductile 1 (center), and Reservoir 3 (right)

3.4 Characterization Methods

3.4.1 Mineralogy

Quantitative x-ray diffraction (XRD) was used to analyze powdered samples and determine the mineralogy of the Caney shale. Five grams of samples from selected depths were ground and analyzed using a Bruker D8 Advance XRD with Lynxeye detector. The scanning 2-theta angle was from 5 to 80 degrees with a 0.01 degree steps and a dwell time of 0.5 seconds. Semi-quantitative XRD analyses used BRUKER's Diffrac.suite software.

3.4.2 Strength Tests at Ambient Conditions

Unconfined compressive strength (UCS) tests were carried out on 30 x 60 mm (1.18 x 2.36 in) cylindrical core plugs taken in the vertical direction, perpendicular to bedding (Figure 13(A)). Specimens were cored using mineral oil and preserved in airtight copper jackets and sealed bags until the time of testing. Tests were performed at room temperature. Specimens were loaded at a constant rate to failure, with UCS taken as the ratio of the force inducing failure to the cross-sectional area of the specimen. Between two and four samples were tested for each formation, depending on availability of intact samples, with the average value reported in the Results.

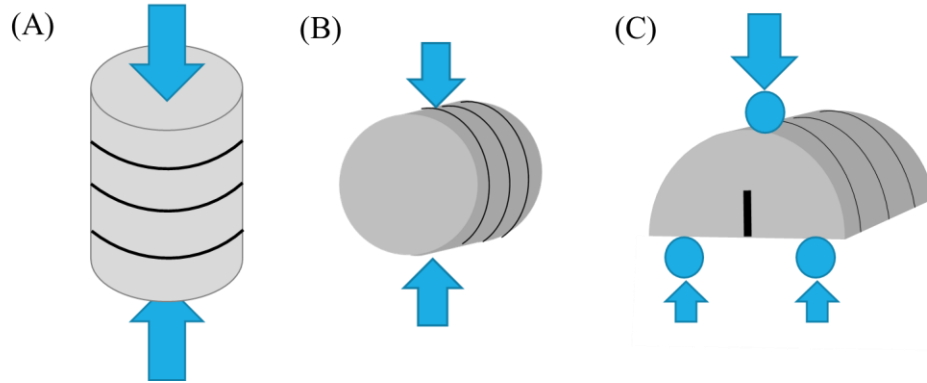


Figure 13 Orientation of bedding planes and indication of loading directions for (A) compressive (B) tensile and (C) fracture testing

Indirect tension (Brazilian) tests were carried out based on ASTM D3967 (2008) under ambient conditions on 15 x 30 mm (0.59 x 1.18 in) disc-shaped specimens obtained by cutting the vertical core plugs. In this way, the tensile strength is obtained in an orientation across bedding (Figure 13(B)). Specimens were loaded diametrically to failure, and the tensile stress (σ_t) developed in the central region of the specimen is estimated as (3.1)

$$\sigma_t = \frac{2F}{\pi d L} \quad (3.1)$$

where F is the maximum force applied to the sample, d is the diameter of the sample, and L is the length of the sample. The tensile stress computed at the time of specimen failure was taken as the tensile strength. Four specimens were tested for each formation, with average values reported.

Fracture toughness was measured under ambient conditions using the semi-circular beam test (Kuruppu et al., 2014). Specimens were prepared from vertical core plugs, with the final orientation relative to bedding shown in Figure 13(C). The load was applied in a 3-point configuration, as illustrated in Figure 13(C) and the relationship between applied load and mode 1

stress intensity factor (SIF) is based on Kuruppu et al. (2014). The computed SIF at the time of failure is taken as an estimate of the mode I fracture toughness, K_{IC} . Four specimens were tested for each zone with averages reported.

3.4.3 Triaxial Tests at 90°C

Triaxial tests were conducted at 90°C using a Hoek-type triaxial cell modified to allow temperature control (Figure 6).

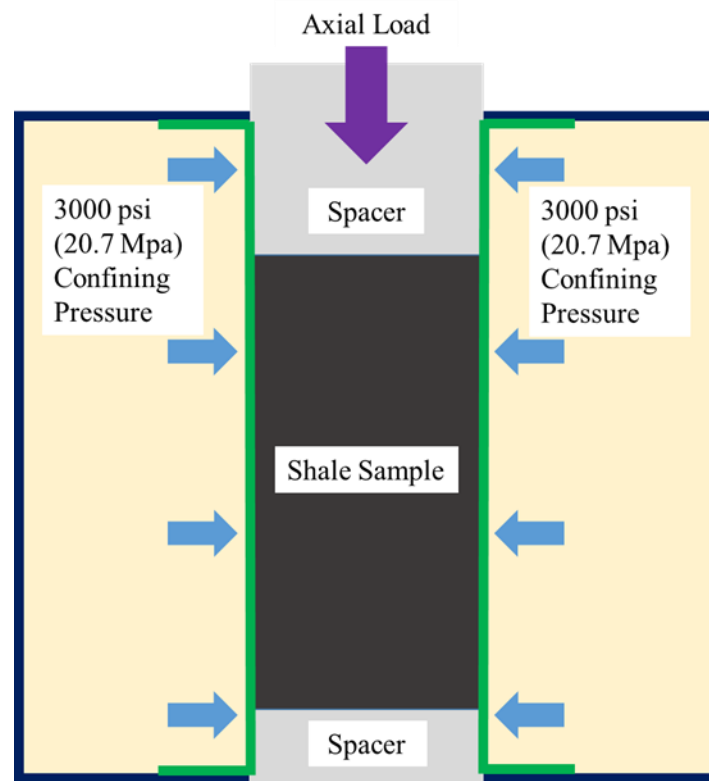


Figure 14 Schematic of triaxial test cell (heated externally) (from Bengte et al., 2023)

As in the UCS tests, vertical core plugs with size 30 x 60 mm (1.18 x 2.36 in) were used, selecting the most intact and homogeneous plugs based on pre-test CT scanning and visual

inspection. A vertical load was applied using an INSTRON 600DX load frame. Vertical and circumferential strain was measured using foil-type strain gages with gage length of 6.35 mm (0.25 in). Stress versus strain curves and ultimate stress at failure is obtained from a single test at each of three confinement levels for each formation. The confinement levels tested were 3.4, 10.3, and 20.7 MPa (500, 1500, and 3000 psi). Based on the obtained relationship between axial stress and confinement, the cohesion and friction angle are computed as

$$\Phi = \sin^{-1} \frac{m - 1}{m + 1} \quad c = b \frac{1 - \sin(\Phi)}{2 \cos(\Phi)} \quad (3.2)$$

where m and b are the slope and y-intercept of a line fit to the relationship between axial stress at failure and confining stress. Additionally, the Young's modulus (E) and Poisson's ratio (ν) are obtained from the linear portion of the stress-strain relationship, with Young's modulus calculated as the slope of the axial strain line and the Poisson's ratio as the change in axial over the radial stress, as in

$$E = \frac{\sigma_{axial}}{\epsilon_{axial}} \quad \nu = - \frac{\epsilon_{radial}}{\epsilon_{axial}} \quad (3.3)$$

where σ_{axial} is the applied axial stress, ϵ_{axial} is the measured axial strain, and ϵ_{radial} is the measured radial strain. Note in some cases the strain gages failed under the high stress, high temperature conditions and therefore E and ν are not obtained in these cases.

3.5 Results

3.5.1 Mineralogy

Results of XRD analysis of samples from each of the five zones are shown as relevant mineral components by weight in a ternary diagram in Figure 15. Reservoirs 1 and 3 showed the highest carbonate content. Examining the clay content of each identified zone, the two nominally ductile zones have greater clay content than the other zones. Note in all layers the predominant clay minerals are illite, muscovite and interlayered illite-smectite.

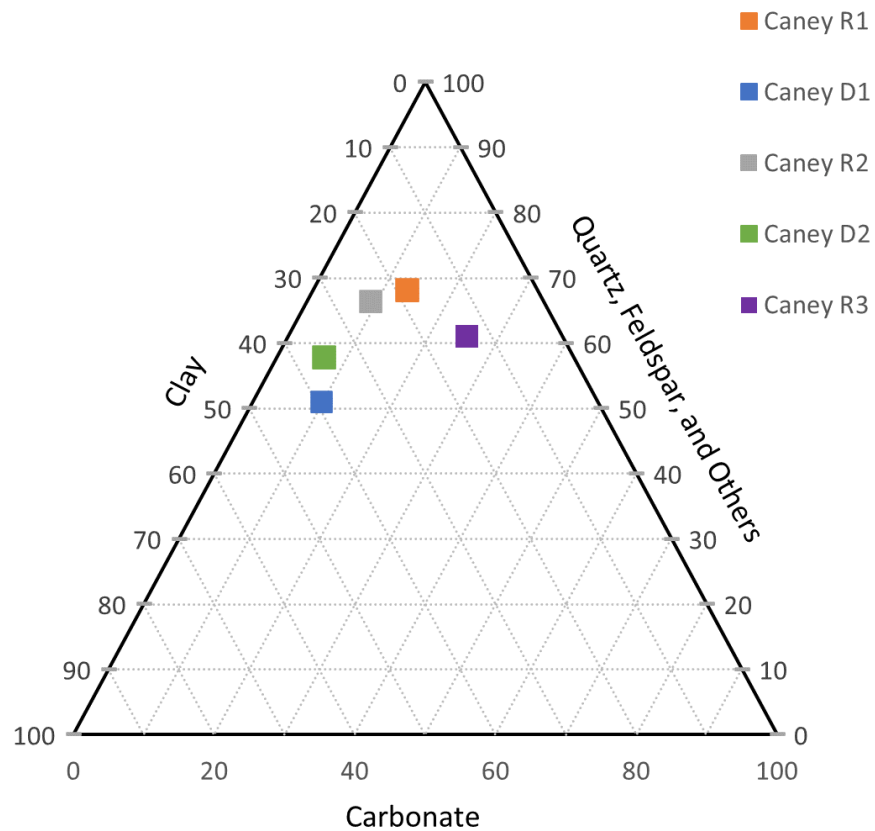


Figure 15 Ternary diagram of caney sample mineralogy

3.5.2 Strength Tests at Ambient Conditions

A summary of average values of UCS, tensile strength, and fracture toughness for each of the five formations is provided in Figure 16. It is notable the nominally ductile sections exhibit significantly lower strength in terms of all three quantities, even when experimental variation is taken into account. However, Figure 16 also shows the UCS and tensile strength are apparently reduced in such a manner their ratio is not correlated to nominally ductile formations, but rather stays similar in all formations and in the range 8-11.

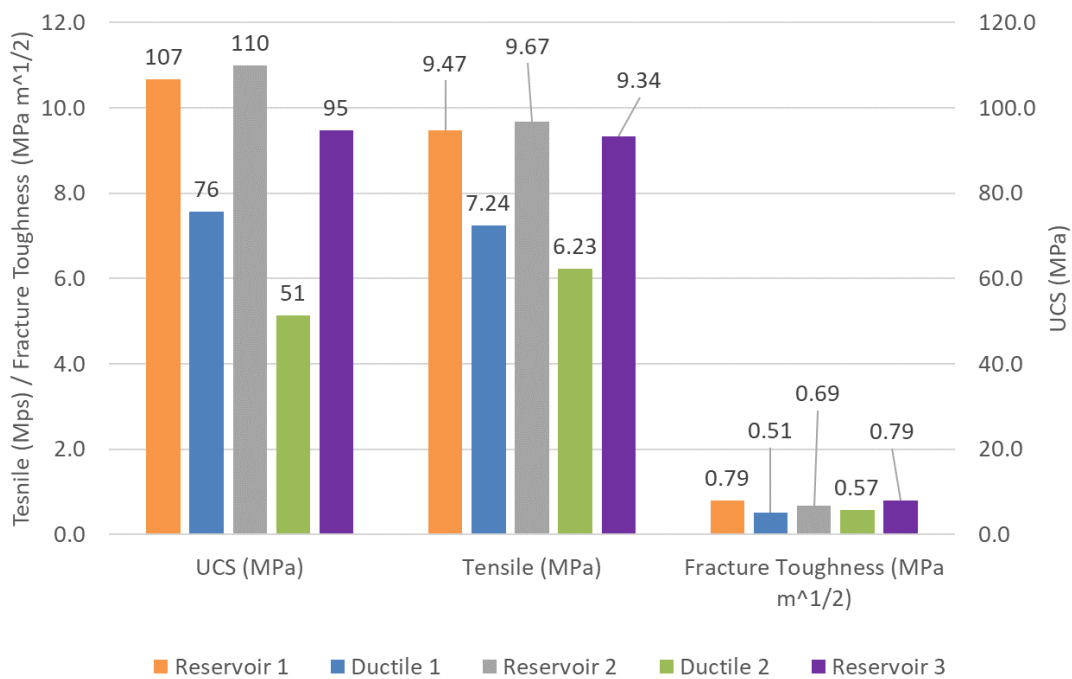


Figure 16 Summary graphs of unconfined properties

3.5.3 Triaxial Properties

Results of the triaxial tests are shown in Figure 17. There are a few things to note. Firstly, the nominally ductile formations track with lower strength compared to the identified reservoir formations. This is in spite of the fact cohesion and friction angle computed based on these graphs do not show systematic dependence on whether the formation is nominally ductile. This points to necessary caution which must be taken into account when summarizing experimental data in terms of fitted metrics. In this example, a Mohr-Coulomb criterion imposed upon the data with fitted values of cohesion and friction angle clearly do not capture the full story. Additionally, it is important to note the experiments would ideally be repeated multiple times at each load level. However, limitations on specimen availability preclude this check on repeatability, and so one must be cautious to conclude nominally ductile layers are somewhat weaker under triaxial testing. When compared to UCS data, the triaxial data illustrates the importance of temperature in the rock properties of the Caney shale. Extrapolating the confined test results in Figure 17(A) back to zero confinement, the estimated UCS would be substantially below the value obtained under ambient conditions. Hence, for all five formations, the rock appears to undergo a reduction in apparent strength as temperature is increased.

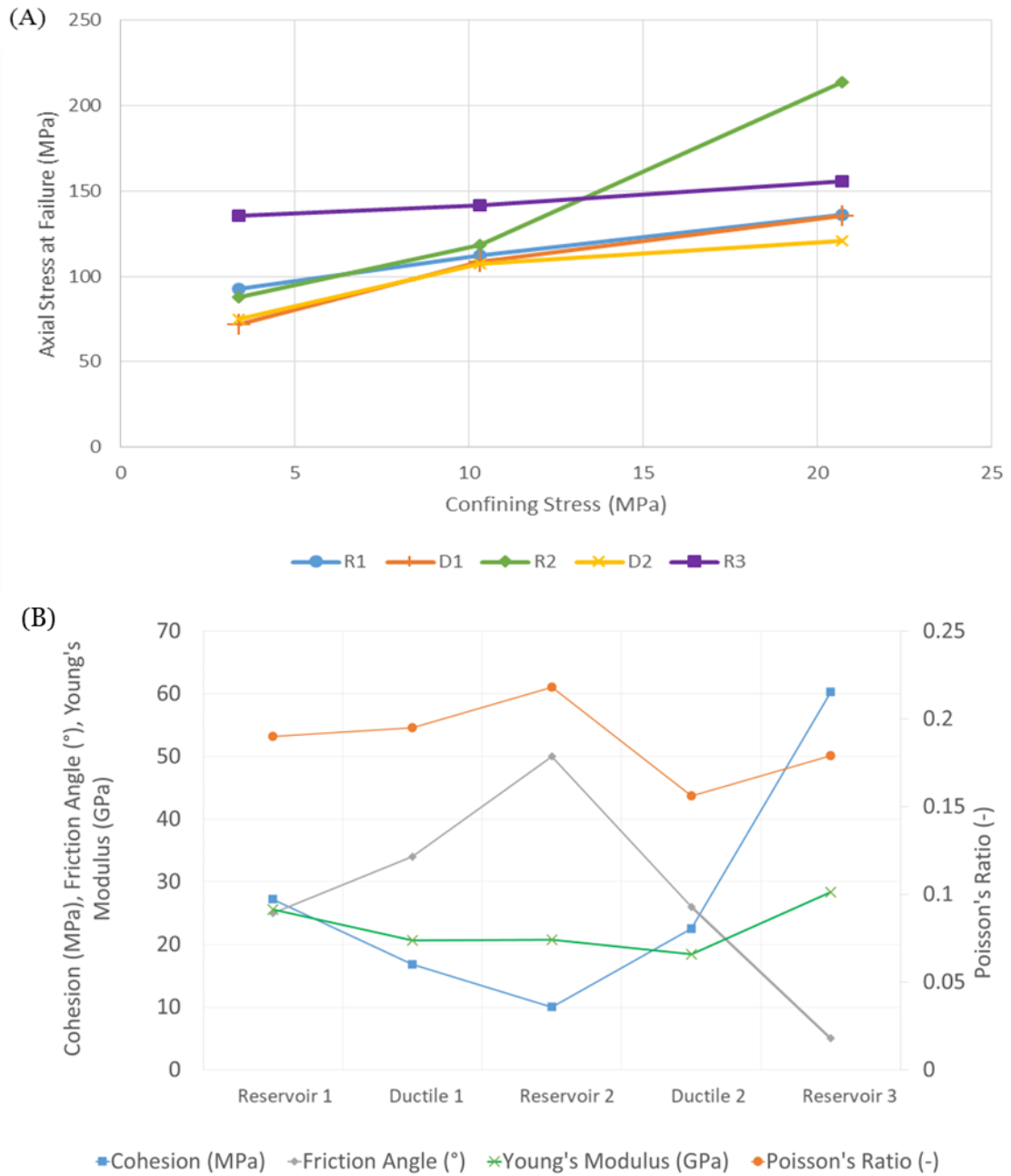


Figure 17 Axial failure stress vs confining stress for all zones (A) and average properties for each zone (B)

3.6 Brittleness Index

Multiple definitions can be used to determine a brittleness index, from an analysis of mineralogy to indentation test data to triaxial compression test data (see e.g. Bai, 2016, Hucka and Das, 1974, Rickman et al. 2008). For this paper, five brittleness index values are selected, representing: 1) A mechanical definition based on comparison of elastic and plastic strain during triaxial compression, 2) An empirical-mechanical definition based on observation brittle materials often have a smaller tensile strength relative to compressive strength, 3) An empirical definition based on elastic properties, a common definition defined in well log interpretation, and 4) A mineralogy-based definition, also commonly used in well log interpretation. Finally, the Irwin Length (squared ratio of fracture toughness to tensile strength) it is common in fracture mechanics to tie this quantity to expected size of the plastic region developing around the tip of a propagating fracture. These five quantities are therefore used to compare the nominally ductile zones to the reservoir zones.

The first brittleness index presented is based on the elastic and plastic strains noted during the loading phase of the triaxial compression test, BI_{strain} . This method, one of the earliest mechanical definitions of brittleness (Coates and Parsons, 1966 as summarized by Huca and Das, 1974) extrapolates the linear part of the stress-strain relationship to estimate the elastic strain. This is assuming elastic behavior is linear and no elastic (recoverable) deformation is associated with nonlinearity in the stress-strain. Hence, this approach compares the extrapolated elastic strain to the total strain at the moment of incipient failure of the specimen. Examples are shown in Figure 18, illustrating firstly the behavior of Ductile 1 in which most of the strain is inferred to be elastic up to the point of failure. This is in contrast to Reservoir 2 where a more substantial portion of the strain is inferred to be plastic. By definition (Table 1), a perfectly brittle material with no ability

to yield would have a BI_{strain} of 1, while a very ductile material will have a value approaching a limit of zero.

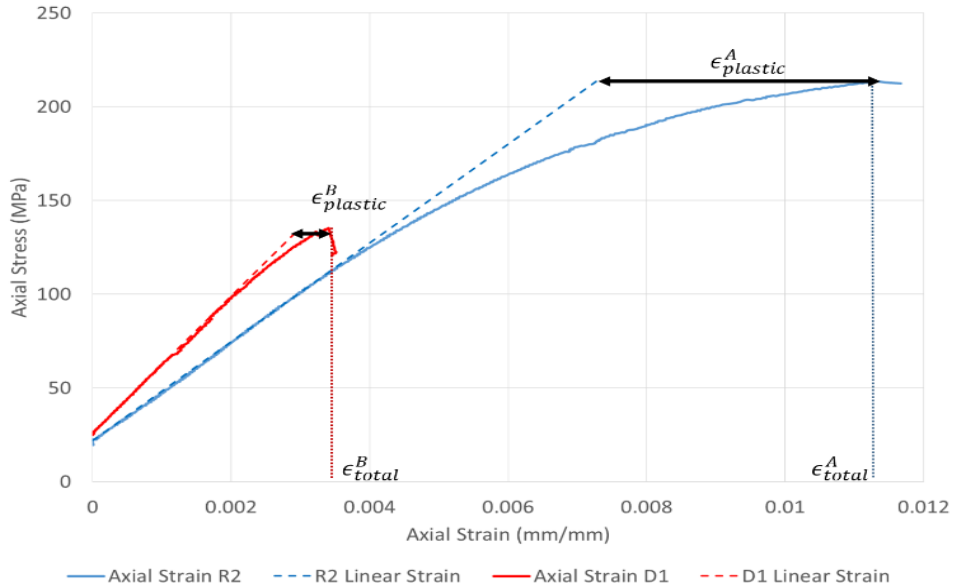


Figure 18 Example tests with plastic axial strain ($\epsilon_{plastic}$), and total axial strain ϵ_{total} , for (A) Reservoir 2 and (B) Ductile 1 tested at 20.7 MPa (3000 psi) confining pressure

A second method, $BI_{strength}$, to determine brittleness uses the unconfined compressive (σ_c) and unconfined tensile strengths (σ_t) (Hucka and Das, 1974). In this definition, $BI_{stress} = 0$ corresponds to the case where the strength is the same in compression and tension, and $BI_{stress}=1$ corresponds to the limit where the tensile strength is negligibly small compared to the compressive strength.

Table 1 Brittleness Indices and Irwin length for each formation, triaxial test results values are taken from 20.7 MPa (3000 psi) confinement

Parameter	BI _{strain} Hucka and Das, 1974	BI _{strength} Hucka and Das, 1974	BI _{mineralogy} Jin et al. 2014	BI _{elastic} Rickman et al. 2008	Irwin length (mm) Lecampion, 2012
Formula	$\frac{\epsilon_{total} - \epsilon_{plastic}}{\epsilon_{total}}$	$\frac{\sigma_c - \sigma_t}{\sigma_c + \sigma_t}$	$\frac{(W_{other} + W_{carb})}{W_{total}}$	Eq. 3.4-3.6	$\frac{K_{IC}^2}{\sigma_t^2}$
Zone					
Reservoir 1	0.88	0.84	0.82	0.36	6.98
Ductile 1	0.86	0.83	0.61	0.50	4.92
Reservoir 2	0.64	0.84	0.75	0.29	5.02
Ductile 2	0.91	0.78	0.65	0.55	8.31
Reservoir 3	0.98	0.82	0.87	0.60	7.17

A third brittleness index is provided by Rickman et al. 2008, BI_{elastic}, which uses the Young's modulus and Poisson's ratio values. Typically these are applied using sonic log data in order to map this metric of brittleness along a section of wellbore. It is defined relative to the maximum and minimum values of Young's modulus and Poisson's ratio in the section of interest, as in

$$E_{unit} = \frac{E - E_{min}}{E_{max} - E_{min}} \quad (3.4)$$

$$v_{unit} = \frac{v - v_{max}}{v_{min} - v_{max}} \quad (3.5)$$

$$BI_{elastic} = \frac{E_{unit} + v_{unit}}{2} \quad (3.6)$$

where E and v are the section's Young's modulus and Poisson's ratio and the subscripts indicate the minimum and maximum recorded values for all the examined samples. For comparison with

the other brittleness values, the numbers in Table 1 are all obtained from the 20.7 MPa (3000 psi) confined triaxial properties and values are normalized only to the measured values at this confining pressure. A higher $BI_{elastic}$ value indicates a relatively more brittle part of the formation while a lower value indicates sections which are relatively more ductile.

A fourth definition of brittleness, $BI_{mineralogy}$ (Table 1), uses the weight percentages of clay, carbonate, and other (i.e. quartz and other non-carbonate, non-clay) components (Jin et al. 2014). The more clay components in a given shale sample, the smaller proportion of carbonates, quartz, feldspars, and other more brittle materials ($W_{other} + W_{carb}$). By comparing the amount of non-clay components to the total material in the sample, W_{total} , the brittleness is determined essentially by examining the amount of clay in the sample. More ductile materials tend to have larger amounts of clay and will have a $BI_{mineralogy}$ closer to zero while a more brittle material with essentially no clay components would have a value closer to one. This method is simple and does not require intact core samples to calculate but is susceptible to noise in the measurements and ideally would be validated against additional methods. Furthermore, it does not account for the impact of grain/mineral structure, nor does it account for the fact different clay minerals have very different morphology, surface chemistry, and overall impact on mechanical behavior.

In contrast to the brittleness index, the Irwin length (Table 1) is a metric often used in fracture mechanics to estimate the size of a zone of inelastic deformation (“process zone”) which develops around the tip of the propagating fracture. For a material exhibiting perfectly brittle fracture behavior, the size of this process zone will become vanishingly small. So, by this measure, a formation with smaller Irwin length should be considered more brittle from a fracture mechanics perspective (Lecampion, 2012). This metric uses the tensile strength (σ_t) and the fracture

toughness (K_{IC}) value from material testing. The calculated brittleness index and Irwin length for each zone is shown in Table 1.

3.7 Discussion

Brittleness measurements have various degrees of connection to mechanics as well as various levels of availability in typical well characterization. The mineralogy and elasticity based indices are often available from logging data. On the other hand, the measures obtained through mechanical experiments on core are seldom available, but arguably can be more directly connected to the mechanisms underlying performance of a reservoir including effectiveness of stimulation. For example, some fracture processes associated with hydraulic fracturing can be connected to the Irwin length. This includes size effects impacting fracture initiation and interpretation of fracture initiation pressures (Lecampion, 2012). Additionally, proppant embedment can be connected both to plastic strain (indicated by BI_{strain}) and shear strength of the rock (indicated by the friction angle) (see e.g. Alamaahi and Sundberg, 2012, Ming et al., 2018, and Deng et al. 2014). While directly making such connections is beyond the scope of the present discussion and is an area of active research, it is nonetheless of interest to investigate if the more available measures ($BI_{elastic}$, $BI_{mineralogy}$) may provide useful indications of rock brittleness according to other mechanically-based measures.

It is important to note the strength-based measure of brittleness ($BI_{strength}$) is ostensibly the same for all formations, within the bounds of experimental variability. In other words, in spite of the other variable properties and indices discussed here, the relationship between tensile strength and unconfined compressive strength (UCS) is very similar from one formation zone to another.

Interestingly, both tensile strength and UCS of the nominally ductile formations is smaller, which could impact a variety of engineering processes. However, the ratio of UCS to tensile strength remains in the range 8-11 with no systematic correlation of larger or smaller values of this ratio (Figure 16). By this measure, the nominally ductile formations appear to be weaker (at least in properties measured at room temperature and without confinement) but not substantially different in terms of brittleness. Nonetheless, it is striking to note formations identified as nominally “ductile” based on log-derived Poisson’s ratio, gamma ray, and resistivity strongly align with lower UCS, tensile strength, and fracture toughness.

XRD analysis suggests clay and quartz are dominant across all the investigated depths in Caney, whereas carbonate occurrence is localized in concretions and discrete layers. Similar mineralogy to the Caney is observed from Radonjic et al. (2020), Kamann (2006), and Schad (2004). Detailed clay mineralogy from Kamann (2006) and Schad (2004) suggest high illite and illite-smectite mixed layers, which is confirmed using the XRD analysis. Based on the well log and the mineralogy of collected samples, calculated $BI_{\text{mineralogy}}$ indicates the three reservoir zones are more brittle than the two zones identified as nominally ductile. In addition, observable differences in strength are clear both in confined tests at 90°C and unconfined experiments at room temperature. However, none of the brittleness metrics in Table 1, other than $BI_{\text{mineralogy}}$, show systematically lower BI in the nominally ductile zones. Taking this fact into account, there is general lack of correlation between $BI_{\text{mineralogy}}$ and other brittleness measures ($R^2 < 0.50$ for all cross plots). So, other measures give different indications of the most brittle and most ductile zones. Based on proportion of non-linear strain, BI_{strain} indicates Reservoir 3 is the most brittle and Reservoir 2 is the most ductile zone. The same is predicted based on elastic properties using BI_{elastic} . In contrast, some have suggested another measure of brittleness, $BI_{\text{friction}} = \sin(\Phi)$ where

Φ is the friction angle (e.g. Hucka and Das, 1974). This metric points to a contradictory conclusion, namely Reservoir 2 as the most brittle and Reservoir 3 as the most ductile of the zones (Table 1). The Irwin length points to Ductile 1 as the most brittle and Ductile 2 as the most ductile zone. The strength based BI_{strength} is ostensibly the same for all zones.

The contradictions presented by various measures of brittleness clearly point to the possible pitfalls associated with summarizing rock behavior using simple indices, especially when those indices have their origins in empirical observations and/or partial mechanical models. The need for a more complete consideration of plasticity, including full development of cohesive and frictional strength, when discussing rock brittleness has been argued in the context of tunnel stability (Hajiabdolmajid and Kaiser, 2003). Such approaches almost certainly have relevance as a path to reconciling disparate measures of brittleness around a more unified view and is more readily applicable to petroleum development issues such as wellbore stability and proppant embedment in hydraulic fractures during production.

Taking the limitations of brittleness index into account, and with the caveat of the limited data presented in this paper, there are potential lessons to be learned by examining the relationships among brittleness indices obtained from these experiments in the Caney shale. As previously mentioned, $BI_{\text{mineralogy}}$ does not correlate with any other brittleness measure. However, BI_{elastic} , which is popular because it can be computed based on interpretation of sonic log data, does have some interesting correlations over the five formations considered in this study (Figure 19). The most striking correlation is a very strongly correlated ($R^2 = 0.91$) relationship between BI_{elastic} and BI_{friction} (recalling the latter is calculated as the sine of the friction angle). While this is significant, what is even more striking is how it is negatively correlated, not positively correlated to this

quantity. In other words, for these rocks, the sections identified as the most brittle based on elastic properties would be identified as the least brittle based on friction angle.

Furthermore, there is a reasonable, positive correlation ($R^2 = 0.71$) between BI_{strain} and BI_{elastic} . This empirical correlation indicates the rocks identified as most brittle based on elastic properties would be the same rocks which would tend to deform linearly up to the point of failure, rather than undergoing softening prior to complete loss of failure.

Finally, it is notable BI_{strain} and BI_{friction} are inversely correlated. This indicates, for this study, rocks with the smallest friction angle tend to deform linearly up to the point of failure while those with the largest friction angle tend to undergo nonlinear softening prior to failure.

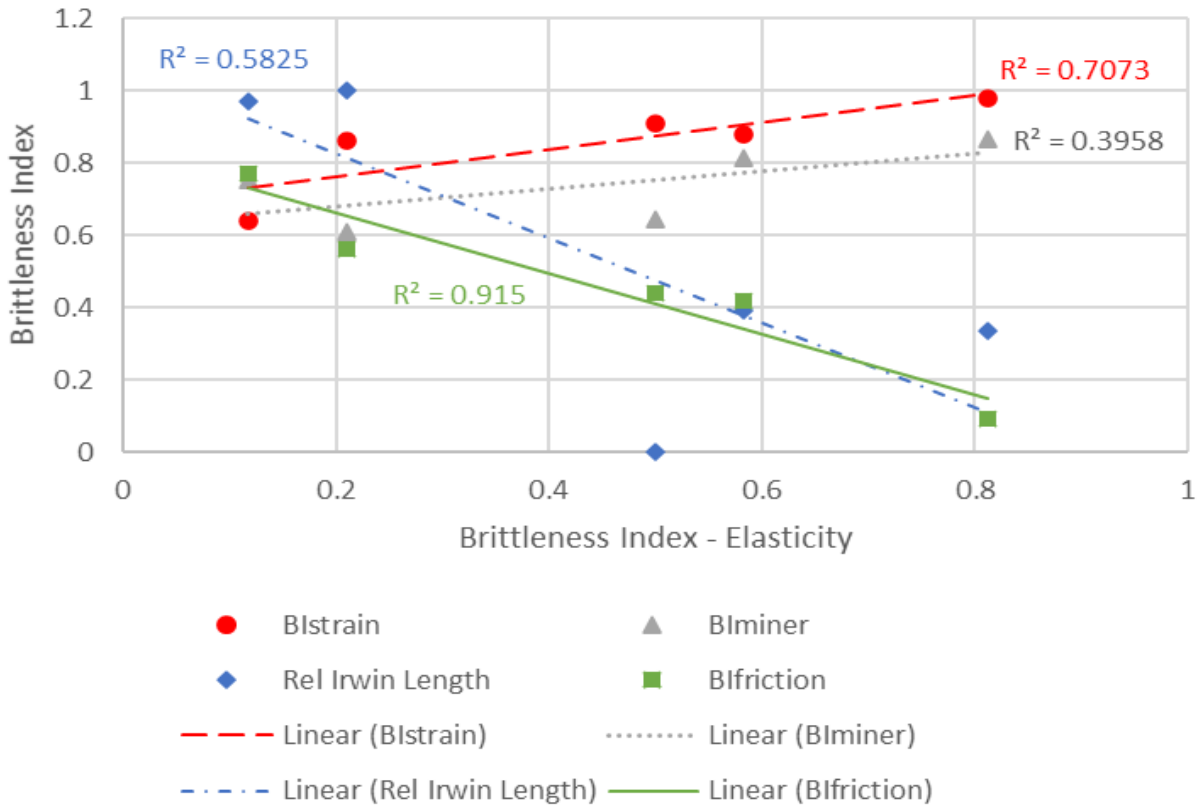


Figure 19 Cross-Plot of various Brittleness Index values, noting the relative Irwin Length gives the absolute value of the difference between the Irwin Length and the smallest Irwin Length, normalized by the difference between maximum and minimum Irwin Length, mapping to the range 0 to 1 with 1 being the most brittle

3.8 Conclusions

Open-hole logs lead to a nominal distinction of five zones in an exploration well, two of which were designated “ductile” and three of which were designated as less ductile “reservoir”. These distinctions are based on petrophysical properties, not directly on mechanical behavior of rocks as they yield and undergo inelastic deformation. The designation is a conjecture by its nature. Nevertheless, the nominally “ductile” zones are weaker in terms of UCS, tensile strength, fracture toughness, and confined compressive strength. Hence there is some usefulness to the distinction.

While there may be some pragmatic justification of “brittle” and “ductile” zoning of reservoirs, in this case study, the terminology “ductile” versus “brittle” does not align with mechanical behavior observed in experiments. Instead, by a variety of brittleness indices, it is found the nominally “ductile” regions do not behave as expected. They might be weaker, but not consistently more ductile. Furthermore, some brittleness indices lead to contradictory conclusions. For example, zones which would be considered the most brittle according to the proportion of nonlinear stress-strain behavior prior to failure would be considered the least brittle according to their internal friction angle. Additionally, mineralogy, over the rather limited range observed in these five formations, appears to not be predictive in terms of brittleness by any other measure.

Taken together, the conclusion to the original question of the veracity of brittle-ductile distinction based on petrophysical logging data is mixed and comes with the caveat of its limitation to a single case study. In this regard, it appears the terminology “brittle” and “ductile” are ambiguous and prone to self-contradiction. However, the distinction itself was able to identify strong and weak zones based on ostensibly dissimilar data such as sonic and dielectric properties. So, in this case, it would be truer to the underlying rock behavior to distinguish these as “weak” and “strong” zones, noting “brittleness” is a matter of engineering objective and the corresponding metric (i.e. brittleness index) is used to compare rocks in a given engineering context.

Based on the properties determined through unconfined and triaxial testing, the most predictive brittleness index was mineralogy. However, both the content and morphology of the clay should be considered when predicting the behavior of a formation. For example, a well-distributed clay will result in a material which is easily deformed, while clay particles surrounded by a significantly stiffer rock matrix will be relatively more difficult to deform. Taking this caveat into account, if only one brittleness index were available to be used for differentiating between

“ductile” and “brittle” zones, the index with respect to mineralogy has the greatest chance of providing useful information with respect to fracturing a formation.

4.0 Creep Properties and Proppant Embedment

This chapter presents previously published work examining the relationship between creep properties and the prediction of proppant embedment and fracture closure. As the creep properties are used to describe the long-term deformation of the formation, they are vital to predicting fracture closure. The work presented in this chapter was completed prior to the completion of creep testing, and therefore only the vertical samples (drilled perpendicular to bedding) are included. However, as the relative behavior of the formations is similar, where the ductile zones are significantly more prone to creep than the reservoir zones, the conclusions are also applicable to the horizontal properties. Because this work was previously published as a stand-alone document, topics are presented again when needed for context and discussion.

The main focus of this chapter is the influence of creep properties on predicted proppant embedment and fracture closure. Fracture closure and formation deformation were predicted with a model used by a collaborator at Lawrence Berkely National Laboratory (Pruess et al., 2012, Itasca, 2011, and Rutqvist, 2011 and 2017). It should be noted the model was developed and run by J. Rutqvist with creep properties determined using laboratory testing used as an input in the model. The closure of fractures over time significantly impacts the overall hydrocarbon production, as a partially closed fracture will restrict the flow of hydrocarbons more significantly than a fracture which is fully open. Additionally, the microstructure of the formation is examined, and as with the initial analysis using the Brittleness Index, it is found there is a correlation between the amount of clay in a given sample and the tendency of the sample to experience long-term deformation. Critically, the clay must be well distributed for this relationship to be valid, as clay

particles surrounded by stiffer materials would not be able to deform but clay particles dispersed as part of the main fabric of the rock would be able to easily deform under applied stresses.

Predicting the amount of proppant embedment and fracture closure over time identifies the expected production for a fracture. In addition to the decline in production caused by the removal of hydrocarbons close to the fractures, a slowly closing fracture or a formation undergoing damage due to proppant embedment results in a significant decrease in overall hydrocarbon production. If a fracture in a particular zone in the formation will be entirely closed in a relatively short period of time, the cost of stimulating the formation in this zone may not equal the profit from production. Similarly, if the fracture closes in a slow enough length of time the zone is profitable, but after a given number of years the amount of production has reduced lower than a desired minimum, the zone can be refractured to increase the amount of production and extend the life of the well. By understanding the behavior of the formation with respect to proppant embedment and fracture closure, it is possible to predict these two mechanisms, and design a stimulation plan both in terms of target zones and in terms of potential future treatments to ensure a profitable amount of hydrocarbon extraction.

This chapter presents work previously published in a paper titled “Creep Properties of Shale and Predicted Impact on Proppant Embedment for the Caney Shale, Oklahoma”, published in *Rock Mechanics and Rock Engineering*. Two significant edits have been made, which include the addition of the 10.55 MPa (1500 psi) triaxial data to Figure 29 and the addition of creep testing for horizontal and 45° samples, detailed in Section 4.9. While additional minor modifications have been made to the previously published work, the copyright for the original journal article remains with Springer.

4.1 Chapter Summary

The Caney shale is an emerging hydrocarbon play located in southwest Oklahoma, USA. Within the Caney shale exist facies which were initially dubbed “reservoir” and “ductile” based on evaluation of well logging data. While past work has shown the distinction of “brittle” and “ductile” is not mechanically justifiable according to formal definitions, the current work shows some important differences between nominally ductile and reservoir zones. First, the “ductile” zones are more clay rich and have textural differences which can be expected to lead to differences in mechanical properties. One important impact of these differences is observed in triaxial creep experiments showing the “ductile” zones are more prone to creep deformation. Numerical simulations predict the “reservoir” zones will experience very little proppant embedment due to creep deformation of hydraulic fractures around proppant particles. On the other hand, “ductile” zones can be expected to undergo creep-driven proppant embedment leading to loss of fracture aperture ranging up to 100% loss, depending upon the spatial density of the proppant distribution. This research shows the identification of nominally “ductile” zones from well logs, while a misnomer, can be useful in finding clay-rich, creep-prone zones which will be the most prone to proppant embedment and hence vulnerable to greater production decline over time.

4.2 Introduction

Located in southern Oklahoma below the Springer shale and above the Woodford shale, the Caney shale is an emerging shale play under examination for hydrocarbon production (Cardott, 2017). A high clay content and the increased potential for ductile behavior in some segments of

the formation imply this shale formation may be more difficult to produce than other shale plays currently in production. Although the Caney shale vertical core does have regions where clay content is sufficiently lower, this is compensated by an additional presence of carbonates and quartz (Awejori et al., 2021, Radonjic et al., 2020, and Wang et al., 2021). With this zonation, it can be proposed to distinguish some subunits within the Caney shale as “ductile”, and other subunits as nominally more “brittle” and hence more promising as “reservoir” rocks. However, previous research work has shown the Caney shale is not “ductile” according to the traditional brittle/ductile definitions in rock mechanics (Benge et al., 2021). Nonetheless, despite the fact this labeling is a misnomer, distinguishing “brittle” and “reservoir” zones has practical relevance, especially as it is able to label zones as relatively stronger/weaker (Benge et al., 2021) and more susceptible to creep deformation over time, as is the focus of this chapter.

The creep deformation associated with the “ductile” zones has clear connections to the effectiveness of formation stimulation through hydraulic fracturing, most notably due to its impact on the distribution of in-situ stresses (see Sone and Zoback, 2014a), the closure of fractures over time, and the embedment of proppant material (see review of Bandara, 2019, Katende et al., 2021a, and Frash et al., 2019). This chapter focuses on the impact of creep on proppant embedment, using elasto-viscoplastic simulations to predict five-year proppant embedment to contrast a “reservoir” zone which undergoes little creep deformation with a “ductile” zone which is highly prone to creep deformation. Hence, this chapter provides not only predictions specific to the Caney shale, but also provides an illustrative test case showing how subunits within a reservoir can behave very differently depending on their geomechanical properties in general and their propensity to undergo creep in particular. While the conclusions presented in this chapter are limited by the number of

available samples, the methodology aims to provide a framework for full characterization of formations including mineralogical analysis, triaxial testing, and creep testing.

Simulations of creep-accommodated proppant embedment require experimental characterization. For this reason, the present work entails creep compliance testing under triaxial loading conditions and at elevated temperatures approximating those relevant to reservoir conditions. The multi-stage creep compliance tests are modified from Rassouli and Zoback (2018), and the data is shown to lend itself to a power-law creep model which is readily implemented in the numerical simulations. Samples are tested from three nominal “reservoir” zones and two nominal “ductile” zones, enabling comparing and contrasting of these zones in terms of their propensity for creep deformation.

Besides the testing of creep properties and connecting these to predictions of proppant embedment, there are additional connections of interest. The first is to examine the effectiveness of well-log based identification of nominally “reservoir” and “ductile” zones to determine the sections of the reservoir which are most promising for sustained production. The second is to examine the differences in mineralogy and microstructure among the identified zones. Ties can therefore be proposed both to mineralogy (for example clay content and/or organic content) and to the fact the same quantity of minerals can occupy the rock volume differently. This microstructure takes into account the internal architecture of the rock matrix, where porosity and natural fractures also contribute to how rock may respond to physical and/or chemical changes at different spatial and temporal scales (Wang et al. 2021). Hence, this chapter includes a detailed description of both mineralogy and microstructure because it is ultimately a key factor in determining the macroscopic properties measured in mechanical tests and considered by the numerical simulations. Furthermore, by providing an integrated case study of connections among

log-derived properties, mineralogy, microstructure, creep, and predicted tendency for proppant embedment, the present work can be relevant not only to the Caney shale, but also can provide an illustrative case to act as a template for similar studies on other formations.

By way of organization, this chapter firstly describes the core and the exploration well from which it was extracted. It then identifies five formation subunits as either “reservoir” (expected to be more brittle) or “ductile” based on the elastic properties as determined by the well log. Next, samples obtained from the core are described in terms of context, meso/micro-scale structures, mineralogy, and triaxial strength. These all provide the context by which mechanical properties can be different among the various zones. The chapter then focuses on creep compliance tests, showing the differences from each zone and providing a power-law description of creep unique to each zone to be used in numerical simulations. Finally, taking characterization from the mechanical testing, an elasto-visco-plastic mechanical model is used to predict proppant embedment. This model provides the backdrop to a closing discussion of the synthesis of log data, mineralogy, microstructure, mechanical testing, and numerical simulation. These are examined with the goal of predicting the most promising and most problematic zones within a reservoir from the perspective of sustaining production through propped hydraulic fractures.

4.3 Core Description

4.3.1 Well Location and Sampling Program

The Caney shale is located in the Arkoma basin in southern Oklahoma, USA. A recent exploration well (completed in February 2020 and described in more detail by Katende et al., 2023)

intersected approximately 152 m (500 feet) of the Caney shale formation. The formation characterization began with determining petrophysical properties from an open-hole well log. Five zones of interest were identified based on these properties, most notably the Poisson's ratio but also including electrical resistivity and gamma ray radiation. From shallowest to deepest, the zones were identified as Reservoir 1 (R1), Ductile 1 (D1), Reservoir 2 (R2), Ductile 2 (D2), and Reservoir 3 (R3), as shown along with well log data in Figure 20. For the purpose of naming, the "reservoir" zones have a Poisson's ratio less than 0.25 (indicated by yellow shading in Figure 20), have a low gamma, and have a high resistivity. Note a low value of Poisson's ratio has been associated with microseismically "brittle" zones in the past (e.g., Rickman et al., 2008) while low gamma and high resistivity are typically associated with low clay content (see for example Fadjarjanto et al., 2018) which, in turn, is considered to be associated with higher brittleness (e.g. Bai, 2016).

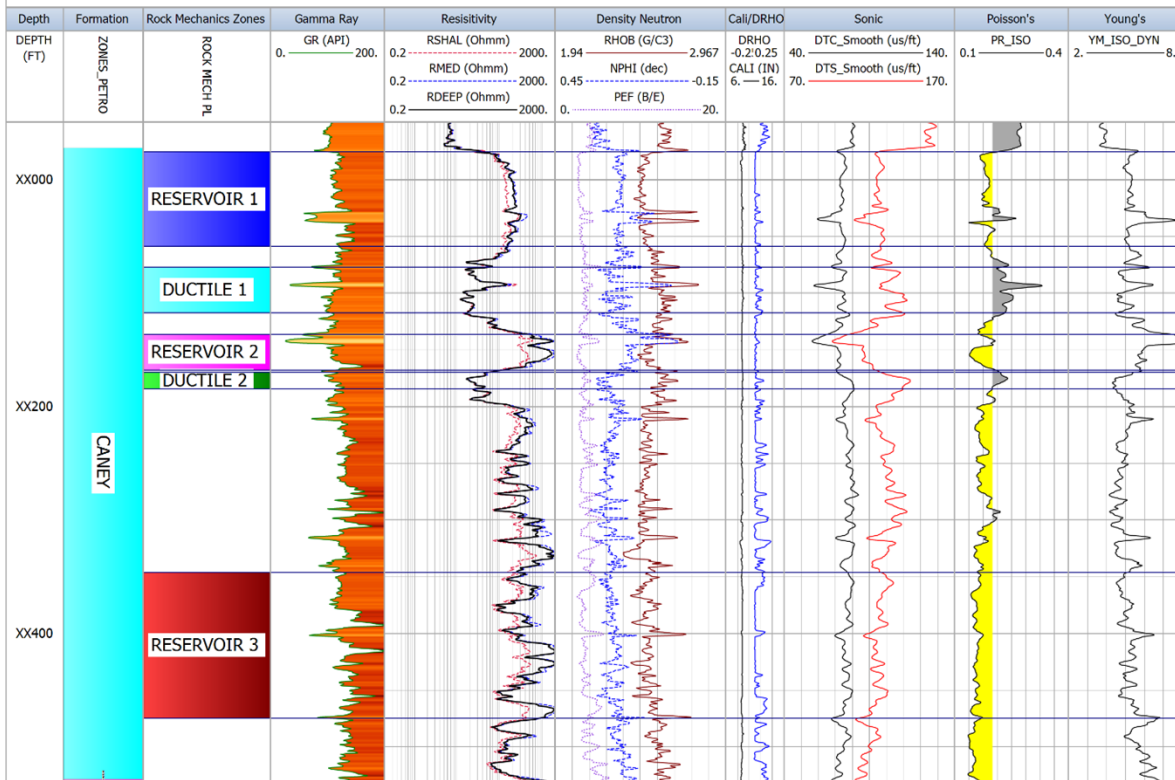


Figure 20 Well log with identified zones indicated by different colored name boxes, note the variation in Poisson's ratio between the Ductile and Reservoir zones

In total, 198 m (650 feet) of 10.2 cm (4 inch) core was retrieved from the 2020 exploration well. From this 10.2 cm core, cylindrical samples (“core plugs”) were obtained from each of the five zones. The core plugs have dimensions 30 mm (1.20 inches) diameter by 60 mm (2.36 inches) long. While multiple orientations of core plugs were taken, here are presented the results obtained from plugs with the main axis perpendicular to bedding planes (vertical core plugs). After the ends were surfaced to create parallel faces, samples were CT scanned to identify any flaws or debonding of bedding planes prior to preparing the samples for testing.

In addition to providing quality control for triaxial and creep testing, CT images of the samples can provide an idea of bulk heterogeneity. The bright white carbonate and pyrite grains in the sample-scale CT scans of Figure 21 are contrasted by the darker fine-grained clay matrix.

While the industrial CT scanner used in these images lacks sufficient resolution to depict microstructural features such as nano-porosity, these values can be obtained using other methods such as scanning microscopy. Unfortunately, the resolution of the CT scanner was unable to show a clear distinction between the nominally brittle and nominally ductile zones, and there were no significant differences between the zones when viewing the core without the use of any visual enhancements.

Although minor partings can be observed on bedding planes and R2 and D2 are shown to have more variation in density among layers, Figure 21 shows the samples are overall intact and lack pre-existing fractures at orientations which would be prone to slippage under triaxial loading. Prior to testing, samples were stored in sealed bags and while a small amount of surface drying may have occurred during experimental setup, the samples are treated to be at an “as received” saturation level.

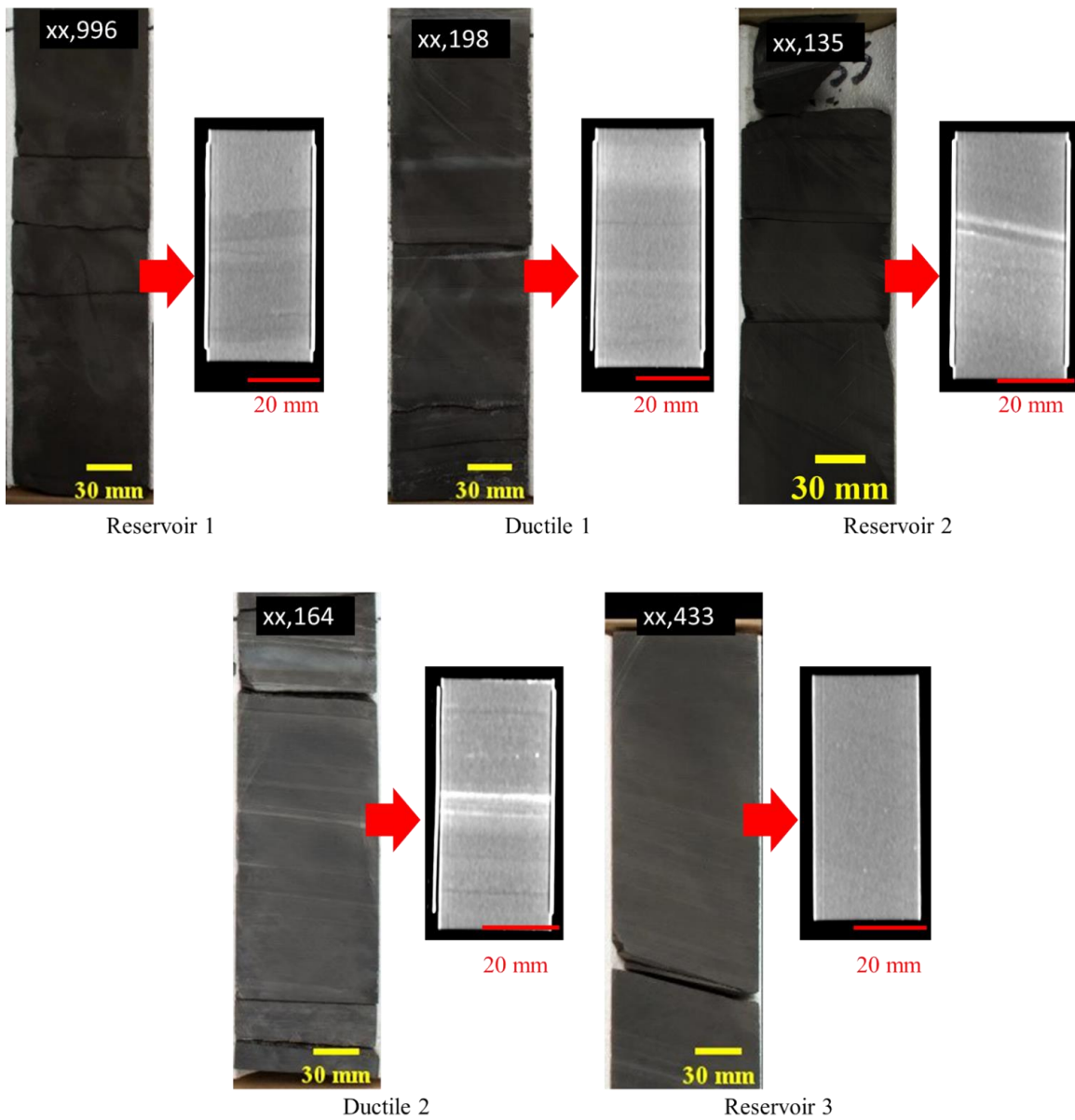


Figure 21 Photographic images of the section of 10.2 cm core sampled by core plugging for each zone along with X-Ray computer tomography scans of example 30 mm diameter core plugs used for quality control during sample preparation

4.3.2 Mineralogy and Microstructure

For geomechanical testing, proppant embedment, and characterization, samples were selected from the same zones as identified previously. In addition, XRD analysis was completed on 120 core samples across the approximately 198 m of available core. Eight horizontal plugs were drilled from the Reservoir 3 zone and thin sections were made from 180 locations. The inherent inhomogeneity present in all sedimentary rocks was accounted for by averaging multiple measurements from samples located throughout the five zones of interest.

At each of the selected zones shown in Figure 20, two grams of crushed rock powder were used to identify the bulk mineral composition with a Bruker D8 Advanced X-ray Diffraction (XRD) instrument at Oklahoma State University Laboratory which is coupled with a Lynxeye detector. Each sample was scanned from 5 to 80 degrees 2-theta angle with 0.01 degree step and dwell time of 0.5 seconds. Semi-quantitative analyses were obtained using the Bruker's Diffrac.suite eva. As can be observed in Figure 22, the mineralogical composition of these Caney shale samples matches what was observed from petrophysical well logs, with the reservoir sections (R1, R2, and R3) having low clay content (18, 25 and 13 weight%) and relatively high carbonate content (14, 19 and 26 weight%), and clearly separating the Reservoir 3 (R3) region as the most favorable for fracturing and subsequent hydrocarbon production based on the criteria determined using the well log.

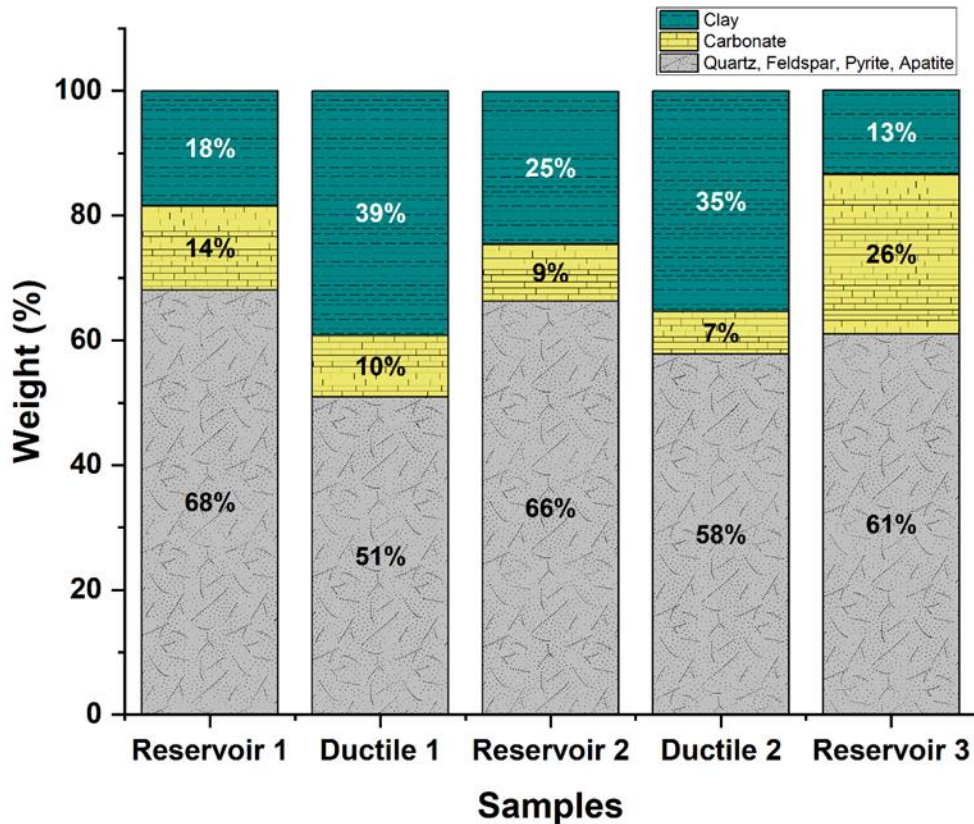


Figure 22 Mineralogical composition of the Caney shale samples in the identified zones

Moving beyond mineralogy, the microstructural characterization entails obtaining 2.54 cm (1 inch) diameter by 1.27 cm (0.5 inch) high disc-like samples from each zone. These were polished and coated with carbon prior to scanning electron microscopy (SEM) analysis for elemental mapping and back scatter electron micrographs. To avoid clay-water interaction, a specially designed protocol was developed for polishing, using an Allied HighTech multiprep polisher to prepare flat sample surfaces for SEM imaging. First a 600 grit silicon carbide abrasive disc was used for grinding to remove initial roughness. After each step, the surfaces were inspected under the microscope to ensure a uniform polished pattern. Grinding-induced deformations were removed using 6 μm diamond suspension on gold label polishing cloth and 1 μm diamond suspension on white label polishing cloth, with purple lube. To avoid the water-sensitivity of shale

samples, the commercial lubricant sold as Purple Lube was used. Purple Lube is a low viscosity, ethyl alcohol-based polishing lubricant. The final polishing was achieved with 0.05 μm water-free colloidal silica suspension used on a Chem-Pol polishing cloth. Polished samples were then dried in an oven at 50 °C before a conductive coating was applied prior to SEM/EDS analysis.

SEM imaging was then carried out using an FEI Quanta 600 field-emission gun Environmental Scanning Electron Microscope in both backscattered and secondary electron mode. The elemental mapping and spot mode analysis were obtained using a Bruker EDS X-ray microanalysis system. SEM images and spectra were obtained at 20 kV and various magnifications, from a larger field of view to a higher magnification to reveal the characteristics of interfaces and surface properties of various phases. Scanning electron microscopy determines the two-dimensional spatial distribution of inorganic (mineral) and organic (kerogen) content and the presence of porosity and micro fractures. Figure 23 through Figure 27 show the microstructural characterization of each zone. Chemical elemental maps were obtained using EDS, primarily to provide an insight into the degree of compositional heterogeneity in each of the five zones. The as-received samples from reservoir and ductile zones differ primarily in grain size, porosity, and composition, as is to be expected due to the difference in depth caused by the different depositional environment and the impact of geological activities related to uplifting and fluid migration over geological times. A specific examination of each zone provides insight into the unique properties of each sample.

The Reservoir 1 sample shown in Figure 23 provides an average 350 by 300 μm field view, a medium range resolution capable of capturing the compositional arrangement, micro-porosity, and micro fractures of the sample. The sample shown is rich in quartz and carbonates and has large conglomerations of pyrite well distributed in the matrix of clays. This characteristic is seen

in the overlapping of aluminum and silica elemental maps. The black areas in the images represent organic matter with a sponge-like appearance because the porosity is not fully resolved at the displayed magnification. Additionally, the large dolomite, calcite, and pyrite are aggregated into large multigrain nodules which contribute to the difference in geomechanical and geochemical behavior during stimulation compared to the ductile zones which will be shown to have a much finer grained clay matrix.

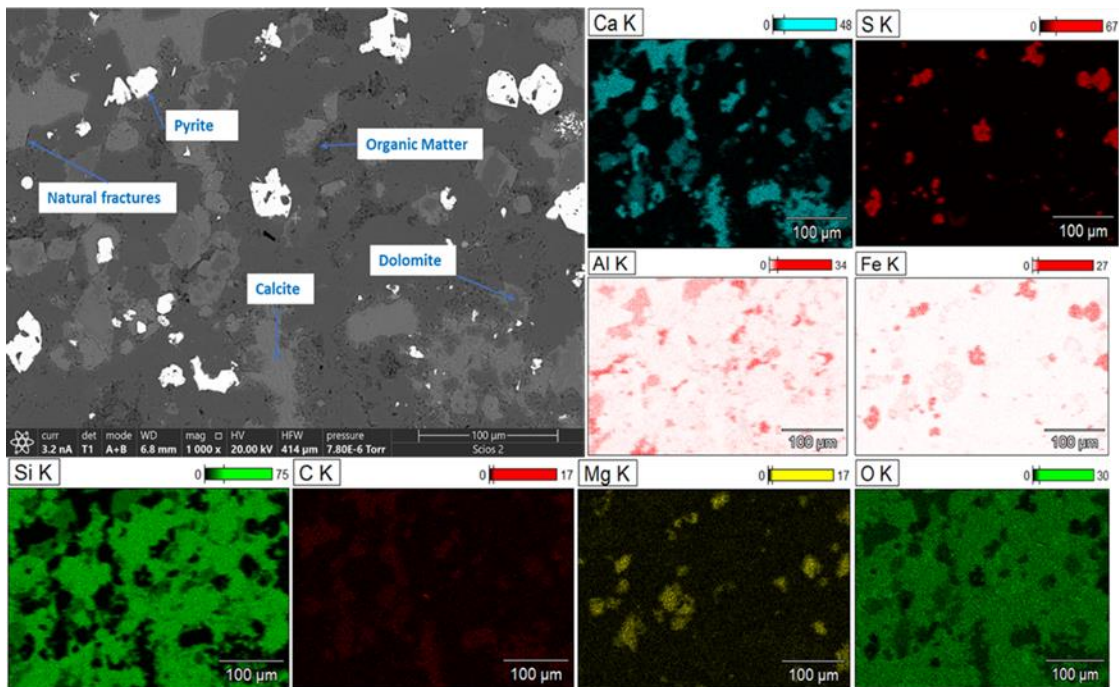


Figure 23 Reservoir 1 SEM backscatter electron (BSE) micrographs at 20 kV and 1000 X magnification

The Ductile 1 image in Figure 24 shows how clay and fine-grained silt dominate the sample, with the presence of fine-grained apatite depicted by bright white in the calcium maps and large diamond-shaped dolomite grains with calcified rims. Organic matter is present as small inclusions evenly dispersed throughout the sample. The micro fractures present are most likely an artifact of

sample preparation. Finally, the aluminum and silica maps indicate some clays form thin lamellar structures, seen in bottom right of the figure.

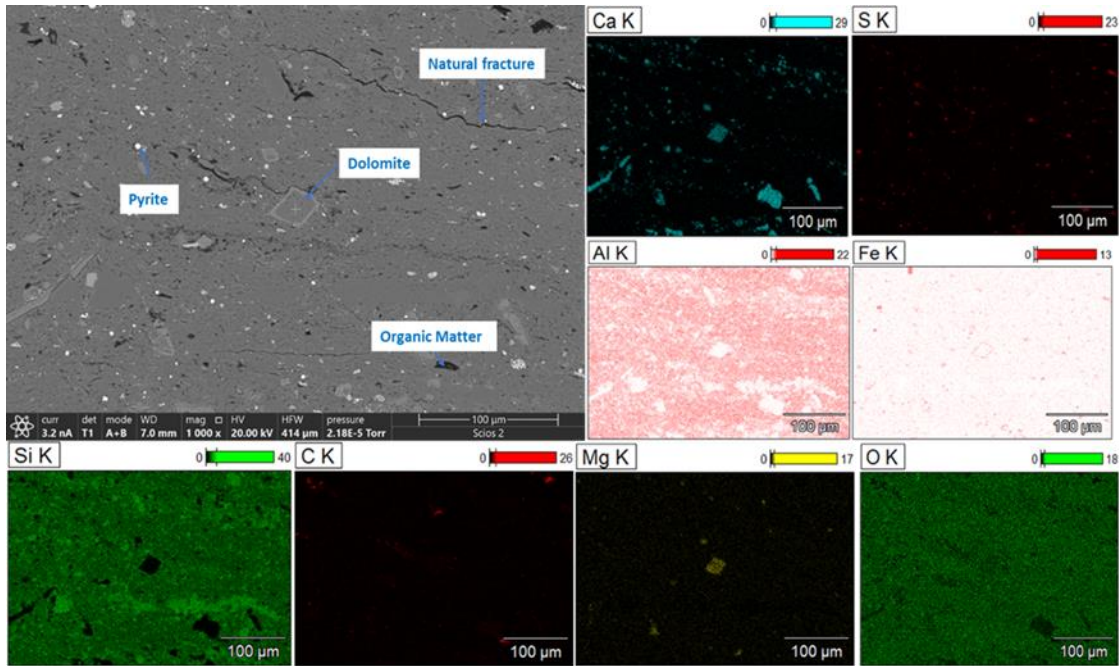


Figure 24 Ductile 1 SEM backscatter electron (BSE) micrograph at 20 kV and 1000 X magnification

Figure 25 demonstrates the more porous matrix of Reservoir 2, with calcite and dolomite embedded in the clay-rich matrix which appears to be swirled without clear layering. Organic matter is present both as coarse-grained isles and as very fine-grained matter interwoven in the clay matrix.

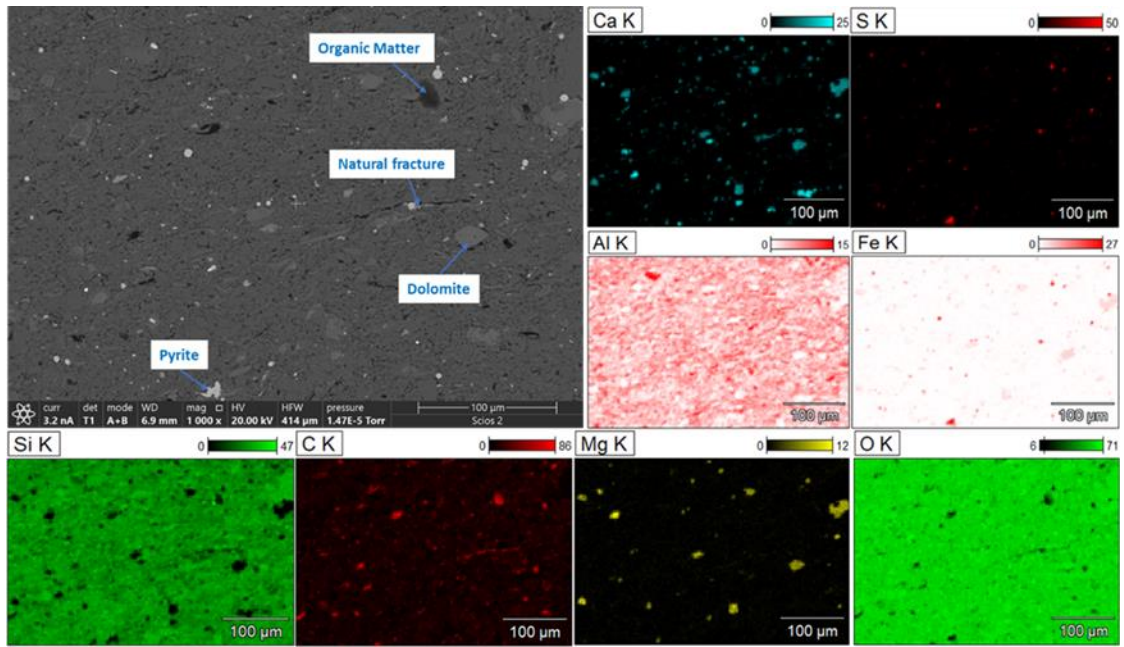


Figure 25 Reservoir 2 SEM backscatter electron (BSE) micrograph at 20 kV and 1000 X magnification

The second ductile zone, Figure 26, is similar to the first ductile zone and contains large individual dolomite grains within a fine-grained silt clay matrix. This sample also shows lens-like kerogen, indicating the presence of layering as seen when looking left to right in the figure.

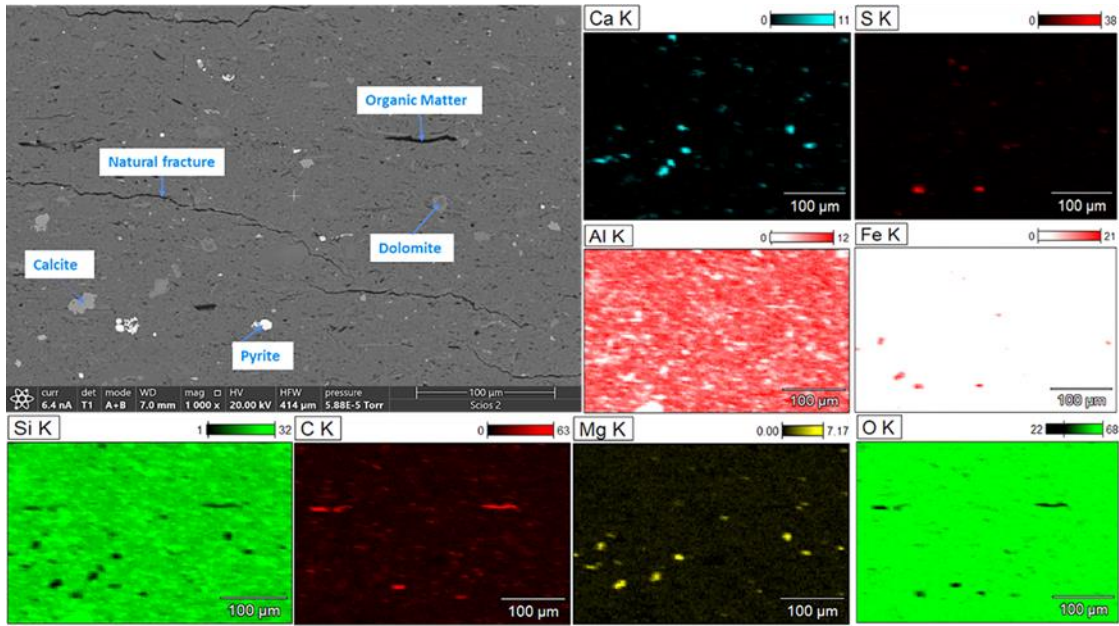


Figure 26 Ductile 2 SEM backscatter electron (BSE) micrograph at 20k V and 1000 X magnification

Finally, Figure 27 immediately stands out compared to all other zones. Reservoir 3 has a high kerogen content, indicating it is a favorable target for stimulation, with a texture which demonstrates a diagonal direction from the bottom left to the top right of the image. Pyrite does not adhere to the same directional preferences shown by the clays and kerogen. The calcium and magnesium maps depict a fine-grained dolomite present in the sample.

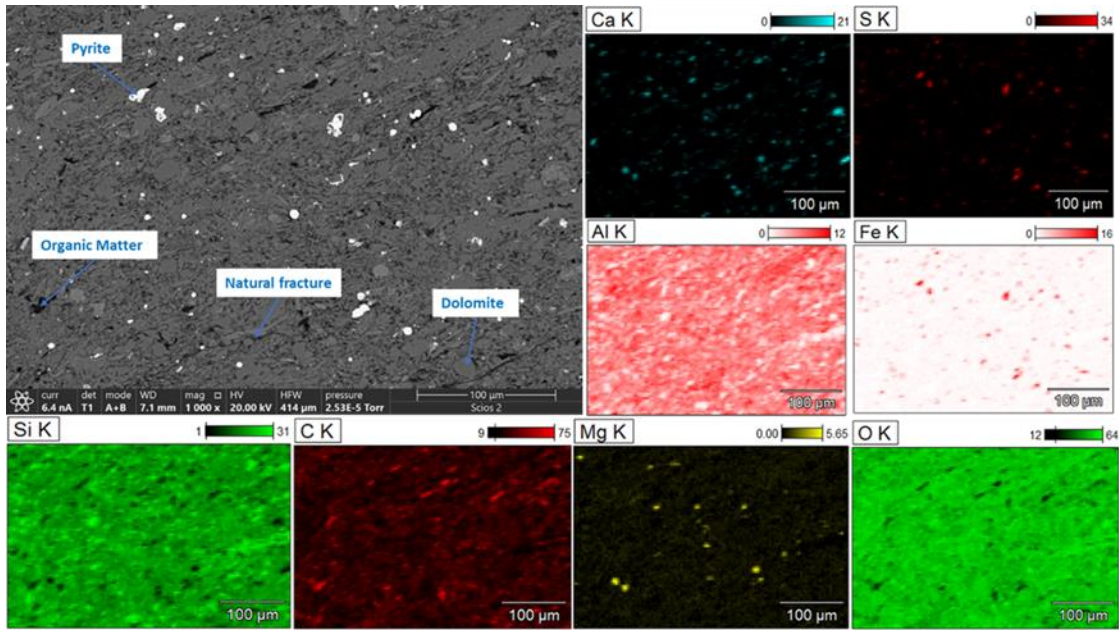


Figure 27 Reservoir 3 SEM backscatter electron (BSE) micrograph at 20kV and 1000X magnification

The mineralogy in all SEM micrographs agrees with XRD data. The nominally more ductile samples show higher clay content than the nominally more brittle zones, and the opposite trend is observed for carbonates, which would contribute to how the rock responds to mechanical load tests as well as prolonged creep tests. The variation in XRD bulk mineralogical composition between the zones identified as nominally ductile and nominally brittle is clearly linked to the visual variation seen in the SEM images, where the black organic material is contrasted by the darker gray aluminosilicates and somewhat lighter gray carbonate, bright gray quartz, and bright white pyrite and apatite. Each of these mineral groups has different mechanical and chemical stability which could potentially be taken out of equilibrium because of drilling, completions, and production (Awejori et al., 2022 and Xiong et al., 2022). Organic matter is not detectable in the XRD but the SEM micrographs and the EDS chemical elemental maps show the difference in the amount present as well as in the morphology of kerogen, which is present in ductile zones as fine grained and well dispersed, compared to the larger lens-like shapes of kerogen in reservoir zones

with a sponge-like texture indicating kerogen porosity. Note a similar correlation has been previously observed in other shale characterization efforts, as discussed by Loucks et al. (2012).

4.4 Rock Mechanical Properties

Previous rock mechanics testing under ambient conditions showed the nominally ductile zones have lower tensile strength, unconfined compressive strength, and fracture toughness compared to the nominally brittle reservoir zones (Benge et al., 2021a). This prior work also presents results of triaxial testing. However, for completeness, it is necessary to reiterate the triaxial testing procedure and results as they are relevant to the simulations presented later in this paper. Vertical core samples drilled perpendicular to bedding planes were subjected to single stage triaxial tests at 90°C and confining pressures ranging from 3.4-20.7 MPa (50-3000 psi), with the method based on ASTM 7012-14 (2014). A polymer sleeve surrounded the sample to allow application of radial confinement while preventing oil intrusion into the pore spaces of the rock. The sample and sleeve were placed in a Hoek-type triaxial cell (see Figure 28(A)). Confinement in the radial direction was applied to the sample by pressurizing hydraulic oil in the Hoek cell using an ISCO syringe pump. Axial loading was provided by an Instron load frame with Partner control software. Heating tape was wrapped around the cell and an internal thermocouple used to measure the specimen temperature, as shown in Figure 28(B). A BriskHeat SDX digital temperature controller was set to control temperature at 90°C.

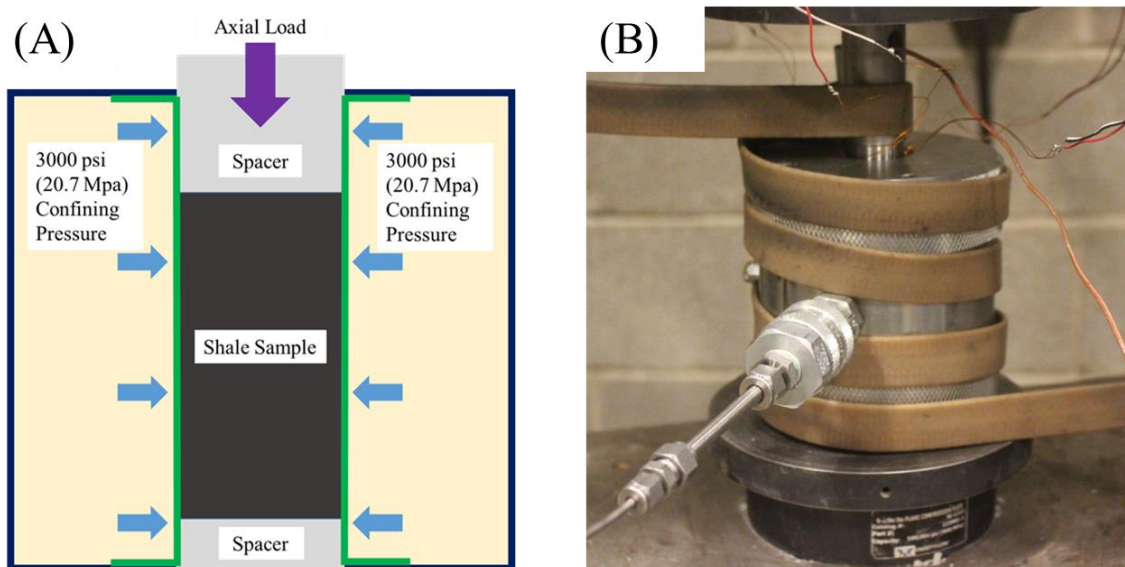


Figure 28 (A) Diagram of Hoek triaxial cell experimental setup and (B) cell set in load frame with heating tape wrapped around cell (external LVDTs not shown)

Throughout testing, the axial load, confining pressure, sample temperature, axial strain, and radial strain were monitored. The axial load was measured using the load cell in the Instron load frame while the confining pressure was controlled from the ISCO pump controller. As previously indicated, the BriskHeat controller maintained a constant temperature during the test, which was verified by measurement from a thermocouple placed between the jacket and the top loading platen, as close to the specimen as possible. Finally, axial and radial strains were measured using strain gauges adhered to the sample with an adhesive and recorded using a Vishay strain recorder.

To perform experiments, a confining radial pressure was applied to the jacketed sample along with an equivalent axial load in order to start the test under hydrostatic conditions. This initial hydrostatic confinement was held at 3.4MPa (500 psi) as the temperature was increased, except in low confinement triaxial tests when the targeted testing confinement value was 3.4 MPa, in which case the hydrostatic load was set to 1.72 MPa (250 psi). The tests conducted at 0.34 MPa

(50 psi), intended to simulate unconfined testing at temperature, started and remained at 0.34 MPa throughout the experiment. Once the sample reached 90°C, the axial load and confining pressure were increased in unison with the hydrostatic pressure required for the test. The sample remained at the target temperature and pressure for approximately two hours to ensure equilibrium of temperature and to enable drainage of any pore pressure generated during the confining and heating stages. Once at equilibrium, a single-stage ramp in the axial loading commenced, loading the sample via a constant axial displacement rate of 0.2 mm/min (0.008 in/min) until failure was detected through a decrease in the measured axial load. As soon as evidence of failure was detected the experiments were stopped and no attempt was made to capture post-peak behavior. This is because the specialized membranes used in this type of triaxial cell were very prone to failure during the post-peak time, especially at the temperatures used for these tests. Furthermore, even if the membrane did not fail, continuing to load into the post-peak range had the tendency to cause the specimen to become permanently lodged in the membrane so the sample and/or the membrane had to be destroyed in order to remove the sample for post-test documentation and storage.

Stress-strain curves for samples tested at 10.5 and 20.7 MPa (1500 and 3000 psi) confining pressure are presented in Figure 29. As can be seen by the axial strain lines, the ductile zones do not display a significantly different slope than the reservoir zones. Computing the slope from the 20.7 MPa (3000 psi) curves gives the Young's modulus, which is indicated in Figure 30 for each zone and is observed to have no systematic correlation with the distinction of "reservoir" or "ductile", per se, although Ductile 2 does have the smallest value. Similarly, all values of Poisson's ratio are in approximately the same range and display no clear difference between the nominally brittle and nominally ductile zones. This result for confined static Poisson's ratio stands in contrast to the dynamic value of the Poisson's ratio from the well log in Figure 20, which correlates strongly

with zones for which a higher value is taken as one indication of whether a zone is nominally “ductile”.

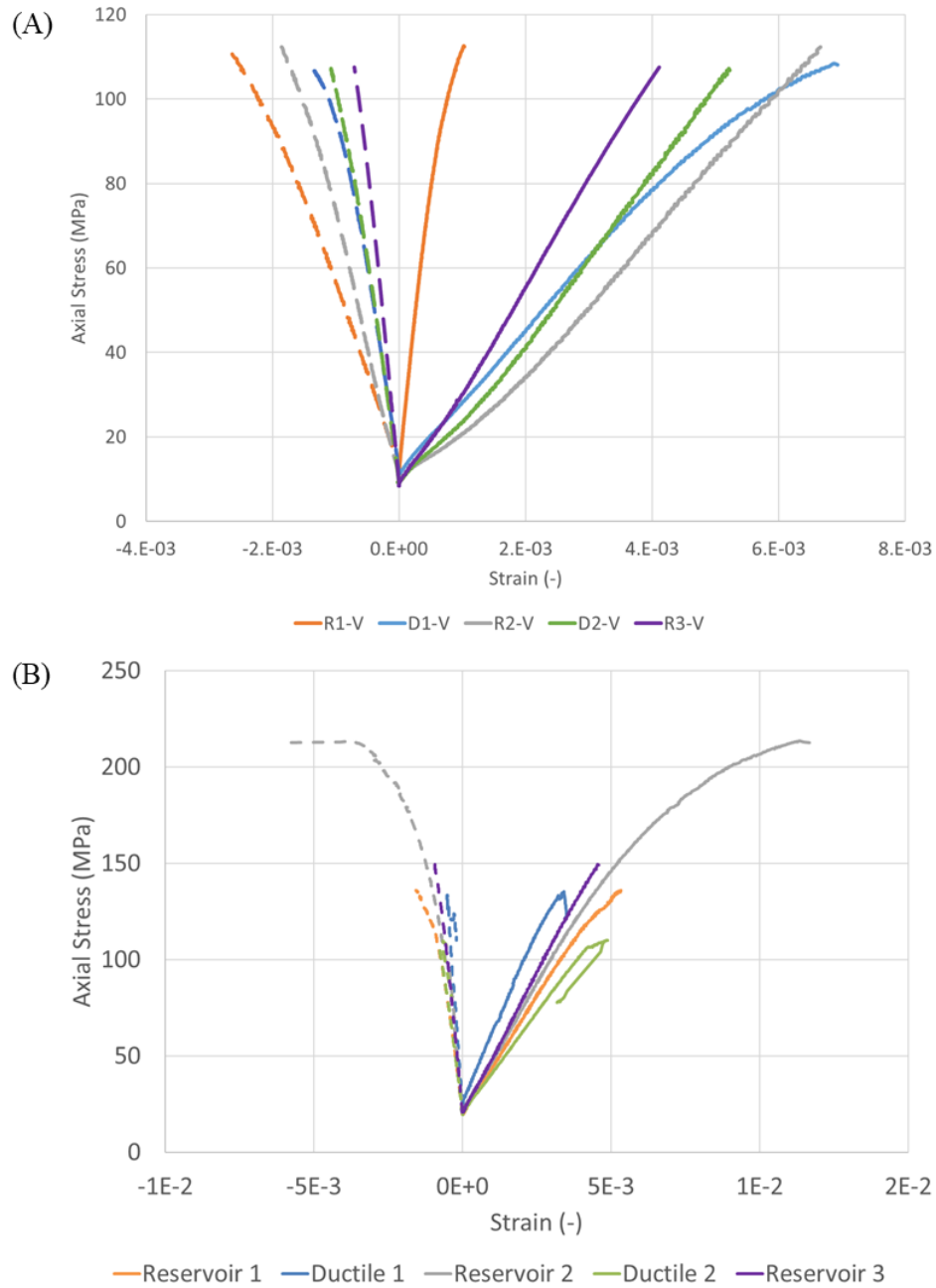


Figure 29 Stress vs axial strain (solid) and radial strain (dashed) for (A) 10.5 Mpa and (B) 20.7 MPa confined (1500 and 3000 psi) samples

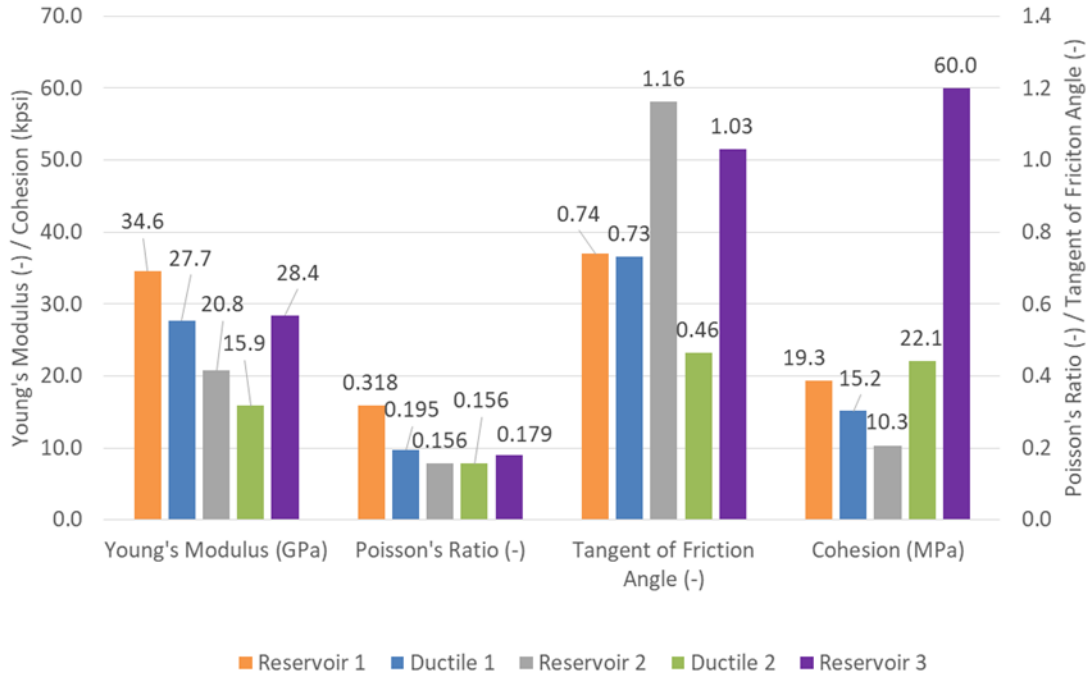


Figure 30: Average Young's modulus at 20.7 MPa (MPa), average Poisson's ratio at 20.7 MPa (-), tangent of friction angle (-), and Cohesion (kpsi) for each zone as calculated from triaxial results

The maximum axial stress at failure, taken at a variety of confining stresses, is presented for each zone in Figure 31. At nearly every confining level (except for the lowest value, intended to approximate an unconfined compressive strength at 90°C), the two ductile zones are the weakest. These results can also be used to calculate the cohesion c and friction angle ϕ using (Kovari et al., 1983)

$$\phi = \sin^{-1} \frac{m - 1}{m + 1} \quad c = b * \frac{1 - \sin \phi}{2 * \cos \phi} \quad (4.1)$$

Here m and b are the slope and y-intercept of a linear fit to each curve in Figure 31, represented as the dashed lines between points. The resulting values of cohesion and the curve of the friction angle are presented in Figure 30. To make the axis scale more convenient, we present the friction

coefficient the tangent of the friction angle. Here the most striking result is Ductile 2 clearly has the lowest value of the friction angle.

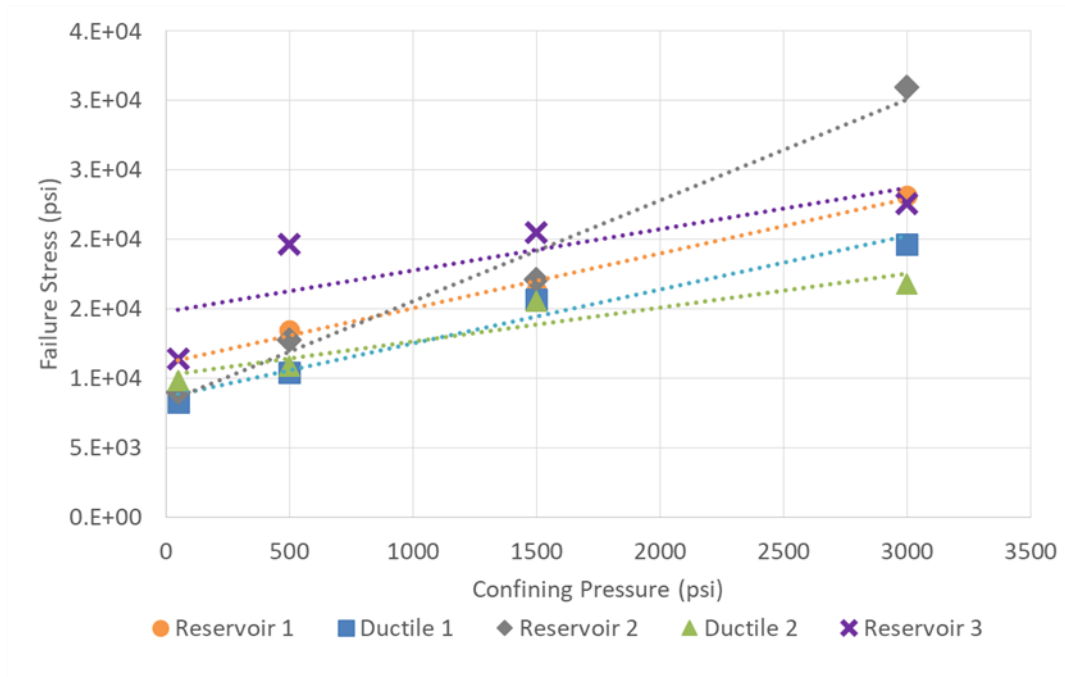


Figure 31 Axial stress for each zone at various confining pressures with linear fit shown to calculate friction angle and cohesion

4.5 Creep Compliance

Creep testing was carried out using the same sample preparation and cell as for the triaxial testing. The equipment to control the temperature and pressure as well as monitor the strain was the same with the addition of external LVDTs to measure axial displacement of the sample monitored through an external DATAQ system. These were added because calibration tests indicated the attached strain gauges undergo some creep, most likely in the adhesive, over long

periods of time at 90°C. Even with the use of high-temperature adhesives, it was not possible to remove this small amount of gauge creep. The LVDTs, in contrast, were very reliable over the long term. Additionally, the axial load frame was switched to an MTS 810 owing to superior long-term load control.

The applied confining pressure for all tests was 20.7 MPa (3000 psi) and the test temperature was 90°C. Inspired by the approach of Rassouli and Zoback (2018), a multiple stage, fixed load procedure was developed. As before, a lower confining pressure of 3.4 MPa (500 psi) was maintained while the sample reached the 90°C testing temperature. After reaching the test temperature the hydrostatic pressure was increased to 20.7 MPa. The hydrostatic pressure was maintained for at least 24 hours as the sample equalized, and the stabilized strain values were used as a reference point for the strain values for the remainder of the test (i.e., these are taken as the zero point in all the results reported subsequently in this thesis). After the hydrostatic stage, the axial force was increased to 30% of the expected axial stress at failure for the sample when tested at a confining pressure 20.7 MPa based on the results shown in Figure 31. This increased load was maintained for twenty minutes before the sample was returned to hydrostatic conditions for another twenty minutes to monitor recovery. A second axial load step to the same level was held for twelve hours, with an accompanying twelve-hour relaxation stage. After a second twelve-hour loading stage, a two-hour recovery stage was used before the final axial load, again to 30% of expected load for failure, was applied for 72 hours. For reference, the expected maximum stress and the applied axial stresses for each of the cases are provided in Table 2.

Table 2 Expected confined compressive strength at 20.7 MPa confinement, shown with applied axial stress during creep testing

Zone	Expected Confined Compressive Strength (MPa / psi)	Applied Axial Stress (MPa / psi)
Reservoir 1	134.45 / 19,500	40.33 / 5,850
Ductile 1	134.45 / 19,500	40.33 / 5,850
Reservoir 2	210.29 / 30,500	62.74 / 9,100
Ductile 2	109.63 / 15,900	35.16 / 5,100
Reservoir 3	115.13 / 22,500	46.54 / 6,750

The strain evolution for each sample is presented in Figure 32. Note, however, each sample had a different applied axial load during the creep stages, as this was chosen as 30% of the failure stress for each sample. So, to facilitate comparison among zones, Figure 32 presents the evolution of the compliance, taken as the evolving strain, ε , divided by the axial deviatoric stress applied during the creep stages, σ .

$$J = \frac{\varepsilon}{\sigma} \quad (4.2)$$

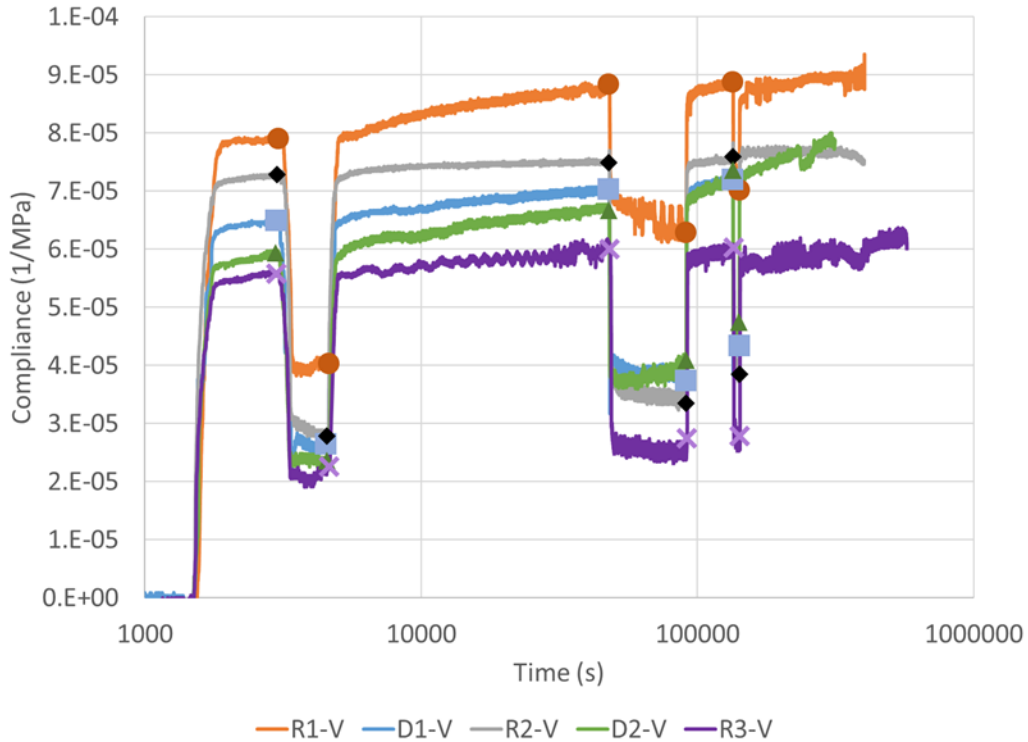


Figure 32 Evolution of compliance (total axial strain divided by deviatoric stress) from creep tests

Recall also Figure 32 takes the reference point for all strain values at the end of the hydrostatic phase, thus giving the graph for each sample a starting point of zero strain prior to application of the first deviatoric axial load. It is instructive to look in some detail at the behavior of each of the zones in Figure 32.

4.5.1 Reservoir 1

This zone has the largest total compliance at all points in the evolution of this quantity. After the initial 20-minute loading (seen at the 24-hour mark), about 50% of the strain was immediately recovered, indicating about 50% of the strain associated with the immediate deformation was plastic and 50% was elastic. On subsequent loading, the compliance returns to

the same level and then undergoes substantial creep. Of this, about 40% is immediately recovered (indicating some additional immediate plastic deformation on the second loading) and in total around 50% is finally recovered at the end of the extended recovery period (ending at around 48 hours). In fact, the time-dependent compliance recovery ($\sim 0.5 \times 10^{-5}$ 1/MPa) comprises around 50% of the total creep compliance ($\sim 1.0 \times 10^{-5}$ 1/MPa), indicating a 50/50 split between viscoplastic and viscoelastic creep. In the final stage of loading, the compliance returns to a level suggesting there is no additional immediate plasticity, and the creep appears to be consistent with mostly viscoelastic deformation, with only a slight increase in the compliance level at the commencement of the final unloading. This indicates a small amount of viscoplastic deformation during the final creep stage.

4.5.2 Reservoir 2

At the outset one notices the compliance is the second largest, second only to Reservoir 1. However, the initial load/unload steps indicate over 50% is immediate plastic strain. Upon reloading and subjecting the sample to creep conditions, the compliance rapidly stabilizes and undergoes almost no change for the remainder of the stage. Upon unloading there is a small recovery, similar in magnitude to the creep which was previously sustained, indicating a viscoelastic mechanism. The final creep stage produces exactly the same compliance as the first, again with almost no increase over time. Hence, Reservoir 2 shows the most stable behavior with time and is the least susceptible to creep deformation.

4.5.3 Reservoir 3

Reservoir 3 exhibits the least compliance overall and a 70/30 split between elastic and plastic immediate deformation. Similar to Reservoir 2, the creep stages generate only a small amount of time-dependent deformation, essentially all of which is recovered indicating a viscoelastic mechanism. Although the total compliance is less than Reservoir 2, there is slightly more creep compliance on the longer time frames (as shown in more detail in Section 4.5.5).

4.5.4 Ductile 1 and Ductile 2

The behavior of these two zones is similar, with similar values of compliance at all stages of loading, despite the first ductile zone being approximately 30.48 m (100 feet) above the second ductile zone. In both cases, the initial load/unload suggests a ~60/40 split between elastic and plastic immediate deformation. Both samples undergo significant creep with almost no recovery during the extended recovery stage. Hence, the creep is likely accommodated almost entirely as viscoplastic creep, with a negligible viscoelastic component.

4.5.5 Creep Compliance Calculation

In order to parameterize the creep compliance in a manner which can be implemented in numerical models, the immediate and time-dependent (creep) parts of the compliance are separated. The creep compliance for each zone is shown in Figure 33(A). Each zone is then fit with a power-law creep model,

$$J = \frac{\varepsilon}{\sigma} = J_{immed} + J_{cr} \quad J = C + kt^n \quad (4.3)$$

where C is the calculated compliance for the immediate part of the loading, t is the time in seconds since the differential load was applied, k is the coefficient in the creep law, and n is the time exponent in the creep law. Note when using a classical compliance coefficient typically denoted as B , the relationship to k is $k = B/\sigma$. Results of this fitting are shown in Table 3.

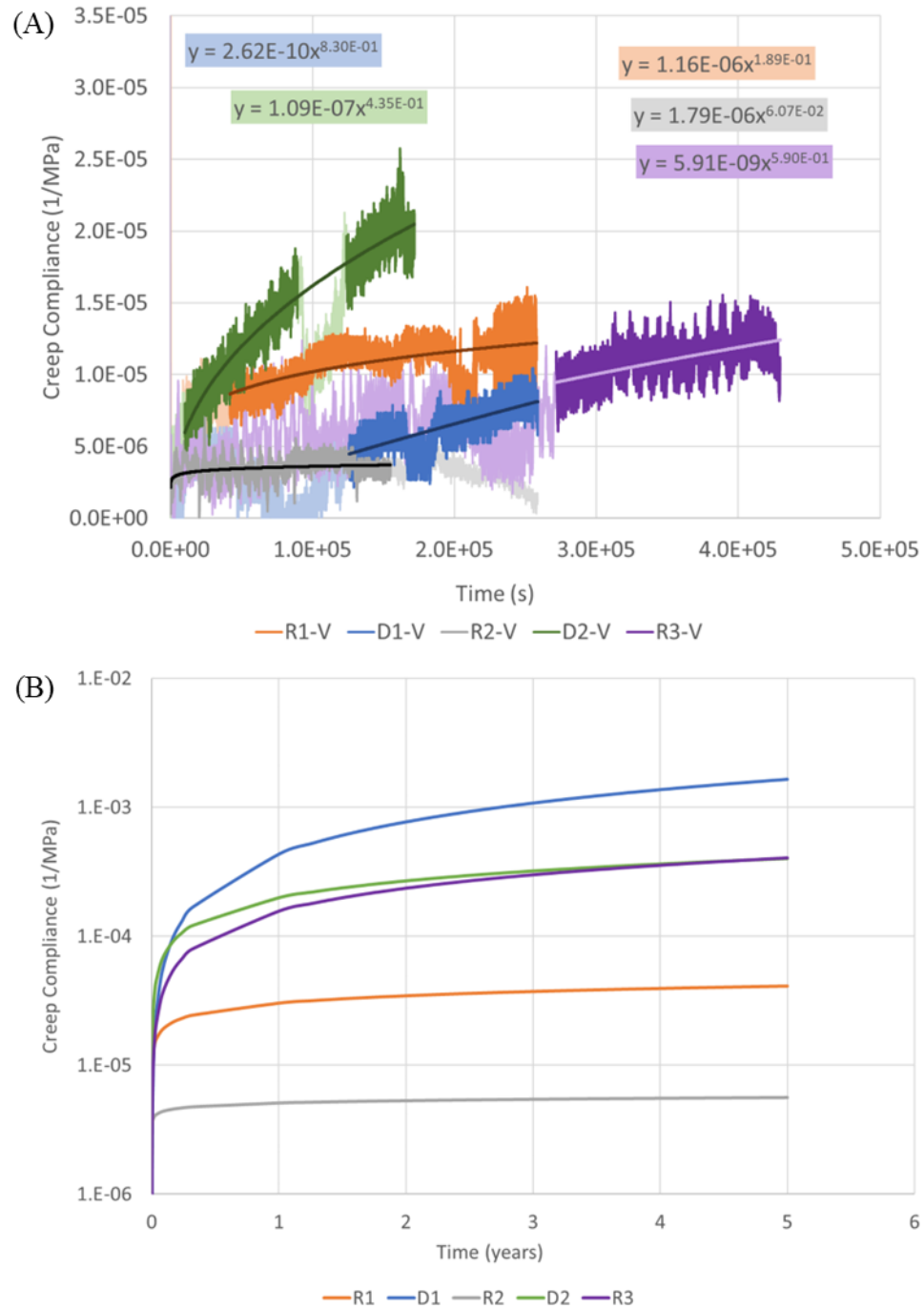


Figure 33 (A) Creep compliance (axial creep strain divided by deviatoric stress) as a function of time, with power law fitted equations and (B) power law fit equations extended to five years

Table 3 Power-Law creep model parameters, valid for stresses in MPa and time in seconds

Zone	k (1/MPa)	n (-)
Reservoir 1	1.17×10^{-6}	0.188
Ductile 1	2.62×10^{-10}	0.830
Reservoir 2	1.79×10^{-6}	0.061
Ductile 2	1.09×10^{-7}	0.435
Reservoir 3	5.91×10^{-9}	0.590

These results show Ductile 2 (D2) is the zone most susceptible to creep in the short term (Figure 33). However, if the fitted creep law is projected out over a time frame of years, as shown in Figure 33(B), Ductile 1 emerges as the most prone to creep after approximately six months. In contrast, Reservoir 2 (R2) is the least susceptible to creep. As one might hypothesize for more clay-rich zones, the nominally ductile zones appear to have higher susceptibility to creep than the nominally brittle reservoir zones. These five-year extrapolations are based on laboratory testing, which by necessity is limited to a reasonable time frame, which in this case was 72 hours as this was the point when the axial strain appeared to reach a constant value. As with all other long-term creep estimations, a test spanning more than a year is unreasonable in terms of laboratory resources, and assumptions must be made for the creep of any material over long periods of time. However, these values were verified against the creep measured in the laboratory over the 72-hour loading stage, and the good agreement with measured strain values provides a fair confidence for extrapolating the strain beyond the time frame used in the laboratory.

4.6 Simulation of Proppant Embedment

Numerical modeling was performed to investigate the potential impact of shale creep on long-term proppant embedment and fracture closure. This modeling is part of ongoing work related to coupled multiphase fluid flow and geomechanical modeling of hydrocarbon production from a network of proppant-filled fractures. The necessary model developments and applications are based on the linking of the TOUGH2 multiphase fluid flow simulator with the FLAC3D geomechanical simulator (Pruess et al., 2012, Itasca, 2011, Rutqvist, 2011, and Rutqvist 2017). Focus is placed on the modeling of proppant embedment and fracture closure as a result of creep deformation over a five-year time period. The simulations include the impact of elastic, plastic, and creep strain on proppant embedment and fracture closure. A Mohr-Coulomb model is applied to calculate plasticity and any plastic embedment which would occur as a result of the load taken by a proppant between closing fracture surfaces. Such a Mohr-Coulomb plasticity model has recently been applied to accurately model indentation experiments on shale (Voltolini et al., 2021, Katende et al., 2021b) and is therefore expected to be adequate for modeling elasto-plastic proppant embedment. For modeling creep embedment, an empirical power-law model was selected (Sone and Zoback, 2014a, Rassouli, and Zoback, 2018). In this model, creep strain, ε_{creep} is calculated according to the expression:

$$\varepsilon_{creep} = k\sigma_{vm}t^n \quad (4.4)$$

where σ_{vm} is von-Mises stress, t is time, and k and n are material properties. This creep model was selected because it has been successfully applied in previous work to analyze creep experiments

on various shales (Sone and Zoback, 2014a, Rassouli and Zoback, 2018, and Li and Ghassemi, 2012). As shown previously, the two model parameters k and n can be conveniently evaluated from triaxial creep tests using a graph of creep compliance versus time.

In this modeling, two extremes of formation properties are considered, namely Reservoir 2 representing nominally brittle reservoir properties and Ductile 1 representing a nominally ductile formation with high clay content. The power-law description of the creep deformation (Table 3) was used as the input for the creep properties of the formation during modeling, applying the elasto-plastic and creep properties as determined from core-scale triaxial compression and creep tests as described previously. The modeling is performed using an axisymmetric model, for an ideal case of spherical proppants of a certain diameter uniformly distributed in a monolayer (Figure 34). The uniform proppant spacing, or center-to-center distance, between individual proppant particles are simulated by changing the radius of the axisymmetric model (Figure 34(B)). The rollers in Figure 34(B) illustrate boundaries where displacement is allowed parallel to the boundary surface while no displacement is allowed normal to the boundary. A stress corresponding to the fracture closure stress at depth is applied to the model in a direction normal to the fracture, which in Figure 34(B) is from the bottom of the model. For the Caney shale it is reasonable to consider a fracture closure stress of 72 MPa (10,000 Psi) (after Vulgamore et al., 2021). Proppant diameters of 0.15 mm (150 μ m or 0.006 inches) and 0.3 mm (300 μ m or 0.012 inches) are considered to represent commonly used proppant mesh sizes for production from shale gas reservoirs. The 0.15 mm proppant diameter corresponds to a 100-mesh size proppant, whereas the 0.3 mm corresponds to an approximate average diameter for 40/70 mesh size proppant. The load taken by one proppant from the fracture closure stress will depend on the spacing between neighboring proppants and will also depend on the reservoir fluid pressure. Here we consider an extreme case

of complete pressure depletion during fluid production, meaning no stress is taken by fluid pressure but instead the stress normal to the fracture is funneled through the proppants.

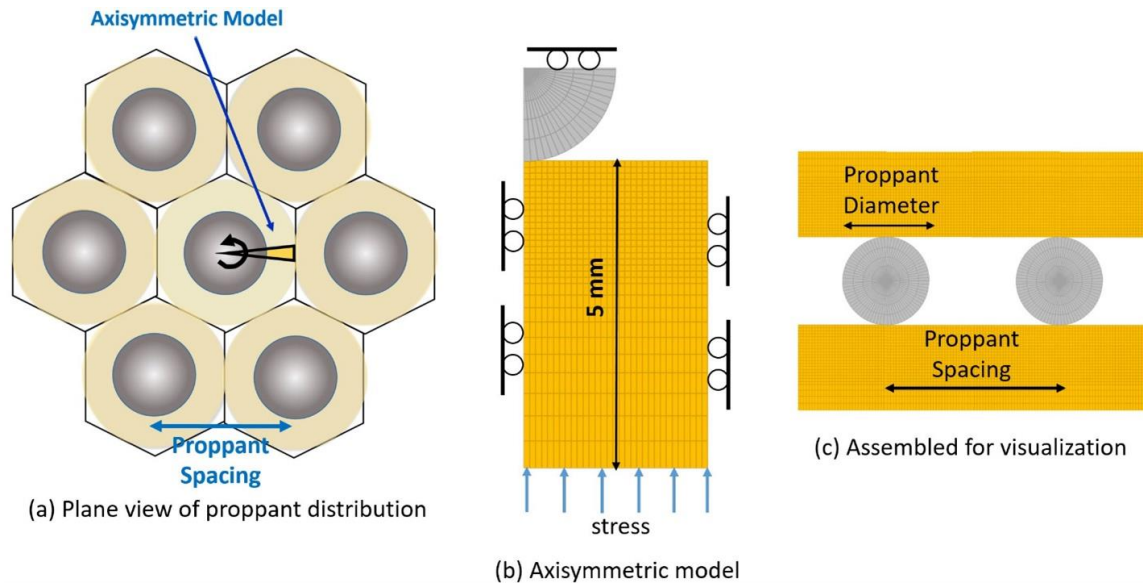


Figure 34 Axisymmetric model geometry with boundary conditions and mesh discretization applied for modeling proppant embedment and fracture closure

Figure 35 and Figure 36 present modeling results of embedment for the idealized case of 0.15 mm (150 μm) diameter proppant located at a center-to-center distance of 0.3 mm in a monolayer of proppant. For the fracture closure stress of 72 MPa, the average load on a proppant agent is estimated at 5.4 N for an extreme case of complete pressure depletion due to fluid production. Figure 35 shows the evolution of proppant embedment, including the initial elasto-plastic embedment followed by time-dependent creep embedment during five years of constant proppant load. The model simulations show the amount of elasto-plastic creep embedment is much larger for Ductile 1 properties. The elasto-plastic embedment corresponds to a fracture closure of about 0.04 mm (40 μm or 0.0016 inches) for Ductile 1 properties compared

to only 0.025 mm (25 μm or 0.001 inches) for Reservoir 2 properties. Creep embedment is different for the nominally ductile and nominally brittle formation properties. The creep closure amounts to only about 0.0002 mm (0.2 μm or 7.8×10^{-6} inches) for Reservoir 2, but as much as 0.064 mm (64 μm or 0.0025 inches) for Ductile 1. Thus, it may be concluded creep embedment is negligible in the case of the reservoir zone, whereas creep is significant in the case of the ductile zone. This confirms a correlation between the clay content of a formation and its susceptibility for creep fracture closure. For the particular case studied, assuming 0.15 mm diameter proppant spaced 0.3 mm apart, the fracture would still be held open after five years even for the high-clay-content formation. The aperture at the mid distance between neighboring proppants after five years of creep is calculated as 0.125 mm (0.005 inches) for Reservoir 2 properties (Fig. 17(A)), and 0.05 mm for Ductile 1 properties (Fig. 17(B)). If flow through the fracture is proportional to the cube of the aperture (i.e., a classical cubic law from Poiseuille flow), then the reduction in conductivity of Ductile 1 would be around 16 times greater than Reservoir 2.

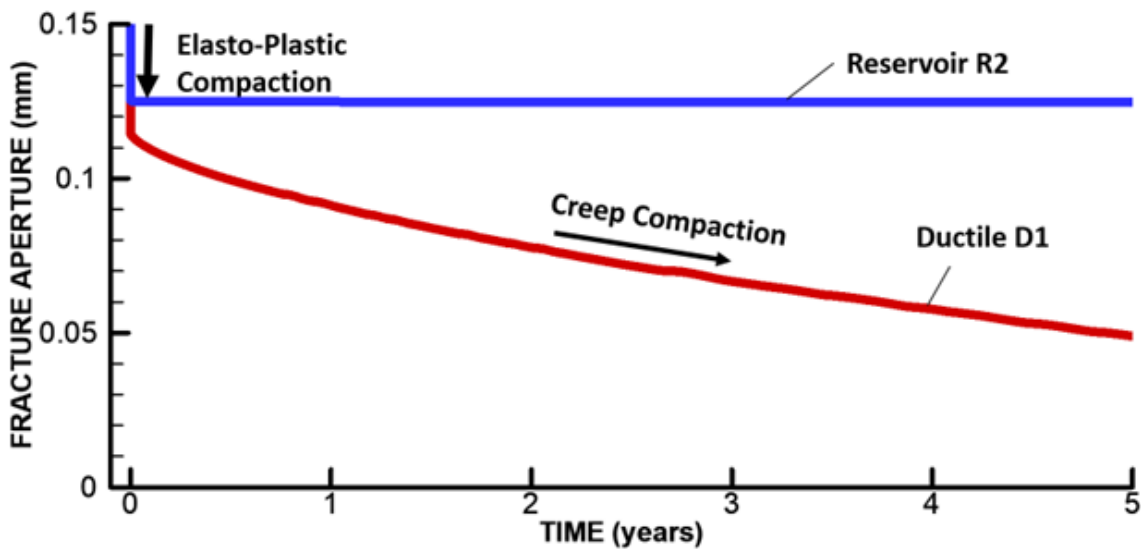


Figure 35 Simulation results of elasto-plastic and creep compaction with calculated fracture aperture evolution as a result of proppant embedment for Reservoir 2 and Ductile 1 properties

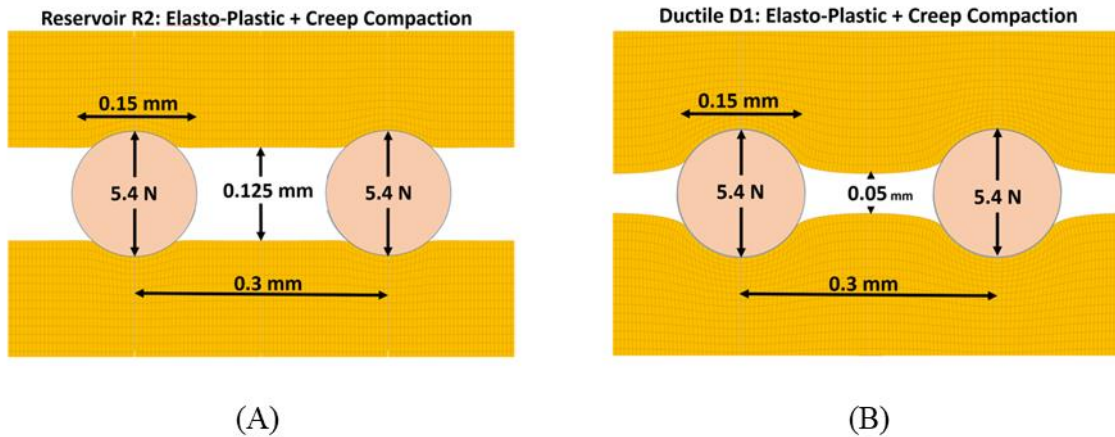


Figure 36 Simulation results of proppant embedment after elasto-plastic and five years of creep compaction for (A) Reservoir 2 properties and (B) Ductile 1 properties

Figure 37 and Figure 38 present the results of sensitivity studies considering different proppant distances of 0.15, 0.30, and 0.40 mm apart, and two different proppant diameters of 0.15 and 0.30 mm. Recall the 0.15- and 0.30-mm proppant diameters correspond respectively to 100-mesh size and the average of 40/70 mesh size proppants. The proppant embedment depends strongly on the proppant spacing because the load taken by each proppant will increase with greater spacing. For example, if the proppant spacing increases just from 0.30 mm to 0.40 mm, the proppant load would almost double from 5.4 to 9.6 N (1.2 to 2.16 lbf) and the fracture would close completely after 2.4 years (Figure 37(A)). On the other hand, if proppants are placed in perfect arrangement next to each other (i.e., distance 0.15 mm for 0.15 mm diameter proppants), the force taken by a proppant would be 1.4 N (0.31 lbf) and the proppant embedment would be quite limited. However, the cross-sectional area open to flow through the propped fracture would be quite small, resulting in a relatively low fracture permeability. In the case of larger diameter (0.3 mm) proppants, the fracture aperture would not only be larger, but would also stay open longer for a

given proppant distance. Considering a case for proppant spacing twice the proppant diameters, the relative permeability reduction will be similar but the absolute permeability would be higher in the case of the larger diameter proppants.

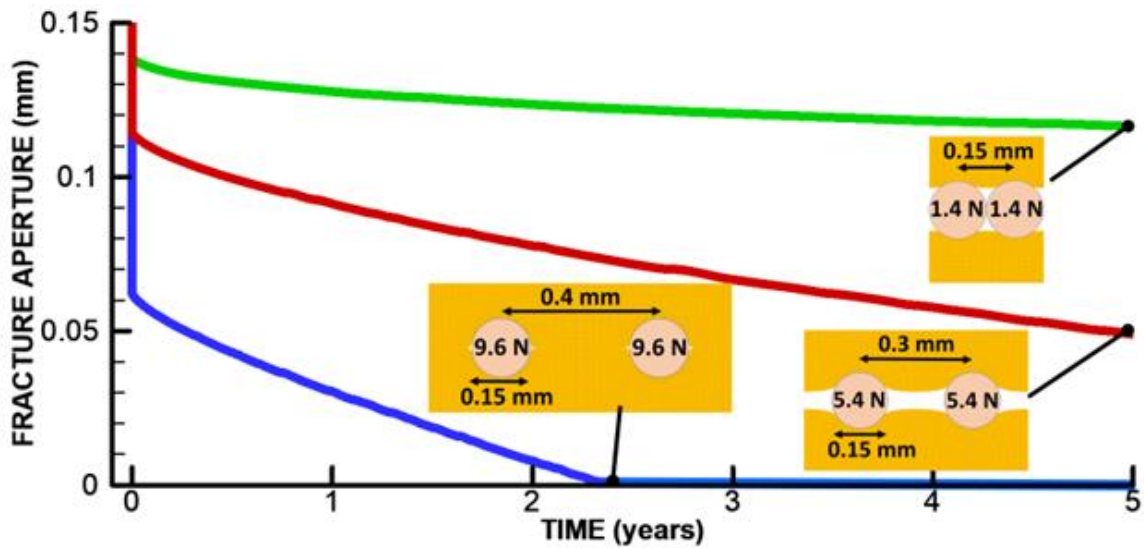


Figure 37 Fracture opening width for Ductile 1 formation and 0.15 mm diameter proppant, plotted as a function of time with diagrams of final fracture geometry after 5 years of simulated time

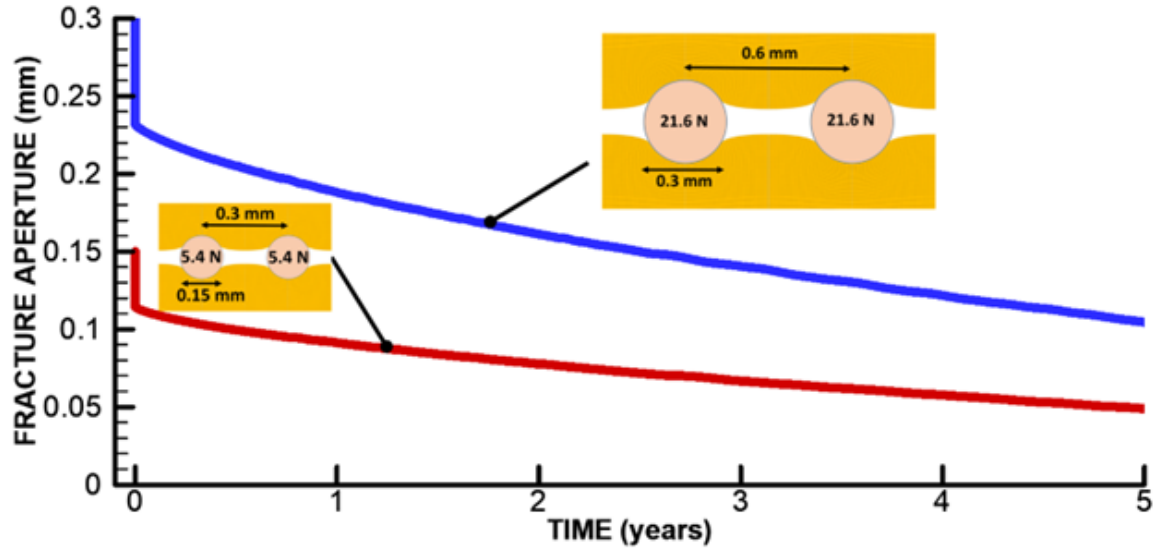


Figure 38 Simulation results of two different proppant diameters (0.15 and 0.30 mm) and with proppant spacing twice the proppant diameter for the case of Ductile 1 properties

4.7 Discussion

An initial discussion point is the applicability of the terms “ductile” and “brittle” when describing the Caney shale samples. As previously demonstrated (Benge et al., 2021a), these terms are potentially misleading when applied using the traditional geomechanical definitions of ductile and brittle. However, as has been demonstrated here, the ductile zones are mechanically weaker and more prone to long-term deformation in the form of creep. Therefore while the definition may not be strictly applicable, there is a usefulness in distinguishing the more creep-prone zones in the formation.

The second point worth discussing is the correlation between mechanical behavior of Caney shale samples from the five identified zones with their bulk composition as well as internal microstructure of each sample, primarily the difference between nominally ductile vs nominally

brittle regions. It appears the clay rich zones are the most important mineralogical feature of Ductile 1 and 2 regions, while Reservoir 1, 2 and 3 are distinguished by high carbonate content (dolomite and calcite). The quartz content is similar in all zones. On the other hand, organic content is present in all zones, but Ductile 1 and 2 have finer, well-dispersed kerogen compared to larger, high-porosity kerogen lenses present in the reservoir zones. All of these observations support the mechanical testing data, as elasticity and creep are more associated with clays and fine-grained kerogen, while carbonates and large kerogen lenses would contribute to preferred fracturing initiation and propagation. As demonstrated using the formation model, the nominally ductile zones tend to creep more than the nominally more brittle reservoir zones, which would cause fractures to slowly close due to creep. In terms of proppant embedment, embedment will occur more readily in clay-rich zones. While carbonate dissolution would contribute to weakening and fracture closure in reservoir zones, this would be a slow and chemically driven process, rather than only by closing fracture stress. This study did not investigate the sample orientation in relation to the bedding of the rock, although bedding plane orientation would also play a role in how rock responds to the proppant embedment and ultimate fracture permeability in terms of production versus time. This study focuses only on the influence of creep and creep deformation on the long-term production of the well, and factors such as the permeability of the formation and the amount of hydrocarbons present in the formation, while extremely important to determining overall production of a reservoir, are not the focus of this study. Additionally, this study does not examine the natural or unpropped fractures present in a formation, though it is likely the tendency of the formation to creep would have a significant impact on the productivity of these fractures.

Overall, the modeling shows creep embedment is negligible in the case of the most brittle reservoir zone, whereas creep is significant in the case of the ductile zone. This confirms a

correlation between the clay content of a formation and its susceptibility for creep fracture closure. It also shows for ductile zones it is important to be able to place the proppants in a dense packing to avoid complete fracture closure. The simulated ductile zone demonstrated a tendency to creep closed much faster and to a greater extent than the nominally brittle reservoir zone, and therefore it can be concluded the nominally ductile zones would experience greater fracture closure and a corresponding greater drop in production over time compared to the nominally brittle zones. This difference in production may indicate a need to later re-stimulate any ductile zones which were fractured, and it may be possible to extract a greater volume of hydrocarbons overall from the nominally more brittle zones.

As the goal of this model simulation was to investigate the impact of shale creep on proppant embedment and fracture closure, other effects such as variable proppant shapes, proppant creep and crushing, and multilayer proppant placement have not been considered. For a thicker multilayer proppant pack (e.g., several mm thick), the fracture flow transmissivity will depend on the thickness and permeability of the proppant pack (e.g., unconsolidated sand permeability). A fracture closure on the order of 0.1 – 0.2 mm (0.004 – 0.008 inches) as calculated in this study would have a negligible impact on the fracture transmissivity compared a several millimeter thick proppant pack, where the particles of more central layers of proppant would support the particles closer to the formation, preventing full closure of the fracture. The multilayer proppant pack is more likely to occur near the well, while proppants emplaced in monolayers at variable proppant spacing are more likely to occur deeper into the stimulation zone away from the wellbore.

As a cautionary note, this paper focuses only on fracture closure due to proppant embedment (which may be both near-wellbore and far field), without accounting for factors such as the impact of fracturing fluids on the mechanical properties of the formation. While additional

impacts are possible, the most obvious impact could be the swelling of clay components in the presence of water. This swelling could significantly increase the amount of proppant embedment. A second example of the impact of creep is provided by Sone and Zoback (2014b), noting a large difference between maximum and minimum stresses in brittle formations and a nearly isotropic stress state in more ductile formations. This closure of the gap between stresses may be related to the increased creep tendency in ductile formations, and the increase in stresses may cause additional proppant embedment.

In addition to the closure of fractures in the formation, the change in the stress profile as predicted by Sone and Zoback (2014b) is different than the traditional profile as calculated by Eaton's method (Eaton, 1969). The second method relies on the overburden pressure, depth of the formation, and Poisson's ratio, while Zoback's method leans heavily on the properties as determined from laboratory creep testing. While outside the scope of this chapter, an examination of the measured in-situ stresses would indicate which of these methods provides an improved estimation of in-situ stresses. Changes in in-situ stresses between layers would cause an issue when stimulating the formation, as fractures grow preferentially in low-stress formations. Again, while the specifics of designing a stimulation plan are outside the scope of this thesis, the additional control mechanisms required to ensure fracture growth in targeted areas should be considered when designing a well for hydrocarbon extraction.

Sone and Zoback (2014b) also discuss assigning brittleness grades which vary with changes in in-situ stresses and mineral composition. Another example from Kainer et al. (2017) examining rock fabric factors noted a positive trend between Young's modulus and Brinell hardness with fracture conductivity, but recognized other factors appear to contribute to conductivity. Zhang et al. (2014) examined the relationships of brittleness and ductility to fracture

conductivity and concluded the conductivity of an unpropped fracture is directly related to brittleness while the conductivity of a propped fracture shows a weak correlation to the elastic properties of the shale samples. Similarly, this study did not find a clear correlation between the Young's modulus and the power-law creep properties as determined from laboratory testing. Thompson et al. (2010) introduced the concept of production hindrance in the ductile Haynesville formation and linked the deformation of formations under "highest effective stress" and proppant embedment in the near wellbore as an "irreversible conductivity choke", suggesting the gradual application of stress in controlled drawdowns could decrease the decline in production by 50% or more.

One final reminder is required noting the highly variable nature of rocks. This study, as with any study based on experiments which require a long time to perform, is necessarily limited to testing of a few samples, and simulations were performed to supplement the limited number of laboratory data points. This is the classical and ubiquitous issue of representative properties in rock mechanics, and it is to be respected here owing to the potential for wide variances existing in the rock fabric of the formations of interest. While a more detailed description of the properties of the Caney shale will be provided using an increased data set from planned future testing, the number of samples tested in this, and any practically achievable testing plan, is always smaller than what would be needed to fully characterize variability of actual rock formations, especially in complicated sedimentary basins.

4.8 Conclusions

As an emerging hydrocarbon play, the Caney shale was previously thought to be a relatively ductile shale formation, with some zones identified on well logs as more ductile than others. The classification based on the well log is successful in identifying the nominally brittle and nominally ductile formations as correlated to mineralogy. Ductile zones are correctly identified as zones with higher clay content and smaller quartz-feldspar content than the identified nominally brittle reservoir zones. However, past work has shown “brittle” and “ductile” are not strictly applicable to describe the differences in mechanical behavior in the identified zones.

Nevertheless, the well log and mineralogy are shown in this study to be capable of identifying zones which are weaker and more prone to creep deformation over time. Indeed, results show the nominally ductile zones consistently fail at lower stresses compared to the nominally brittle reservoir zones. Additionally, the lowest value of the Young’s modulus and the lowest friction angle are associated with the zone which is also the most prone to creep deformation. The two nominally ductile zones are substantially more prone to creep with 5-year creep compliance values around 100 times larger than the least creep-prone of the nominal reservoir zones. However, when using traditional triaxial testing methods there was not a clear correlation between triaxial properties such as Young’s modulus and Poisson’s ratio and the power-law used to describe creep behavior, only the qualitative one described. This could in part be due to the methods used to obtain samples, as by necessity the core was exposed to ambient conditions and stresses induced by tectonic influences such as the pressure in the formation could have relaxed and altered the properties of the samples.

Hence, the experiments show how, from the perspective of creep deformation, there is a clear difference between the ductile and reservoir zones. This higher susceptibility of ductile zones

to creep deformation can be expected to translate into a higher tendency for proppant embedment which, in turn, lowers the hydraulic aperture of propped hydraulic fractures and can lead to production decline. Numerical simulations show the long-term proppant embedment associated fracture closure and fracture permeability is significantly influenced by the lower strength and higher creep compliance of the nominally ductile zones compared to the nominally brittle zones. Specifically, the reservoir zones undergo negligible creep while ductile zones can be expected to undergo creep-driven proppant embedment leading to loss of fracture aperture ranging up to 100% loss, depending upon the spatial density of the proppant distribution. Hence, this research shows the identification of nominal “ductile” zones from well logs, while a misnomer, can be useful in finding clay-rich, creep-prone zones which will be the most prone to proppant embedment and hence vulnerable to greater production decline over time. This insight into the behavior of the formation allows for optimization of the stimulation plan, targeting zones which will not experience a significant decline in production due to fracture closure and potentially performing additional treatments as needed to improve the overall hydrocarbon extraction.

While the experiments and simulations are specific to the Caney shale, there are several principles which could be applicable to other shale reservoirs. Most notably, despite the misnomer, identifying nominally “ductile” zones based on well logs is beneficial to provide an indication of layers which will be more susceptible to proppant embedment and can be expected to experience more significant production decline compared to nominally brittle “reservoir” zones. With this said, the utility of such an approach has been shown for comparison among layers within a given formation, and it is not clear whether one can meaningfully use such correlations to speculate about the economic prospects of a new formation based on comparison to a different play. Nonetheless, the relationship among log properties, mineralogy, microstructure, strength, and creep

susceptibility illustrates an integrated approach to shale evaluation which, with the help of geomechanical simulations, gives a comprehensive view of physical and mechanical properties of the shales and the potential for these properties to meaningfully impact production for various zones within a target formation.

4.9 Creep Testing of Additional Orientations

This section was not included in the original publication as creep testing of the horizontal and 45° samples were completed at a later date. Additional testing is discussed here along with analysis of both the new results and their relationship to testing presented as part of the previously published work.

4.9.1 Creep of Horizontal Samples

Horizontal samples were tested using the same test procedure as for the vertical samples. Similar to the results from the vertical samples, Figure 39 demonstrates the overall magnitude of creep compliance is very similar for all zones despite the change of drilling bedding plane orientation. However, the magnitude of the creep compliance is different than the vertical samples, with the horizontal samples experiencing significantly lower overall compliance values. Again, the ductile zones experience significantly more creep over time than the reservoir samples.

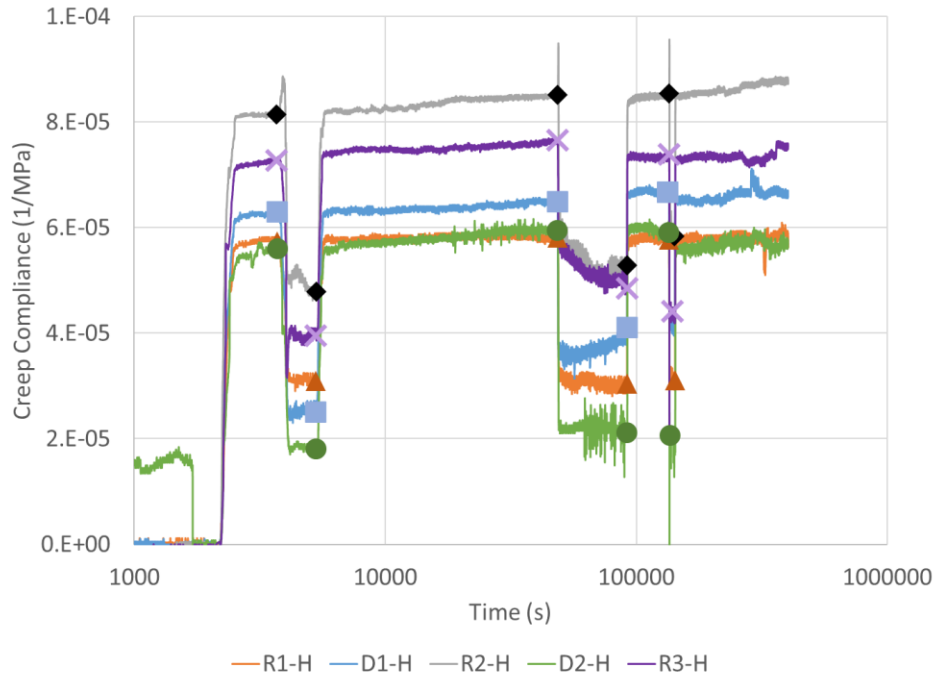


Figure 39 Creep compliance over time for horizontal samples

Unlike with the vertical samples, the two ductile samples did not experience the same amount of creep recovery. Ductile 1 recovered approximately 40% of the strain after the 20-minute load/unload cycle while Ductile 2 recovered approximately 30%. Both ductile zones appear to experience approximately the same amount of creep during the subsequent 12-hour load/unload stages. Again the samples appear to undergo strain hardening, not recovering as much after the first 20-minute load/unload cycle. The magnitude of compliance after the final 2-hour unload stage is approximately the same as after the 12-hour unload stage.

Reservoir 1 and Reservoir 3 recover approximately 50% of the applied strain, while Reservoir 2 recovers more at 60%. During the 12-hour load/unload stages, Reservoirs 2 and 3 experience more creep recovery during the 12-hour unloading stage than Reservoir 1. As with the ductile samples, the reservoir samples also appear to undergo strain hardening, not recovering a significantly greater amount of strain compared to the previous load/unload stages.

4.9.2 Creep of 45° Samples

To complete characterization of the creep properties, samples drilled 45° relative to bedding planes were tested using the same conditions as for the vertical and horizontal samples. The first significant difference noted in Figure 40 is the magnitude of the creep compliance for the 45° samples is lower than for the vertical or horizontal samples. However, all zones still have approximately the same magnitude of creep compliance. One note to make when examining the 45° data is the Ductile 2 zone did not provide a sample, and therefore no discussion can be made on data from this zone.

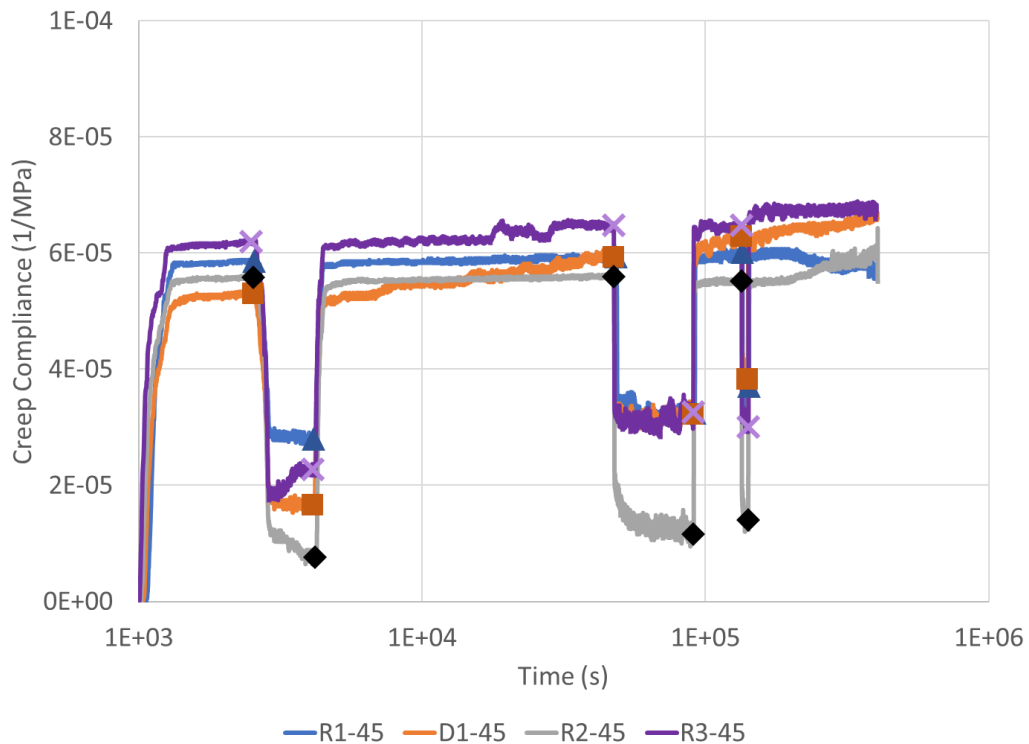


Figure 40 Creep compliance over time for 45° samples

The single ductile sample tested recovered approximately 30% of the strain applied during the initial 20-minute load/unload stage. As with the previous stages, the sample undergoes additional creep during the 12-hour and 72-hour loading stages, and based on the decrease in recovered strain during the 12-hour unload stage the sample also undergoes some strain hardening. The amount of creep in the ductile zone is noticeably more significant than the creep experienced by the reservoir zones. Interestingly, the behavior of the ductile sample drilled at 45° relative to bedding planes appears to more closely match the behavior of the sample drilled vertically from the same zone.

Reservoir 1 experiences the greatest amount of elastic strain recovery at 50%, while Reservoir 2 experiences the least at approximately 10% and Reservoir 3 recovers 35%. As with the experiments conducted on other orientations, the samples undergo some strain hardening, decreasing the amount of strain recovered during each unloading stage compared to the previous unloading stage. Similar to the horizontal samples, the reservoir samples do not appear to undergo a significant amount of creep during the subsequent loading/unloading stages until the final 72-hour loading stage.

4.9.3 Creep Behavior and Bedding Plane Orientation

One significant difference between the vertical and horizontal samples is the magnitude of the creep experienced by the samples at later stages of testing. The samples drilled parallel to bedding planes experience significantly lower creep than the samples drilled perpendicular to bedding planes. Testing methods were identical between the vertical and horizontal samples, and therefore most of the creep occurs in the bedding planes instead of the rock fabric.

This theory of the bedding planes being responsible for a significant portion of the creep is also supported by the samples drilled 45° relative to bedding planes. While the ductile zone obviously shows a greater amount of creep than the reservoir zones, the behavior of the samples falls somewhere between the behavior of the vertical and horizontal samples. Compared to the vertical samples the overall magnitude of creep compliance is decreased. The behavior of the Reservoir 1 sample more closely matches the behavior of the horizontal sample than the vertical sample. This is contrasted to the Ductile 1 sample, where the behavior of the 45° sample more closely matches the behavior of the vertical sample. The Reservoir 2 zone experienced the least amount of creep but also appears to slightly match the behavior of the horizontal sample, though the difference in behavior is difficult to determine. Finally, Reservoir 3 also appears to have closer correlation between the horizontal sample and the 45° sample compared to the correlation of the 45° sample to the vertical sample.

4.9.4 Long-Term Deformation of Horizontal Samples

In addition to the load/unload cycles, all samples were loaded for 72 hours and the creep compliance over time was calculated. Figure 41 demonstrates a significantly lower tendency to creep for samples drilled parallel to bedding planes. While the overall trends are the same between the horizontal and vertical samples, the creep compliance over time for the horizontal samples is significantly lower.

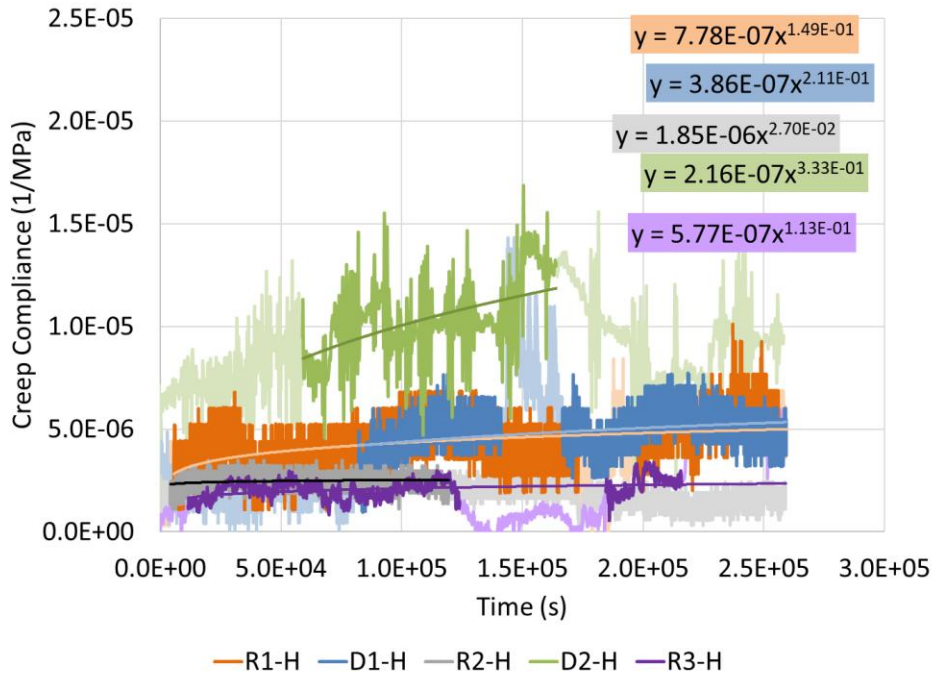


Figure 41 Power-Law fit to horizontal samples

Once again, the ductile zones have a higher time exponent than the reservoir zones, and all samples have similar values of creep compliance throughout the 72-hour loading stage. Extrapolation out to longer period of time shows the ductile zones quickly experiencing greater deformation than the reservoir zones. Once again Reservoir 2 is the region which will undergo the least amount of creep. However, instead of Ductile 1 undergoing the greatest amount of deformation, for the samples drilled parallel to bedding planes Ductile 2 appears to be the most susceptible to creep over time.

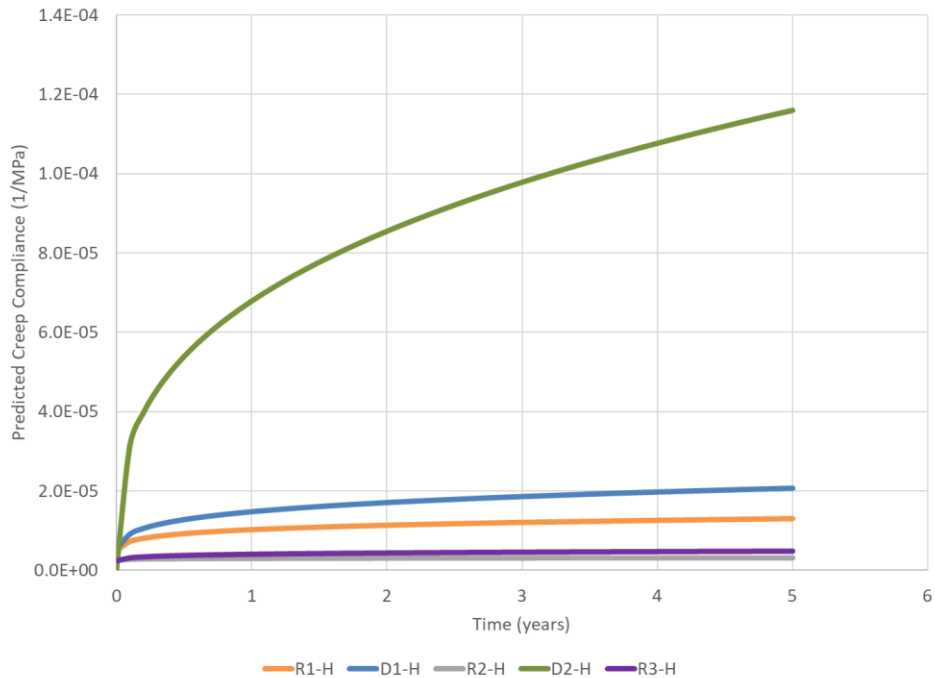


Figure 42 Predicted creep compliance for horizontal samples over five years

Another item of note is the magnitude of the time exponents is very similar for all samples, and there is significantly more noise in the deformation measurement compared to the vertical samples. It is possible there is some additional noise in the signals confusing which zones will creep more when comparing Reservoirs 1 and 3 and Ductile 1 and 2. However, the trend of the ductile zones deforming significantly more than the reservoir zones and Reservoir 2 being the least susceptible to creep remains unchanged.

4.9.5 Long-Term Deformation of 45° Samples

Finally, the 45° samples in Figure 43 demonstrate similar behavior as seen with the creep compliance over time when comparing these samples to samples from the other two orientations.

The magnitude of the creep compliance is significantly lower than for the vertical samples and more closely matches the compliance of the horizontal samples. Examining the time exponent, the ductile zone once again has a higher magnitude than the reservoir zones, as demonstrated in the five-year predicted creep compliance in Figure 44.

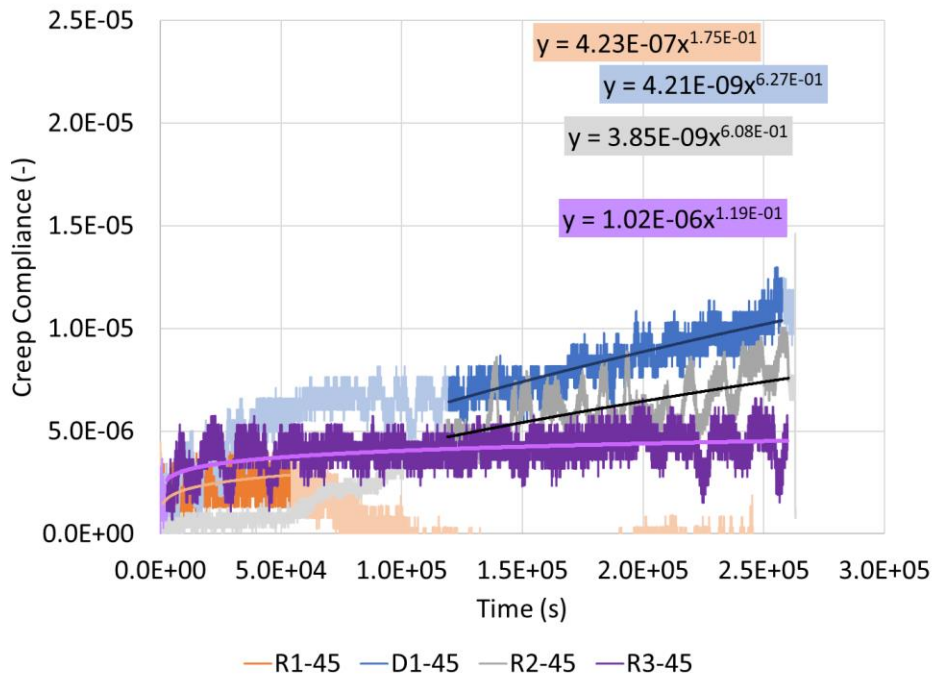


Figure 43 Power-Law fit to 45° damples

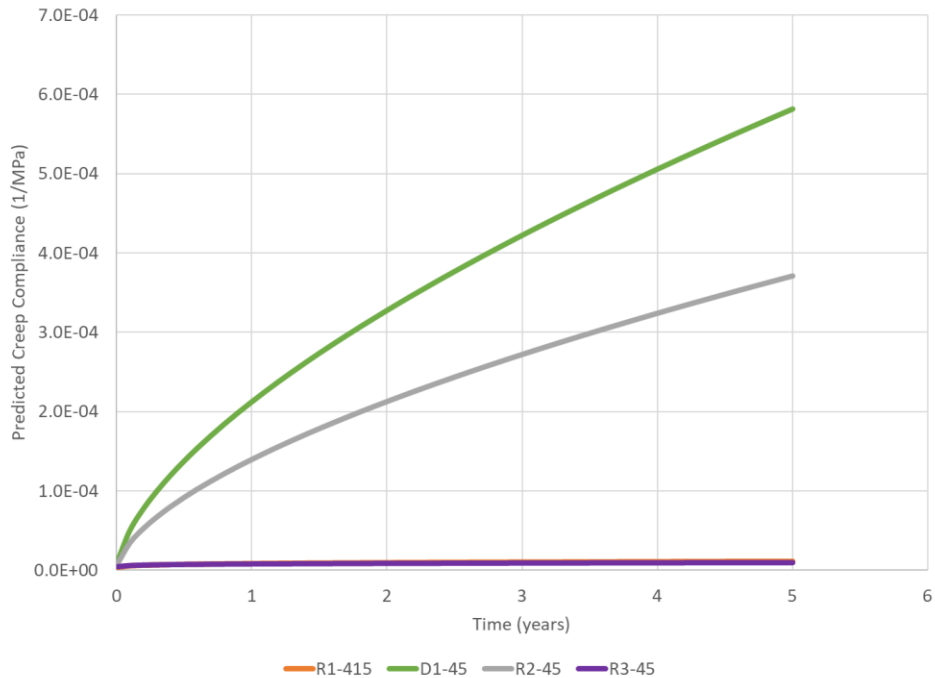


Figure 44 Predicted creep compliance for 45° samples over five years

As with the horizontal samples, the low magnitude of creep compliance increases the uncertainty due to noise in the LVDT signal at very low displacements. This is most clearly demonstrated with Reservoir 2, which in all previous tests experienced the least amount of creep deformation instead showing one of the highest tendencies toward creep when tested at 45° relative to bedding planes. This additional displacement could also be due to the sample twisting while in the cell under the applied loads, causing the top plate of the load frame where the LVDTs are measuring the relative displacement to measure greater displacements than the direct axial displacement of the sample.

Examining the time exponents for each sample, Ductile 1 has a value between those determined using the horizontal and vertical samples. However both Reservoir 1 and Reservoir 3 have values lower than those measured from the other two tests, and Reservoir 2 has an exponent significantly higher than the other two tests.

4.9.6 Creep and Bedding Planes

Creep testing provided a clear distinction between the nominally brittle and nominally ductile zones which unconfined and triaxial testing were unable to provide. The ductile zones clearly demonstrated a tendency to undergo significantly more long-term displacement than the more brittle reservoir zones. This is reflected most clearly when examining the power-law fit for the 72-hour loading stage, where the ductile zones will quickly pass the reservoir zones in displacement when the power-law fit is extended past 90 days. This trend held true for the vertical and horizontal bedding plane orientations, with a potential question of measurement reliability in the 45° samples. This means regardless of the angle a well would intersect the Caney formation, the ductile zones would still be expected to undergo significantly more creep and deformation than the reservoir zones.

Unsurprisingly, the orientation of the bedding planes in shale samples has a significant impact on the measured properties. As an anisotropic material, the properties of the shale in a given plane are not necessarily the same as the properties in a plane orthogonal to the first. Due to the nature of how the shale is formed, the shale can be considered transversely isotropic when considering a sample drilled perpendicular to the bedding planes. This can be seen most clearly in the results from creep testing, where the samples drilled perpendicular to the bedding planes experienced significantly more creep deformation than the samples drilled parallel to the bedding planes.

This difference in creep over time due to the orientation of the bedding planes implies most of the creep occurs in the bedding planes themselves. If the creep occurred in the rock and not the bedding planes, the magnitudes of creep would be similar between the vertical and horizontal

samples. Instead, the significant decrease in creep leads to the conclusion the anisotropy seen in the creep parameters is due to the creep occurring in the bedding planes.

There is an additional complication seen when examining the 45° results. Unlike with the other samples, during load application it was more likely these samples would rotate in the test cell during the load/unload cycles. Due to the method used to set up the equipment, this would result in the rotation of the relative positions of the LVDTs with respect to the sample. This twisting behavior, while small, could result in either higher or lower displacement of individual LVDTs compared to a sample which did not experience this rotation. This impact was compounded by the small magnitude of displacement measured during the 45° testing, as any additional change in the signal would significantly impact the calculated axial strain. This behavior is likely why Reservoir 2, which for all other tests was the least likely to undergo creep deformation, instead showed the greatest amount of displacement during testing.

While there was a clear difference between the horizontal and vertical samples, there was not a consistent trend of the 45° samples relative to the other orientations. The Reservoir 1 and Reservoir 2 samples appeared to be closer to the behavior of the horizontal sample while the Ductile 1 sample more closely matched the vertical sample from the same formation. While difficult to determine due to the low amount of creep deformation experienced by the Reservoir 2 samples, the 45° sample also appeared to more closely match the horizontal sample. Based on these trends, it would be expected the Ductile 2 sample, which could not be obtained for testing, would more closely match the vertical sample, as the ductile zones appear to more closely match the samples drilled perpendicular to bedding planes while the reservoir zones appear to more closely match those drilled parallel to bedding planes.

5.0 Formation Stress Model

This chapter presents an in-situ stress model developed using the finite element program Abaqus (Abaqus, 2011). Properties for the model were obtained from analysis of laboratory triaxial and creep tests. The finite element model is compared against two models available in the literature. One is a basic elastic model of layer stresses and the other is an analytical creep model of the evolution of layer stresses.

5.1 Introduction

When designing a stimulation plan for hydrocarbon extraction, two main factors determine the overall approach. The first factor is the set of properties of the formation, which include composition and material properties. The second factor is the in-situ stresses present in the formation. In many cases, both of these factors are unknown and must be estimated using indirect methods such as well logs (see for example Wong 2007).

A case study performed on the Caney shale provides a good opportunity for determining both the properties of the formation and predicting the in-situ stresses based on those properties and known variables about the formation. Located in Oklahoma, the Caney shale is an emerging play under examination for development. Initial testing examined the material properties of the Caney shale (Benge et al. 2021a) and the influence of creep properties on the long-term productivity of a formation with specific emphasis on examining proppant embedment and fracture closure due to creep (Benge et al. 2023). The amount of fracture closure depends on the amount

of creep the formation will experience, with the creep a function of the applied stresses. A validated model to predict the in-situ stresses could be used to provide a more accurate prediction of fracture closure, with the in-situ stresses applied as they would be in the formation.

This chapter focuses on the development, validation, and results of a three-dimensional finite element model of the stress state in the layered Caney shale. While model limitations require the properties of the shale to be simplified to an isotropic material, the two extremes of properties are examined by modeling both the vertical and horizontal properties. After validating the model, the main focus of the study presented is to examine how the inclusion of both creep and tectonic strains improves the estimation of in-situ stresses, specifically highlighting the difference between the presented model and the current model as presented in literature by Sone and Zoback (2014a and 2014b). Of specific interest is an examination of how layers with different properties, here differentiated as “ductile” or “brittle”, impact the relative stress magnitudes of the different zones in the formation.

5.2 Background

Fractures will only form if the pressure exceeds the minimum principal stress of the formation (see for example Economides and Nolte, 1987). An initiated fracture will orient so the fracture opening is in the direction of the least principal stress and will grow preferentially in areas with lower stresses. By predicting the magnitude and orientation of the principal stresses, it is possible to predict fracture growth in a formation with multiple layers of differing properties. Stress prediction therefore is directly relevant to stimulation design and operations, as the stresses are the main controlling factor for fracture growth, size, and orientation.

Previous research has used numerical techniques including finite element analysis to analyze the stresses and strains in a formation. However, while these often noted the changes in stresses over time due to relaxation or creep, this was not the main focus of the model (see for example Sasaki and Rutqvist, 2022). Others compared only the dynamic properties of the shale to the well log and did not account for long-term deformation in their prediction of current in-situ stresses (see Wong et al., 2008). Some models, such as the one presented by Min et al. (2004), examined how stresses in the formation impact permeability. Predictably, higher stresses result in decreased permeability compared to lower stresses. However, this examination did not include creep behavior which would alter the stress state over time by allowing for stress relaxation.

Zobeiry et al. (2016) presented a finite element model with a user subroutine created in the finite element software Abaqus to describe a transversely isotropic polymer. These authors used a Prony series approximation to describe the creep behavior of a fiber reinforced polymer. While the authors were able to validate their response against multiple analytical models, a Prony series description of creep is not always applicable to a material and may require assumptions such as predetermined relaxation times in order to be implemented (see for example Bažant and Jirásek, 2018).

Li et al. (2020) presented a modified Burgers model for transversely isotropic rocks. The authors conducted laboratory testing on phyllite to determine creep properties and calculate creep parameters. The creep parameters were calculated based on a linear fit for the Maxwell portion of their creep model and a logarithmic equation for the Kelvin portion of the model based on the stress applied to the sample during testing.

The work presented by Sasaki and Rutqvist (2022) examines the impact of creep properties on the integrity of shale. While the main goal of the model was to examine the long-term integrity

with respect to nuclear waste disposal, results from the model did identify changes in the stress profile of the formation due to the creep behavior of the shale. For example, the model showed a shale with a high tendency to creep would relax completely with no deviatoric stress while a shale less prone to creep may only experience a 50% decrease in deviatoric stress. This demonstrates why the creep properties of shale are important when determining the in-situ stresses in a formation, as a single formation can have widely varying stresses depending on the properties of different zones in the single formation.

Finally, the work by Sone and Zoback (2014a and 2014b) has inspired the characterization of creep properties for prediction of stresses in the Caney shale. However, the authors only predicted the horizontal in-situ stresses, creating a mathematical model based on the power-law creep parameters and a constant tectonic strain rate. This method was able to be validated against well logs (Sone and Zoback, 2014a).

This chapter presents a finite element model created in the commercial software program Abaqus to calculate the in-situ stresses in the Caney shale. While limiting the scope to a single formation, the methodology and model presented can be modified to be applicable to any formation. This is a continuation of ongoing research to characterize the Caney shale from both a properties perspective (Benge et al. 2023) and a geomechanical perspective.

5.3 Baseline Geomechanical Model

For comparison to the common method of predicting in-situ stresses in a formation, a geomechanical model with no creep was created in the finite element software Abaqus. As will

be demonstrated in this chapter, Abaqus was chosen to allow the model to be expanded to include creep behavior after establishing the baseline stress profile of the formation.

5.3.1 Model Assumptions

Several basic assumptions were made for establishing the finite element model. First, it was assumed the material was linearly elasto-viscoplastic, where the deformation is separated into an elastic component and a viscoplastic creep component. Second, it was assumed each zone of interest was relatively homogeneous, which allows a single set of properties to be applied to each zone. This assumption was necessary because there were a limited number of available samples. Similarly, the scale at which the formation was modeled is assumed to be large enough small inconsistencies or inclusions can be considered to have negligible impact on the calculation of stresses and are therefore not included in the model.

Abaqus does not allow a transversely isotropic material to include anisotropic creep behavior. Developing a transversely isotropic creep law and implementing the behavior in Abaqus was outside the scope of this thesis. Instead, the isotropic model was run twice with two sets of material properties. A model created with the vertical creep properties served as an upper bound to the expected amount of creep. The lower bound of expected creep was calculated using the properties obtained from horizontal samples. As demonstrated in Section 4.9, the vertical samples experienced the most creep out of all the tested orientations and the horizontal samples experienced the least, with the 45° samples providing creep properties between the other two orientations. The 45° samples providing properties between the other two orientations indicates there is not an orientation where there is more creep than the vertical samples, and no orientation where there is less creep than the horizontal samples. This method, using the vertical samples to provide an

estimate of behavior using the most creep-prone set of properties and using the horizontal samples for the least creep-prone, provides an upper and lower bound to behavior with respect to creep properties, and can be used to estimate an upper and lower bound of the corresponding horizontal stresses as calculated using the two sets of creep properties.

If the exact properties of a region of the formation are unknown, it would be possible to estimate the properties using the orientation of the bedding planes. Results from testing the 45° samples indicate the properties do not transition linearly between the vertical and horizontal directions. While ideally more orientations would be tested, the 45° samples still provide a midpoint for estimating properties based on the bedding plane orientation, and additional orientations could be estimated as a proportional change between the 45° samples and either the vertical or horizontal samples depending on the desired bedding plane orientation. A further correlation could be made to the seismic velocity of the formation; however this is outside the scope of the project.

The model also assumes there is a proportional relationship between the Young's modulus of the vertical and horizontal samples. Due to the small number of samples, the horizontal samples could not be characterized using triaxial testing. To determine a relative Young's modulus for these samples, the Young's modulus as calculated during the loading ramps of the creep tests was used to obtain a proportional change between the vertical and horizontal samples. This proportional change was then applied to the static Young's modulus of the vertical samples as determined from triaxial testing to approximate the Young's modulus of the horizontal samples as if they had undergone the same testing. Poisson's ratio was assumed to be the same between both the vertical and horizontal samples. See Section 2.2.7 for a more detailed description of this process.

5.3.2 Formation Stress Model Setup

A formation scale model was created to represent a portion of an analog to the Caney formation. The goal of this model was to predict the in-situ stresses in the formation based on the overburden pressure and assumed tectonic strains using the properties from laboratory testing.

To create the model, the range of each of the zones needed to be extended vertically. While the five zones of interest are the focus of this study, additional regions were present between the zones of interest which were not selected for mechanical testing. While ideally samples would be available throughout the entire depth of interest, this would require an unreasonable number of samples and demand considerable laboratory resources. Therefore, the zones of interest were extended vertically to meet each other, removing the areas of the formation which were not selected for analysis from the model. The midpoint between the bottom of the upper layer and top of the next layer of interest was selected as the point to allow the zones of interest to meet. This is illustrated in Figure 45(A) with the model sections colored to indicate the different zones of interest. The mesh is displayed in Figure 45(B).

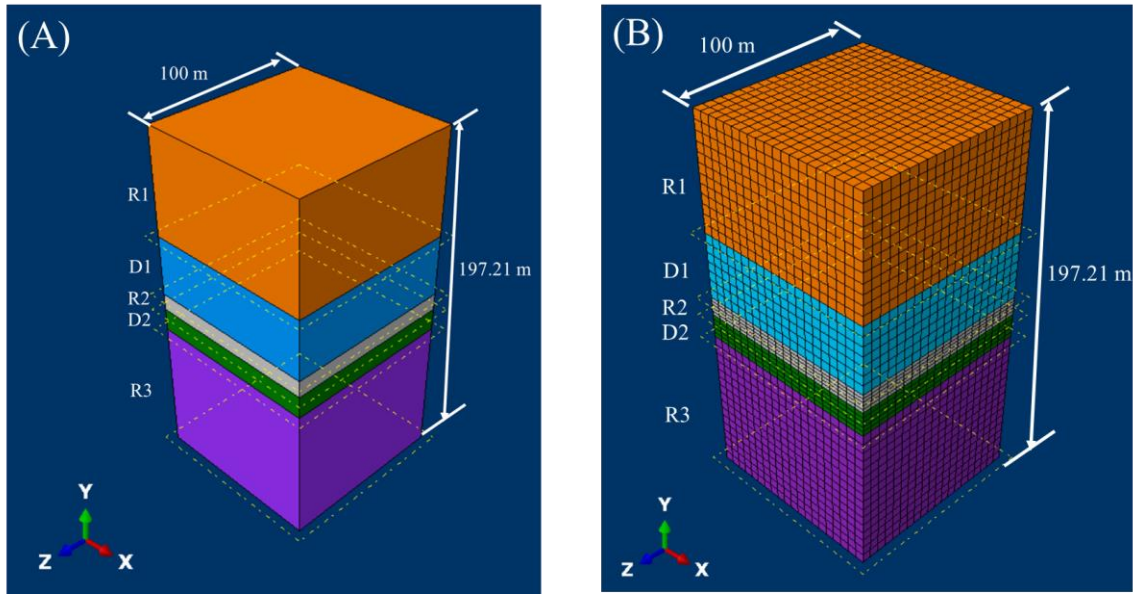


Figure 45 (A) Analog formation stress model colored by zone and (B) the mesh used in the analysis of the analog formation model

Each side of the model in the x-z plane was 100 m (328 ft) in length, with the idea of being a large enough rectangular prism to minimize edge effects. Heights for each zone were determined based on the well log and the aforementioned extension of the zones to eliminate gaps in the model. The formation model was created as a single homogeneous unit which was then sub-divided into each zone of interest. Each subsection was then assigned the appropriate properties with respect to depth. Creating the formation as a single unit and then subdividing meant the zones were not able to separate from or overlap each other, and nodes would be aligned at the intersection between two zones.

Boundary conditions for the formation model included the application of a gravity load to the entire model and applying an overburden pressure to the top of the Reservoir 1 subsection. The overburden pressure was chosen to be 20.67 MPa (3000 psi) to match the pressure used in laboratory testing. The sides of the formation had an applied constant displacement rate which

would produce a nominal strain rate to represent the tectonic strains in the Earth's crust. The minimum horizontal strain was set to either 100 or 1000 μ strain, with a velocity calculated so the model would reach the specified strain at the end of the simulation. A ratio of 1.5 was chosen to relate the maximum to minimum horizontal stresses. This is intended to capture a range of possible tectonic strains, as exact tectonic strains for the Caney formation were not available. Finally, to prevent rigid motion of the model, the bottom surface of the model was fixed to prevent movement along the vertical (y) direction, and a single node on the bottom surface was additionally fixed in the horizontal directions (x and z) to prevent translation and rotation of the model. This is illustrated in the simplified diagram of Figure 46.

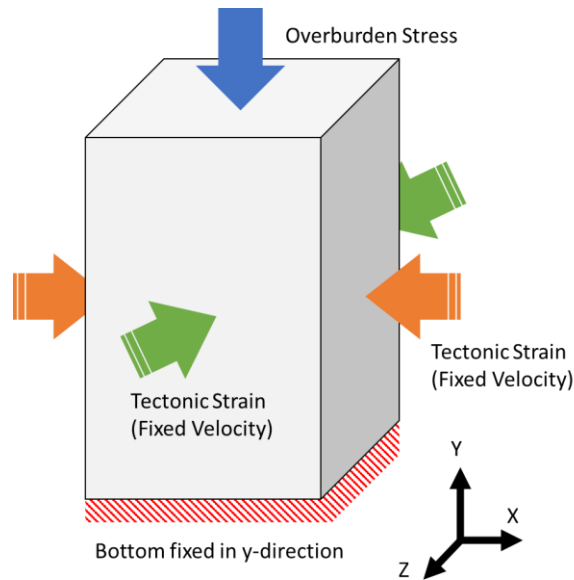


Figure 46 Diagram of formation stress model boundary conditions

The formation stress model assumes a monotonic loading state, with constant overburden stress and constant tectonic strain rates. While the tectonic strains present in the crust may change slowly over time, the tectonic strains were assumed to be constant for the duration of the

simulation. Similarly, though the Caney was deposited on the surface and would not have experienced a constant overburden stress through all time, assuming a constant set of boundary conditions simplifies the model.

Of specific interest in the model are the magnitude of horizontal stresses with respect to the depth through the formation. To determine the stresses as a function of depth, a set of nodes at the same initial x and y coordinates were chosen, creating a vertical depth line through the formation. The nodes along this line from the top to the bottom of the model were then used to generate the stresses with respect to depth which will be displayed in this chapter. These nodes were located in the same initial x and y coordinates approximately halfway between the edge of the model and the center, removing any possible effects caused by the edge of the model and avoiding the center point where the middle node was fixed to prevent translational movement of the model. The nodes at the top and bottom surfaces of the model were removed as these would be affected by the applied boundary conditions. This vertical line of nodes is shown in Figure 47.

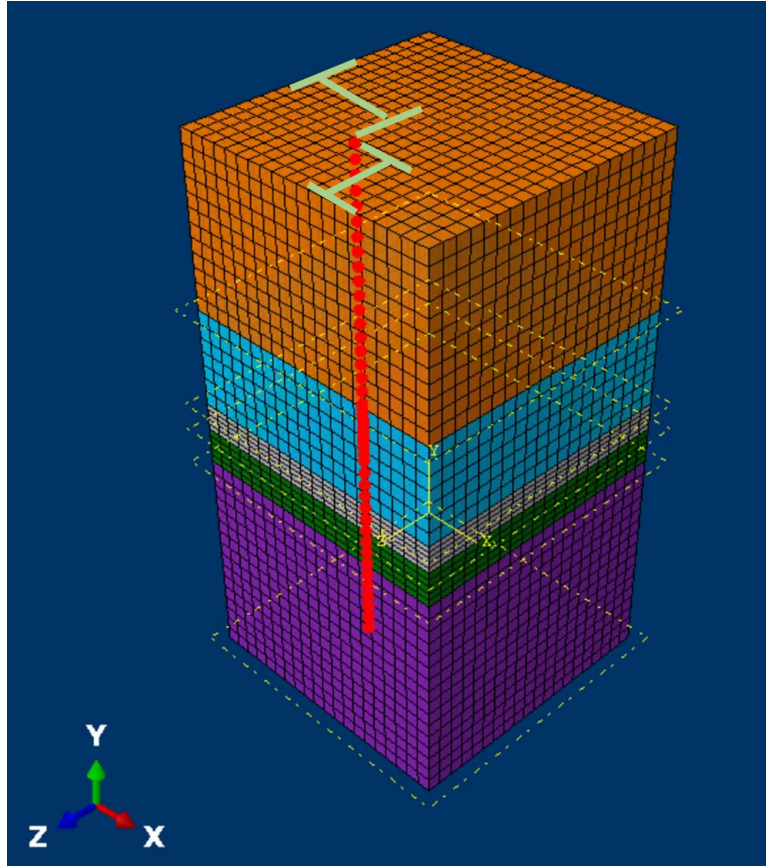


Figure 47 Highlighted nodes used for analysis to determine stress with respect to depth through the formation

For reference, the properties of each zone are provided in Table 4. As mentioned previously, the bedding planes are assumed to be parallel to the x-z plane and the y-direction refers to the depth of the formation. The vertical properties assume the model is oriented perpendicular to the bedding planes while the horizontal properties are for a model oriented parallel to the bedding planes.

Table 4 Formation model input parameters for each zone

Parameter		Reservoir 1	Ductile 1	Reservoir 2	Ductile 2	Reservoir 3
Vertical Properties	Young's Modulus (Pa)	2.68x10 ¹⁰	3.79x10 ¹⁰	2.39x10 ¹⁰	2.10x10 ¹⁰	3.03x10 ¹⁰
	Poisson's Ratio (-)	0.190	0.195	0.218	0.156	0.179
Horizontal Properties	Young's Modulus (Pa)	3.16x10 ¹⁰	5.62x10 ¹⁰	2.99x10 ¹⁰	3.67x10 ¹⁰	3.48x10 ¹⁰
	Poisson's Ratio (-)	0.190	0.195	0.218	0.156	0.179

5.3.3 Formation Model Verification

A numerical check was used to ensure the formation model was able to correctly calculate the stresses. To calculate the case for zero tectonic strain, a 1D calculation was used (Eaton, 1969)

$$\sigma_h = \sigma_v \frac{\nu}{1 - \nu} \quad (5.1)$$

Where the horizontal stress σ_h is calculated from the vertical stress σ_v and Poisson's ratio ν .

Equation (5.1) allows for the 1D calculation of the horizontal stress based on the overburden, and results are provided in Figure 48 to compare the initial and calculated horizontal stresses with respect to depth. In this case, the tectonic strain was not included in the simulation,

as this is not accounted for in the equation. Note the y-axis is the depth into the formation, where the top of the formation is the point where the 20.68 MPa (3000 psi) overburden is applied.

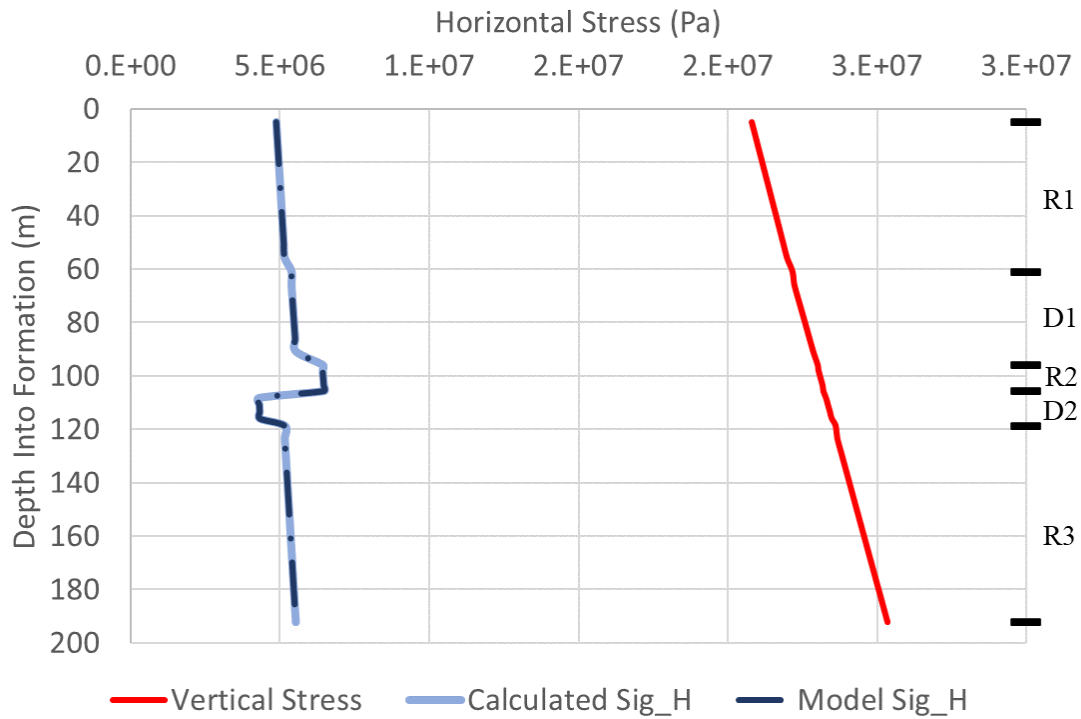


Figure 48 Verification of initial horizontal stress for baseline geomechanical model

A second verification was conducted by setting the tectonic strains in the horizontal direction to a large value, equivalent to a strain rate of 0.002 1/s for both the x and z directions, while removing the vertical stress. By plotting the stress vs strain curve for the horizontal stress in this scenario, it is possible to recover values very close to the input Young’s modulus values. The values are demonstrated in Figure 49, showing the model is able to recover the Young’s modulus to within less than one percent of the input values in this scenario.

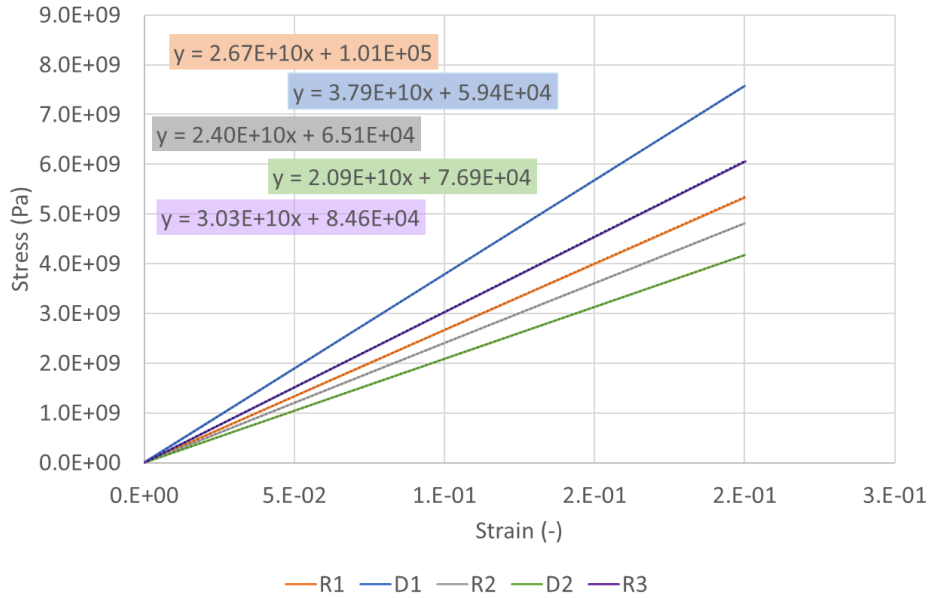


Figure 49 Recovery of Young’s modulus values for baseline geomechanical model

5.4 Inclusion of Tectonic Strains

With the horizontal stresses and elastic behavior verified, a set of three simulations were run to demonstrate the influence of tectonic strain rate on the elastic behavior of the formation. These simulations were run on a model containing the vertical properties and a model with the horizontal properties. First, the baseline with no tectonic strain demonstrated the properties determined if only the overburden stresses are taken into account. Second and third, a constant tectonic strain rate of 100 and 1,000 μ strain were applied, equivalent to a displacement of 0.005 and 0.05 m (0.197 and 1.97 inches) applied to each side of the model. Strains in the x and z-directions were set to be equivalent for these simulations.

Figure 50 demonstrates the influence of including tectonic strain in the baseline geomechanical model. Note this model does not include any creep properties. The baseline case

is identical for both the vertical and horizontal properties, as the Poisson's ratio was the same for both models. As shown in equation (5.1), the Young's modulus does not play a role in calculating the horizontal stress when the tectonic strain is not included in the model, and therefore both the vertical and horizontal properties produce the same initial stress profile.

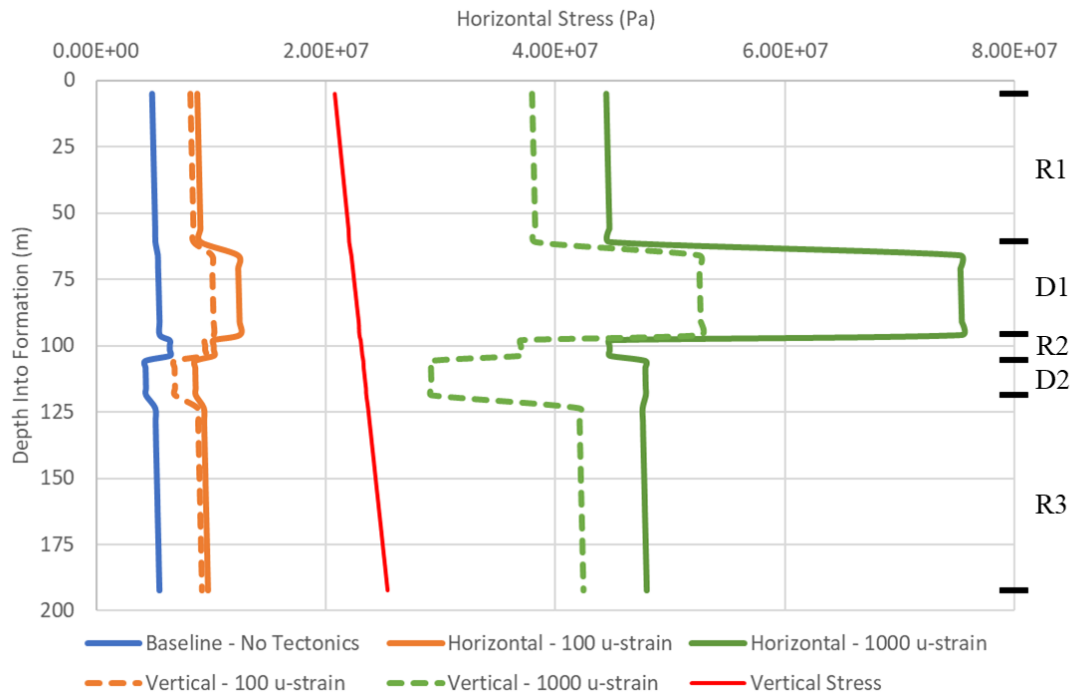


Figure 50 Baseline geomechanical finite element models with 100 and 1,000 μ strain for vertical (dashed) and horizontal (solid) properties

The baseline model also shows Reservoir 2 as a potential fracture barrier, as the relatively high Poisson's ratio of this zone results in an increase in predicted horizontal stresses. Similarly, the zone with the lowest Poisson's ratio, Ductile 2, is predicted to have the lowest horizontal stress. Based only on the baseline calculation and not accounting for tectonic strains or creep, Ductile 2 would be seen as a target zone for stimulation with the anticipated result fractures would be well-

contained by the relatively higher stresses in Reservoir 2 and Reservoir 3. However, looking at the models which include tectonic strains, it becomes evident the baseline model which does not account for tectonic strains will lead to misleading conclusions.

For both the horizontal and vertical models, including 100 or 1,000 μ strain of tectonic strain increases the horizontal stresses by approximately two or three orders of magnitude, respectively. Simply accounting for the presence of a tectonic strain significantly increases the anticipated stresses in the formation, which must be accounted for not only during stimulation but also during drilling to ensure wellbore stability.

In both cases with tectonic strain included in the model, the relative increase or decrease in stresses for each of the zones is the same. Both sets of properties show a significant increase in horizontal stresses for the Ductile 1 zone, creating a clear differentiation between Reservoir 1 and Ductile 1 which is substantially more subtle in the baseline case. This also increases the stress in Ductile 1 above the stresses in Reservoir 2, which changes the Ductile 1 zone from a potential target of stimulation to a likely barrier to fracture growth. However, there is a significant difference in the other zones between the model created using the vertical properties and the model created using the horizontal properties.

For both models, Reservoir 2 has lower stresses than Ductile 1, changing from a barrier to fracture growth into a potential stimulation target when comparing the two zones. However, the Ductile 2 zone has a lower stress than Reservoir 2 in the vertical model and slightly higher stress in the horizontal model. This is caused by the relative changes in Young's modulus, which resulted in a higher Young's modulus in the horizontal model compared to the vertical model. As previously discussed, this factor was based on the elastic portion of the load/unload curve during creep testing, and the horizontal value of Young's modulus is an estimated adjustment of the

vertical Young's modulus assuming a proportional change based on these load/unload ramp values. The relatively high Young's modulus of the Ductile 2 zone in the horizontal model results in a higher stress while the relatively low modulus of the vertical model results in lower stresses. This means depending on the properties used in the model, Ductile 2 would be seen as a target for stimulation based on the vertical properties and a barrier to fracture growth based on the horizontal properties.

The inclusion of tectonic strains significantly changes the zones identified as either targets for stimulation or barriers to fracture growth. Additionally, the use of either the vertical or horizontal properties changes the relative increase or decrease of stresses when accounting for the influence of tectonic strain. These conclusions demonstrate the purely elastic model shown in Equation (5.1) is not sufficient to describe the in-situ stress state of a formation, especially when the formation is undergoing tectonic strain.

5.5 Inclusion of Creep in Geomechanical Model

While accounting for tectonic strains improves the stress calculations for a formation, other behaviors need to be taken into account. Of specific interest in this case is the creep, or long-term deformation behavior of the Caney. As the formation was previously thought to be susceptible to long-term deformations by being identified as a nominally "ductile" formation, examining the influence of creep behavior on the in-situ stresses will demonstrate the creep behavior needs to be accounted for in predicting in-situ stresses to avoid significant errors.

5.5.1 Analytical Creep Model

A study by Sone and Zoback (2014b) demonstrates the culmination of a project to create a single equation to account for the change in in-situ stresses over time, taking into account both elastic and creep components of strain. The authors combined the elastic and creep strains to allow the Laplace transform to convert between stress and strain calculations (Sone and Zoback 2014a). This method has the advantage of providing a single equation to calculate the accumulated differential horizontal stress $\Delta\sigma(t)$ as a function of an average tectonic strain rate $\dot{\epsilon}$, creep parameters B and n, and time.

$$S_{Hmax} - S_{Hmin} = \Delta\sigma(t) = \dot{\epsilon} \frac{1}{B(1-n)} t^{1-n} \quad (5.2)$$

Where S_{Hmax} and S_{Hmin} are the maximum and minimum horizontal stresses respectively, t is the time in seconds, and B and n are the creep parameters as calculated from the creep compliance (see Section 4.5). Other than the difference of including the elastic strain when calculating B and n, the calculation of the creep parameters by Sone and Zoback (2014a and 2014b) and the study presented in this thesis are the same.

As this calculation determines the difference between the maximum and minimum horizontal stresses, additional calculations are required to determine the in-situ stresses using this method. One factor which must be determined either from field data or assumed from laboratory testing is the stress ratio Φ , calculated as the ratio of the three principal stresses, S_1 , S_2 , and S_3 .

$$\Phi = \frac{S_2 - S_3}{S_1 - S_3} \quad (5.3)$$

Using this stress ratio then allows for calculation of the maximum and minimum horizontal stresses, though the equations will vary depending on the faulting regime. For example, the equations for the normal faulting regime ($S_V > S_{Hmax} > S_{hmin}$) are

$$S_{Hmax} = S_V + (1 - \Phi)\Delta\sigma(t) \quad (5.4A)$$

$$S_{hmin} = S_V - \frac{1}{\Phi} \Delta\sigma(t) \quad (5.4A)$$

While the equations for a strike-slip faulting regime ($S_{Hmax} > S_V > S_{hmin}$) are

$$S_{Hmax} = S_V + (1 - \Phi)\Delta\sigma(t) \quad (5.5A)$$

$$S_{hmin} = S_V - \Phi \Delta\sigma(t) \quad (5.5B)$$

Sone and Zoback (2014a and 2014b) assume a strike-slip faulting regime, which will be maintained for this examination of the analytical model.

Importantly, this method estimates the maximum and minimum horizontal stresses as a function of the vertical stress and does not directly calculate the stresses in the formation. Additionally, it requires either the measurement or assumption of a stress ratio value Φ . This stress ratio value must be either estimated based on information such as drilling-induced fractures or with extensive knowledge of in-situ stresses (Sone and Zoback, 2014b). This has the obvious limitation of requiring significant information about stresses prior to calculating the stresses, which

means this method is not usable for fields where no stress information is known, such as in an exploration well.

In addition to the issue of requiring knowledge of the principal stresses, the reliance on using the vertical stress to determine the horizontal stress has the same inherent limitations as other approaches and results essentially in a scaling factor applied to the vertical stress based on a physical property. In this case it is the creep behavior instead of Poisson's ratio as in (5.1), but the approach is very similar.

The one-dimensional analytical model for stress in (5.2) is acknowledged to be sensitive to the tectonic strain rate. The authors also caution laboratory testing of core samples under appropriate conditions is required to obtain representative creep parameters.

5.5.1.1 Parameters for Analytical Creep Model

Unlike the method previously described to calculate the power-law creep parameters, Sone and Zoback (2014a and 2014b) did not offset the creep strain by the elastic portion of the strain, instead selecting B and n values which represent the total strain. The authors indicate the Young's modulus is approximately equal to the inverse of the B parameter, which further ties together the elastic and creep strains.

To calculate the equivalent parameters for the Caney shale, and to align the analytical model to the properties used in the Abaqus finite element model, the B and n parameters were calculated without offsetting the elastic strain. An example of this is provided for the horizontal samples in Figure 51, and Table 5 lists the B_Z and n_Z parameters calculated using this method, the subscript Z indicating the method developed by Zoback (Sone and Zoback, 2014a).

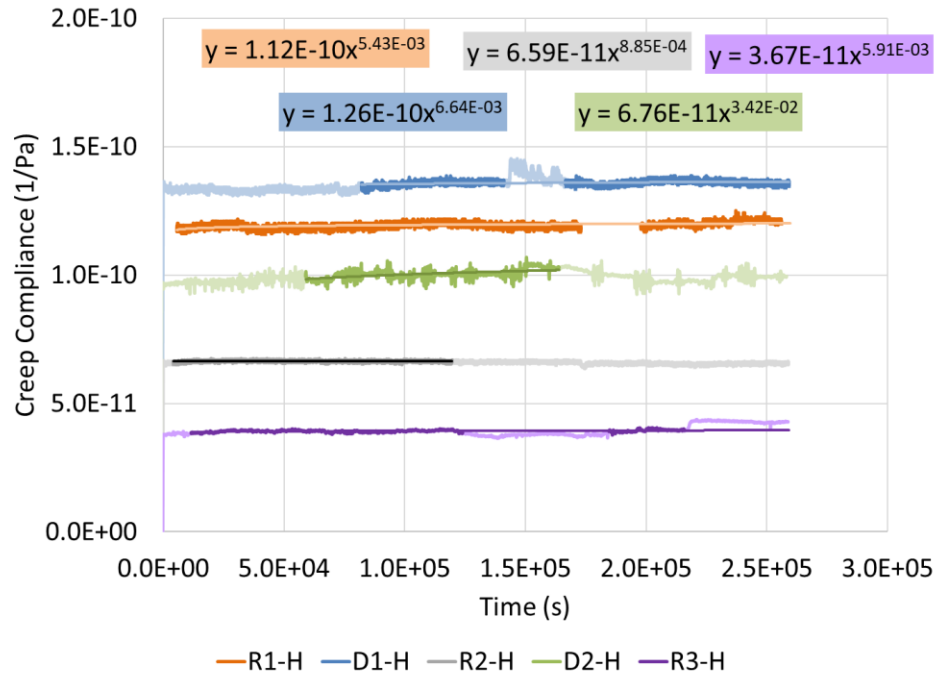


Figure 51 Example calculation of creep parameters without elastic offset (horizontal samples)

Table 5: Horizontal creep parameters calculated without elastic strain offset

Zone		Bz (1/Pa-s)	nz (-)
Horizontal Samples	Reservoir 1	1.12×10^{-10}	5.43×10^{-3}
	Ductile 1	1.26×10^{-10}	6.64×10^{-3}
	Reservoir 2	6.59×10^{-11}	8.85×10^{-4}
	Ductile 2	6.76×10^{-11}	3.42×10^{-2}
	Reservoir 3	3.67×10^{-11}	5.91×10^{-3}

The first significant difference between the method presented by Sone and Zoback (2014a and 2014b) and the method presented in this thesis is the magnitude of the B and n parameters. Without offsetting the total strain by the elastic portion of the strain, the n-values which control the amount of creep experienced over time are significantly diminished, for example the horizontal

values changed from the order of 1×10^{-1} down to orders of 1×10^{-3} . This difference in values will result in very different calculated amounts of strain for a given time frame between the two models.

5.5.1.2 Analytical Prediction of In-Situ Stresses

As demonstrated (see Section 5.4), the magnitude of the tectonic strain has a significant influence on the in-situ stresses for the formation. Therefore, a constant tectonic strain rate of 1×10^{-19} 1/s was selected to represent the tectonic strains for the in-situ stress model with a ratio of 1.5 between the maximum and minimum tectonic strains. This value is based on Sone and Zoback (2014b) for the Barnett shale, both for comparison to the published work and to represent a tectonic strain rate at a location far away from active plate tectonics. The value of 1.5 was chosen as the ratio of tectonic strains to provide an average middle ground between equal strains with a ratio of 1 and a maximum ratio of 2. This resulted in the minimum tectonic strain of 1×10^{-19} and a maximum tectonic strain of 1.5×10^{-19} .

The analytical model requires a constant stress ratio Φ to be predefined for a formation to calculate the final stresses (Sone and Zoback, 2014b). Because the stress ratio needs to be either measured or assumed to use the Zoback method of calculating horizontal stresses, several values of Φ were used to predict the maximum and minimum horizontal stresses for the model. In this case, only the horizontal properties are used in the model, as they provided additional readability in results compared to the vertical properties. Figure 52 demonstrates the influence of different Φ values on the predicted maximum and minimum stresses. It should be noted a typical value of Φ is most likely closer to one than zero, but a wide range of values are shown here to include a wide variety of possible stress states, and to demonstrate the behavior of the analytical model for different values of Φ .

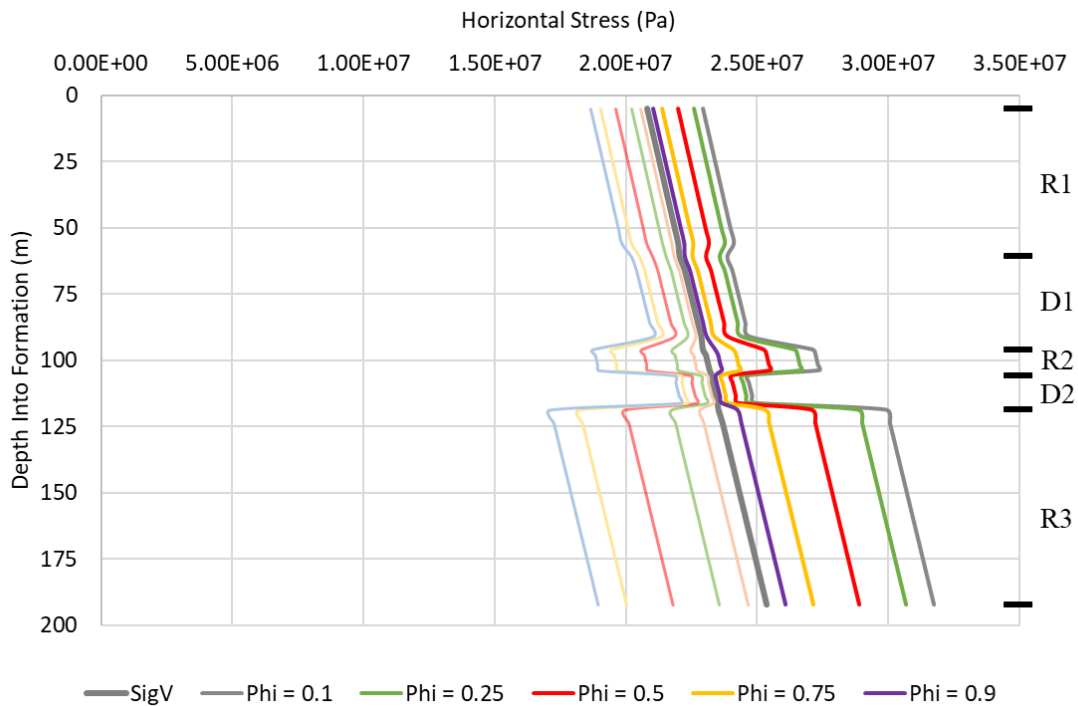


Figure 52 Predicted horizontal stress ranges for analytical model with various stress ratios, maximum stress (dark) and minimum stress (light) plotted with vertical stress

A higher value of Φ results in higher maximum stresses and lower minimum stresses. The stress ratio acts as a multiplier to the difference in stress as calculated using the creep model in (5.2). While this behavior could be predicted by examining the equations (5.5A) and (5.5B), this demonstrates more clearly how the approach presented in Sone and Zoback (2014a and 2014b) provides a range of possible stress values based on the ratio of stresses.

It is possible to estimate an approximate ratio of stress values, either using preexisting information about the stresses or by taking into account the geologic history of the basin. For example, sedimentary basins which have relaxed will likely have a Φ closer to 1. Meanwhile, a region which experiences very high differential stresses applied to rock not prone to creep may have a Φ value further from 1.

Based on their greater tendency to creep, the ductile zones are expected to act as fracture barriers and demonstrate more creep deformation over time than the reservoir zones. This is the case when examining the minimum horizontal stresses, as the ductile zones are predicted to have higher minimum stresses than the reservoir zones. However, the Ductile 1 zone and Reservoir 1 zone do not show a significant difference in stresses, and the difference is small enough a fracture initiated in Reservoir 1 may propagate into Ductile 1. By contrast, Reservoirs 2 and 3 would be well-contained, as they have significantly lower stresses than the surrounding Ductile zones. It is likely this is caused by the similar B_Z values of the two zones (Table 5). This result shows one of the ductile zones acting very similar to one of the reservoir zones, which is against what would be expected based on the behavior of the samples under laboratory conditions.

The similarity of the stresses in Reservoir 1 and Ductile 1, and the requirement of calculating the principal stress ratio Φ highlight two concerns with the analytical model. This model requires preexisting knowledge of the stress state which might be difficult to obtain, especially in unexplored formations. Instead of an analytical model, this thesis examines a finite element simulation to calculate in-situ stresses, which does not require the preexisting knowledge of stresses and includes a more creep-oriented power-law.

5.5.2 Finite Element Simulation

Because creep significantly impacts the in-situ stress calculation, the model presented in Section 5.4 was expanded to include creep behavior. As previously demonstrated, the power-law description of creep provides a good description of the long-term creep deformation for the Caney shale (Benge et al., 2023). Abaqus has a built-in power-law creep behavior, described using equation 5.6A (Abaqus, 2011). The A , s , and m parameters are the inputs used in Abaqus to

describe the power law, calculated using the parameters from laboratory testing in equations 5.6B through 5.6D.

$$\dot{\varepsilon} = A * \sigma^s * t^m \quad (5.6A)$$

$$\varepsilon = B * \sigma * t^n \quad (5.6B)$$

$$\dot{\varepsilon} = (B * n) \sigma t^{n-1} \quad (5.6C)$$

$$A = B * n \quad s = 1 \quad m = n - 1 \quad (5.6D)$$

Using the creep parameters from laboratory testing to determine the Abaqus inputs, the vertical and horizontal models were extended to allow for creep in their corresponding directions. It was assumed the creep properties for each zone are homogeneous and uniform. As mentioned previously, two versions of the model were created, one using the properties from vertical samples (drilled perpendicular to bedding) and one using the properties from the horizontal samples (drilled parallel to bedding), with the goal the two models will provide the upper and lower bound of possible stresses.

The most significant difference between this finite element model and the approach presented by Sone and Zoback (2014a and 2014b) is the separation of the elastic and creep strain components prior to calculating the power-law creep parameters. By separating the elastic and creep components of the strain, the model is able to calculate the initial stress state and then account for the influence of creep.

The potential issue of combining the elastic and creep strain into a single term such as the one presented by Sone and Zoback (2014a and 2014b) is the creep may be overshadowed by a relatively larger elastic strain. While the creep strain may be larger than the elastic strain when

examining the geologic time scale, the laboratory tests which are used to determine the creep strain are by requirement significantly shorter. This shorter time scale for laboratory tests means the amount of creep a laboratory sample is able to undergo is limited. For samples with a low tendency to creep, the method presented by Sone and Zoback (2014a and 2014b) might underestimate the amount of creep because relative to the elastic strain the creep strain is extremely small. The method presented here separates the elastic and creep strain, which ensures even small creep strains are accounted for when calculating the power-law equation of creep. As will be shown, this may result in overestimations of creep for very creep-prone formations but ensures low-creep formations (such as Reservoir 2) are accounted for when predicting creep deformation.

Separating the elastic and creep strains ensures even formations with very low or very high amounts of creep are able to be accounted for. Additionally, as demonstrated in Chapter 4.0, offsetting by the elastic strain allows samples tested under different stress conditions to be compared regardless of the applied axial stress or Young's modulus of the samples. This method would also allow the comparison of different formations and different test conditions, allowing more direct comparisons which may lead to additional insights into the long-term deformation behavior of formations.

5.5.2.1 Laboratory Scale Model and Creep Parameter Calibration

Before the analog formation could be simulated with creep, the parameters from the power-law fit and their corresponding Abaqus input values needed to be calibrated against the available laboratory data. Therefore a laboratory scale model was created to simulate the creep testing conducted in the laboratory. The goal of this laboratory-scale model was to predict the axial strain during a simulated 72-hour creep test and verify the results against the measured data.

This would demonstrate the creep properties were correctly predicting the change in strain over time for the samples.

Two laboratory-scale models were constructed to match the samples drilled vertically and horizontally relative to bedding planes. Each model consisted of a rectangular prism with a side length of 0.3 m (1.18 inches) and a length of 0.6 m (2.36 inches) to match the 30 x 60 mm cylinders used for testing. The cylindrical laboratory sample was modeled as a rectangular prism to allow the elements to align with the axes and remove the potential for error when using curved elements or elements not aligned with the principal directions. A single point in the center of one side of the sample was used as the point to determine strain to mimic the use of the strain sensors and LVDTs used in testing.

As shown in Figure 53 and Figure 54, the model was able to accurately predict the axial strains measured by the LVDTs. The power-law data from the laboratory analysis of creep was able to be input into the Abaqus software using a simple derivative with respect to time, as the software defines the creep strain as a rate instead of the direct strain. Because the calculations for the model included an offset of the elastic strains, the B parameter was slightly adjusted as needed to align with the laboratory data. This slight modification was allowed because the process to calculate the creep parameters included offsetting the elastic strain. Depending on the data points chosen to calculate the elastic strain, this value would vary slightly, giving different B values. Therefore, the small adjustments made to the B-value input into the finite element model were deemed acceptable as this was a simple offset to match the laboratory data and did not impact the overall development of the creep strain.

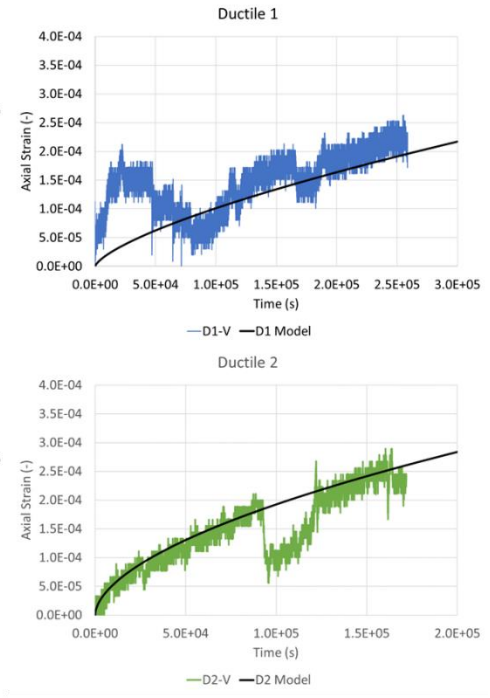
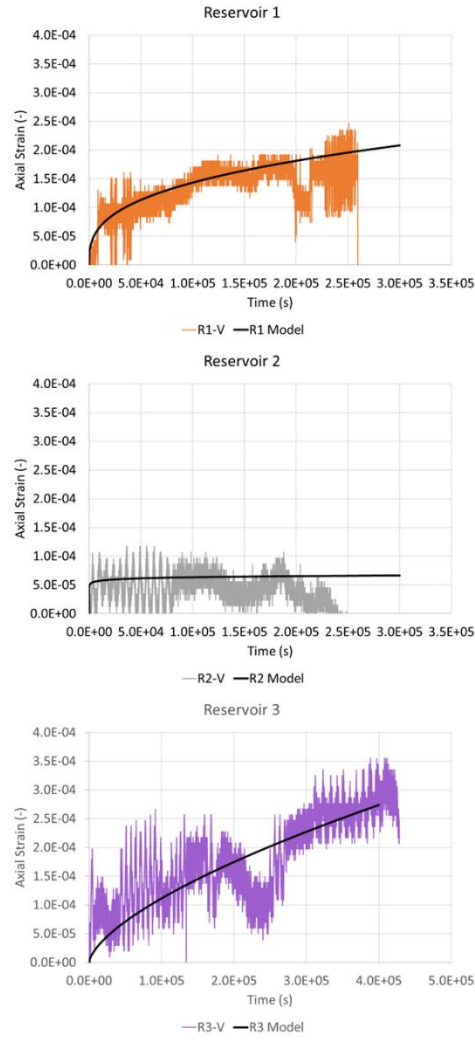


Figure 53 Validation of vertical creep model using laboratory scale model

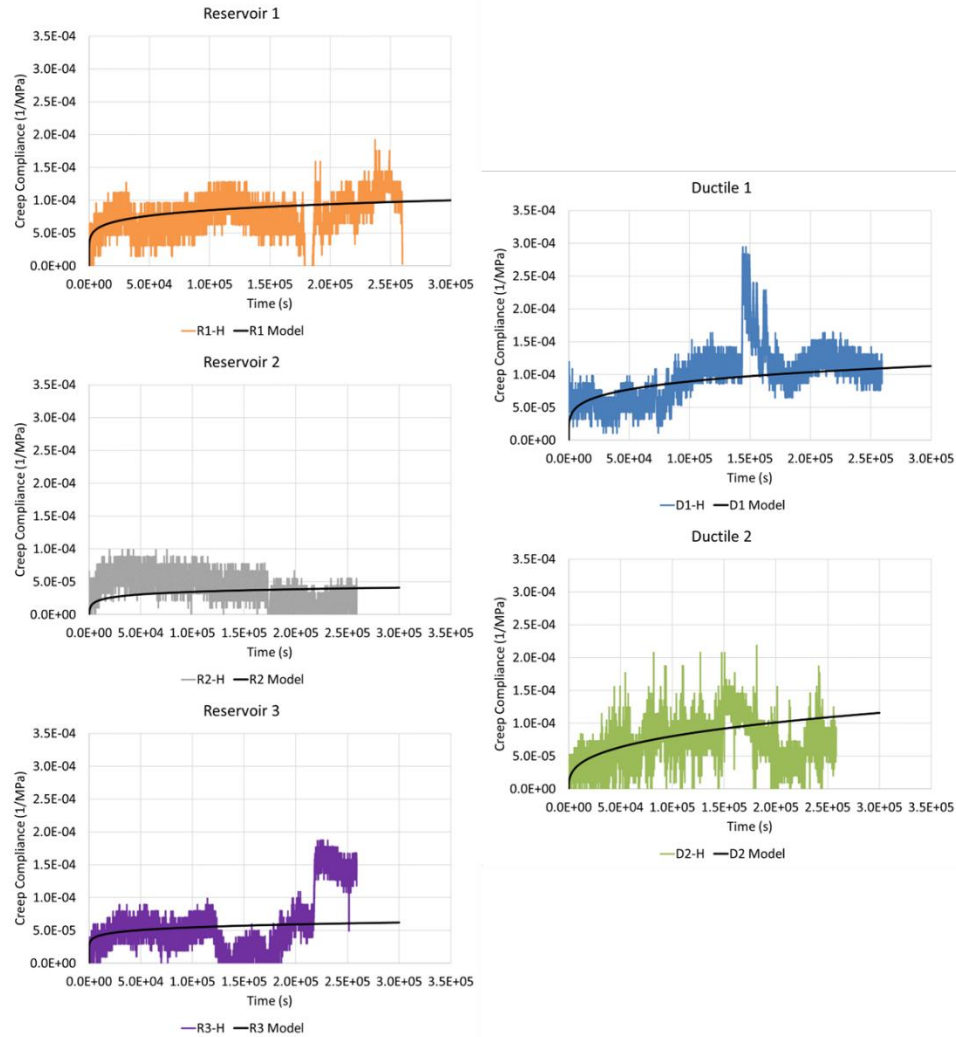


Figure 54 Validation of horizontal creep model using laboratory scale model

As discussed, the B-values used as inputs to the creep model needed to be slightly adjusted. In addition to the variation caused by the offset of elastic strain, the finite element model assumes a perfect material, and this is very rarely the case in laboratory testing. Variations in material properties, the presence of small microcracks or inclusions, and noise in the signal from sensors can all contribute to the inconsistencies between the laboratory data and the finite element model. Therefore, small adjustments were allowed to be made to the B parameter, as shown in Table 6.

Table 6 Creep values adjusted to match laboratory results

Zone		Laboratory Values		Adjusted B Value
		B (1/Pa-s)	n (-)	B (1/Pa-s)
Vertical Samples	Reservoir 1	3.86×10^{-14}	-0.661	5.00×10^{-14}
	Ductile 1	1.14×10^{-15}	-0.307	1.40×10^{-15}
	Reservoir 2	8.11×10^{-14}	-0.956	4.00×10^{-14}
	Ductile 2	1.18×10^{-14}	-0.440	1.10×10^{-14}
	Reservoir 3	1.59×10^{-15}	-0.351	1.59×10^{-15}
Horizontal Samples	Reservoir 1	1.16×10^{-13}	-0.851	1.16×10^{-13}
	Ductile 1	8.14×10^{-14}	-0.789	8.50×10^{-14}
	Reservoir 2	5.00×10^{-14}	-0.973	1.00×10^{-13}
	Ductile 2	7.19×10^{-14}	-0.667	4.00×10^{-14}
	Reservoir 3	6.52×10^{-14}	-0.887	6.52×10^{-14}

Because the adjustments made to the B values were small, and because the finite element model was able to match the creep strain over time as shown in Figure 53 and Figure 54, the model was deemed to be calibrated to the laboratory data.

Prior to examining the stresses in the analog formation model, the mesh size was verified using multiple mesh sizes. Once the appropriate mesh size to ensure convergence of the solution was determined, the time step used to simulate the model was also examined. It was found the solution converged when the incremental time step was set to be two orders of magnitude less than the total simulation time.

As an experiment, the parameters as determined using the method of Sone and Zoback (2014a and 2014b), where the creep compliance was not offset by the elastic portion of the strain, was tested using the analog formation model. It was found the significantly lower n -values of the power-law description of creep (Table 5) created a numerical error when the creep law was extended to more than one million years. The numerical error resulted in the strain increasing exponentially quickly, reaching an invalid number during the simulated time. This is why the analytical model is presented separately from the finite element model, as the numerical issue in the finite element simulation caused by the higher n -values could not be resolved by adjusting the mesh or the time stepping method used in the model.

5.5.2.2 Influence of Creep on Formation Model

With no additional changes needed in the analog formation model, and the mesh size of the full formation model determined, the model was run to predict the in-situ stresses of the Caney formation. The initial model was run for 350 million years, approximating the age of the Caney shale as it was formed during the Mississippian age (Cardott, 2017). For comparison to the previous models which did not include creep (as presented in Figure 50), 100 and 1000 μ strain were applied to the formation. This strain was applied as a velocity boundary condition, meaning the displacement rate was calculated so the model would start the simulation with no strain and the strain would reach the specified value at the end of the simulation. In this case, the model would reach either the 100 or 1000 μ strain after 350 million years of simulated time.

Figure 55 provides the final stresses of the formation at the end of the 350 million years of simulated time with 100 μ strain applied. Included are the reference lines for the previous 100 μ strain models which did not include creep.

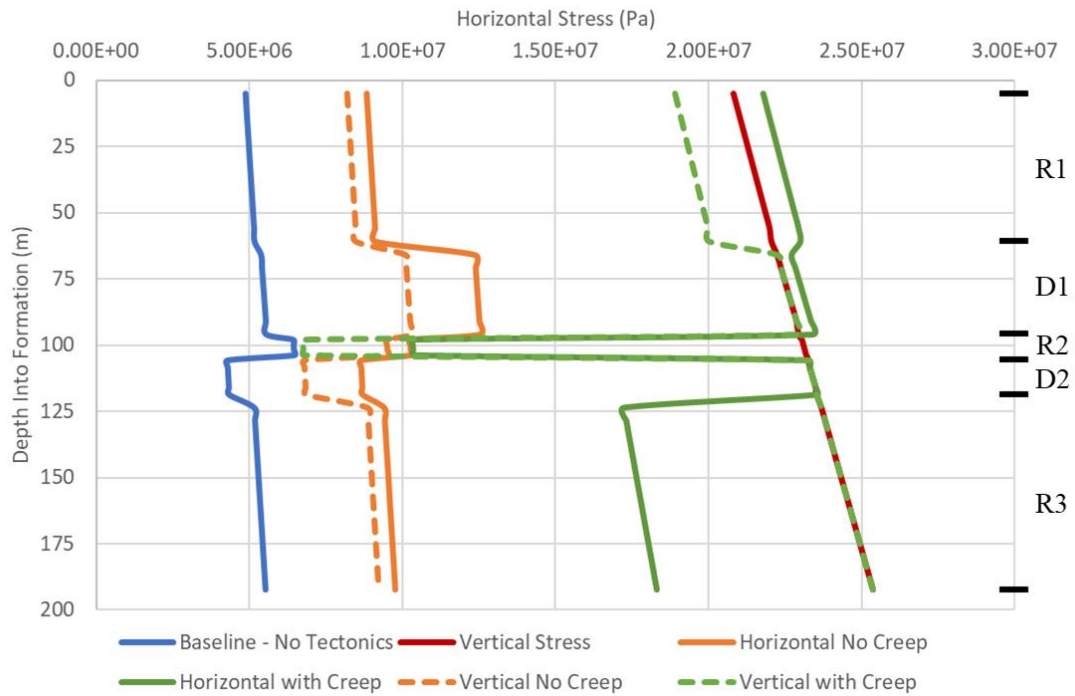


Figure 55 Comparison of horizontal (solid) and vertical (dashed) models with and without creep with 100 μ strain applied

The most significant difference between the two models is every zone except Reservoir 2 has significantly higher stresses when creep is included in the model. As Reservoir 2 experienced almost no creep, the vertical model predicts almost no change in stress while the horizontal model predicts the same final stress as the model with no creep for this zone.

Most interestingly, Ductile 2 changes from being a target for fracture growth to a clear barrier to fracture growth, with horizontal stresses approaching the vertical stresses for this zone. Unlike in the models which do not include creep, a fracture started in Reservoir 3 would not be expected to propagate into Reservoir 2 because Ductile 2 will act as a barrier to fracture growth.

Ductile 1 differs between the vertical and horizontal models. For the more creep-prone vertical model, Ductile 1 has higher stresses than Reservoir 1, and a fracture initiated in the

uppermost zone would not be expected to propagate further into the formation. However, the higher stresses in Reservoir 1 as calculated using the horizontal model indicate fractures will preferentially propagate through the lower stress formations below, meaning a fracture initiated in Reservoir 1 may propagate through Ductile 1 and even into Reservoir 2. The relatively higher stresses of Ductile 1 and Ductile 2 indicate once a fracture is either initiated in or grows into Reservoir 2, it will grow preferentially in this zone and not propagate into the surrounding zones of higher stress.

Examining the deeper zones of the vertical model, the Ductile 2 and Reservoir 3 zones have reached a stress value essentially proportional to the vertical stress. This indicates the vertical model is reaching a steady state with lithostatic stresses by the end of the simulation while the horizontal model is still developing stresses. Because the vertical model essentially reaches lithostatic stress state before the completion of the simulation, the remainder of the discussion will focus on the model made with the horizontal properties.

5.5.2.3 Impact of Tectonic Strain Magnitude and Application Rate

The impact of both tectonic strain magnitude and the inclusion of creep behavior have been demonstrated. Applying the tectonic strain over the lifetime of the formation while accounting for stress relaxation results in significantly different stress values compared to a model which accounts for only one or none of these factors. The remaining question is how the magnitude of the tectonic strain influences the horizontal stresses, and if the time frame of the application has a significant impact on the final stresses.

Examining the behavior of the horizontal model, a small test matrix was created to determine how the application and magnitude of the tectonic strains impact the in-situ stresses. As the age of the Caney is estimated to be Mississippian (Cardott, 2017), an approximate age of the

formation was selected as the midpoint of this era at 350 million years. For comparison to a much shorter time period, 3.5 million years will represent a younger formation. It is likely these time frames will encompass most formation ages and will further demonstrate any clear differences between stresses based on the rate at which the tectonic strain is applied. For both time frames, one model was run with an ultimate tectonic strain load of 100 μ strain and a second model was run with an ultimate tectonic strain load of 1000 μ strain. Again, the purpose of this range is to not only show how an order of magnitude difference impacts the in-situ stresses, but to also include what is the most common range of values measured in the field.

Figure 56 provides the final stresses for the 100 and 1000 μ strain, both examined for the estimated 350 million year age of the formation.

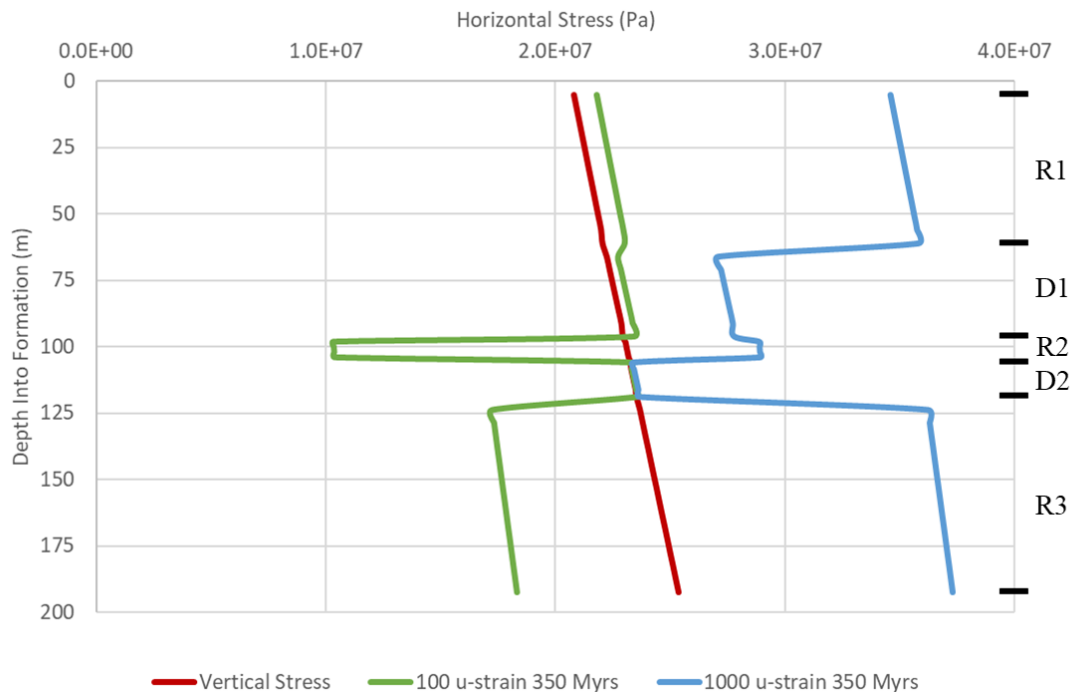


Figure 56 Final horizontal stresses influenced by tectonic strain

The first major result of this simulation is the 1000 μ strain case predicts stresses which are above the vertical stresses, meaning the formation would be in a strike-slip faulting regime. This is not the intended conclusion of the model, and it is not suggested the formation is undergoing a change in faulting regimes. Instead, the 1000 μ strain case is intended to be examined only as a relative change to higher total stresses compared to the 100 μ strain case. As will be discussed, the specific intent behind using this higher strain is to illustrate the transition from relaxation-driven behavior to elasticity-driven behavior.

A second important conclusion is the Ductile 2 zone approaches a horizontal stress which is essentially equal to the vertical stress. This is the tendency of more creep-prone zones noted by Sone and Zoback (2014a and 2014b), where zones which undergo more deformation due to creep approach a lithostatic stress state.

Examining the difference between the 100 and 1000 μ strain cases, the higher tectonic strain corresponds to higher overall stresses, which makes a logical sense given the change in boundary conditions. More interestingly, the 100 μ strain and predicts Ductile 2 as a fracture barrier and Reservoir 2 as a region where fractures will grow preferentially, while the 1000 μ strain model predicts the opposite. In both models, regardless of the application speed, the Ductile 2 zone appears to reach a stress value proportional to the vertical stress and then does not increase significantly more. By contrast, the 100 μ strain cases predict the Reservoir 3 zone as relaxing and experiencing less strain than the Ductile 2 case while the 1000 μ strain case shows the stresses in Reservoir 3 as being higher than in Ductile 2. This emphasizes how the 1000 μ strain case is reacting more to the application of the tectonic strain, producing an essentially elastic effect, while the 100 μ strain case is still able to relax most of the stresses to produce stress differences in the formation.

The main conclusion from this examination is the higher strain rate of the second model, and by extension the higher overall strain values, results in an elasticity-driven behavior in the reservoir zones while a more relaxation-driven behavior persists for the ductile zones. This is more in line with the classical version of geomechanical modeling. However, at lower strain values, when the behavior is more relaxation-driven, the reverse holds true, and zones which are thought to act as barriers to fracture growth in classical geomechanical modeling instead become targets for fracture growth due to their lower relative stress.

To examine more in-depth how the model behavior is more relaxation-driven or elastic-driven, Figure 57 presents the stress development over time for the 100 μ strain model. The stress development of each zone is represented by a midpoint located at the approximate vertical center of each zone. Note Figure 57(A) has a logarithmic time scale while Figure 57(B) has a linear time scale.

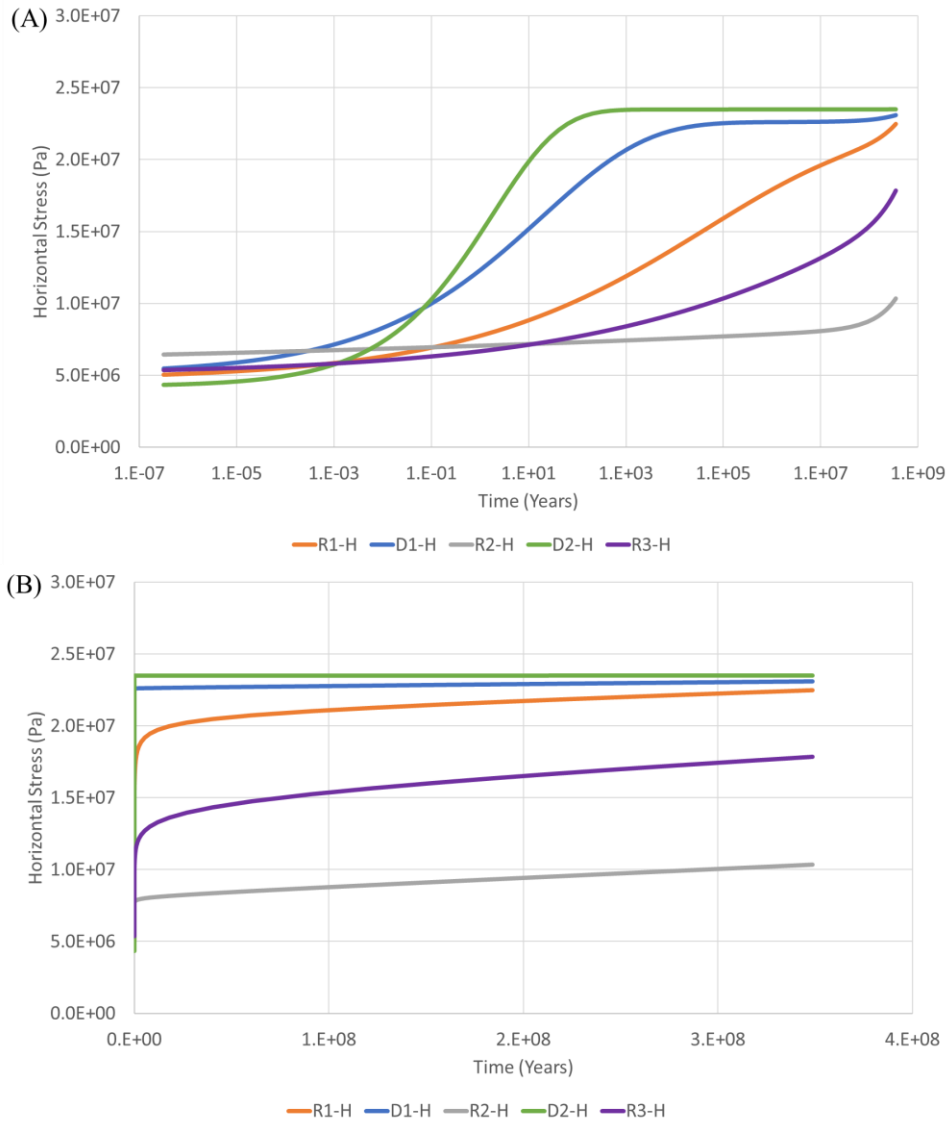


Figure 57 Stress development over time for 100 μstrain model simulated over 350 million years, (A) with logarithmic time scale and (B) with linear time scale

Examining the short-term behavior seen in Figure 57(A), the two Ductile zones are quickly relaxing due to the vertical stresses and reaching a constant stress state. The three Reservoir zones are much slower to relax. At the end of the logarithmic time scale (Figure 57(A)), the stress appears to quickly increase. Moving over to the linear time scale in Figure 57(B), this sudden increase is actually a linear increase over time, distorted due to the logarithmic time scale. Figure

57(B) shows the Ductile zones have maintained their relaxed stress state, and the slight increase in Ductile 2 over time is likely due to the application of the tectonic strains, meaning it is an elastic reaction to the increasing strains. Reservoir 1 and Reservoir 3 still relax until approximately one million years, at which point the tectonic strain has reached a high enough level the behavior changes from relaxation-driven to elasticity-driven and the stress increases linearly with the tectonic strains. Finally, Reservoir 2 shows very little relaxation, and instead appears to behave almost entirely as an elastic material. As Reservoir 2 was the zone least prone to creep, this helps validate the behavior, as almost no relaxation-driven behavior is seen and instead Reservoir 2 acts mostly as an elastic material.

Figure 57 helps explain the relative differences in stress seen in Figure 56, where most zones act almost as expected except for the relative stresses of Reservoir 1 and Ductile 1, where the tectonic strains begin to increase the stresses in Reservoir 1 due to the transition between relaxation-driven behavior and elasticity-driven behavior. The same examination can be made of the 1000 μ strain model by examining Figure 58.

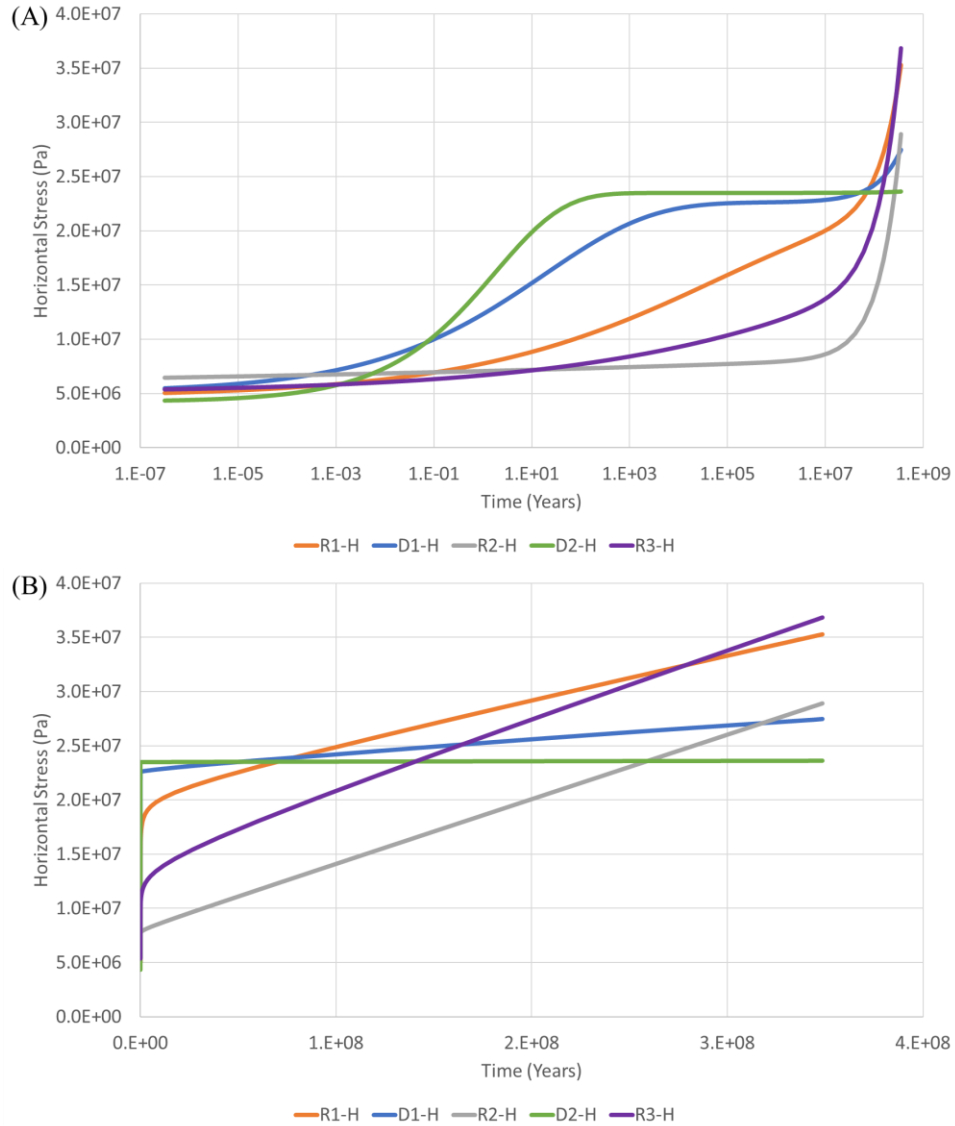


Figure 58 Stress development over time for 1000 μstrain model simulated over 350 million years, (A) with logarithmic time scale and (B) with linear time scale

Compared to the 100 μstrain case, all zones except Ductile 2 are reacting in a more elastic way due to the higher total tectonic strains. The increase in strains seen at 10 million years in Figure 58(A) are shown to be this transition to elastic-driven behavior in Figure 58(B). Interestingly, Ductile 1 appears to be able to maintain its relaxed state, which is supported by the fact Ductile 1 has the highest Young's Modulus value of the horizontal samples. Figure 58(B)

also shows the two more creep-prone reservoir zones, Reservoir 1 and Reservoir 2, still experience some relaxation until transitioning to an approximately elastic behavior. Another interesting behavior seen in this higher total strain model is Reservoir 3 surpasses Reservoir 1 in stress. Reservoir 3 has a slightly higher initial stress than Reservoir 1, and this trend is repeated in the final stresses. Finally, Ductile 2 also begins to transition from relaxation-driven to elasticity-driven behavior due to the higher tectonic strain values. Based on this trend, a model which applied sufficient tectonic strains would essentially recover the relationship between Young's modulus values for the formation, a behavior which is verified by returning to the elastic verification of the model seen in Figure 49.

Having examined the influence of the magnitude of the tectonic strain, the next question to answer is how the rate of application of the strain impacts the stresses in the formation. For a comparison to the 350 million years simulating the age of the formation, a second set of models was created to simulate a 3.5 million year old formation. This time frame was chosen not only to provide a comparison using two orders of magnitude difference, but to capture a wide range of potential formation ages, from the order of millions to hundreds of millions of years old. A comparison of all the models, with different tectonic strains applied over different time scales, is provided in Figure 59.

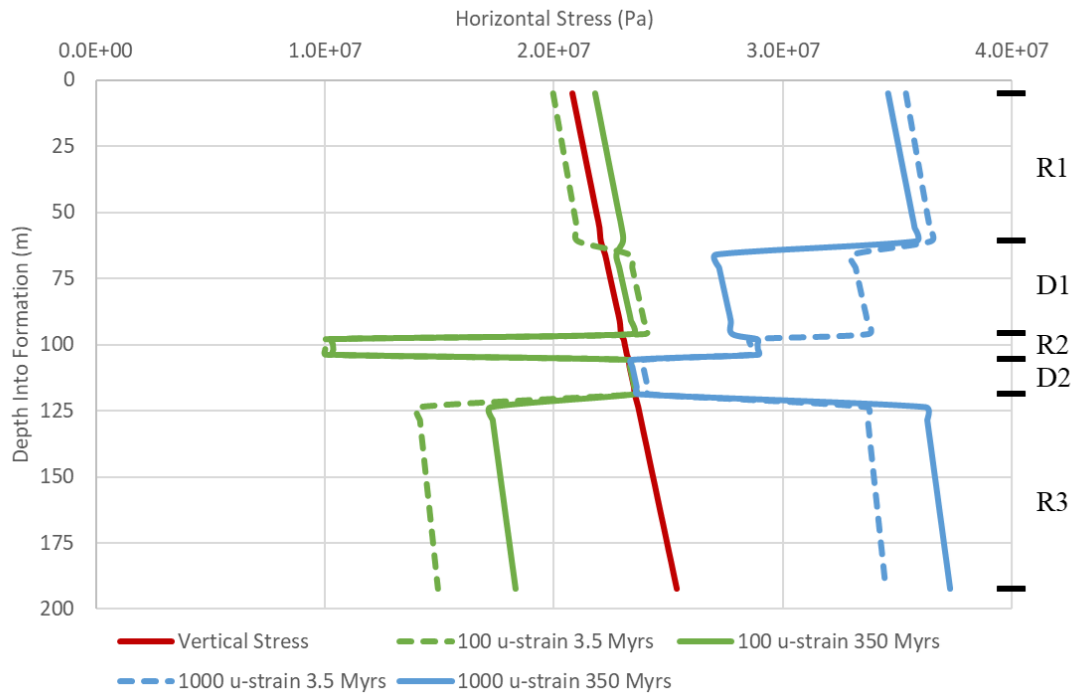


Figure 59 Final horizontal stresses influenced by tectonic strain and time, simulated for 350 million years (solid) and 3.5 million years (dashed)

Most of the differences between the magnitudes of tectonic strains remain the same regardless of the time frame those strains are applied over. The higher total strains of the 1000 μ strain model result in overall higher stresses compared to the 100 μ strain model. More interesting differences can be seen when examining the differences between the 350 and 3.5 million year models.

For the 100 μ strain model, the differences are minimal between the Ductile 2 and Reservoir 2 zones. There is a slight difference in Ductile 1, where the shorter time frame appears to limit the amount of relaxation the zone is able to undergo, resulting in an increase in predicted stress for this zone. Reservoir 1 has the opposite behavior, where the formation experiences less overall stress when the load is applied over a shorter period of time. Finally, Reservoir 3 shows

similar behavior to Reservoir 1, with an expected decrease in stress with a shorter simulated formation age.

Similar trends are seen in the 1000 μ strain model. Reservoir 3 again experiences lower stresses in the 3.5 million year model compared to the 350 million year model. Ductile 1 also has higher predicted stresses, though the difference is greater than the difference seen in the 100 μ strain model. Interestingly, Reservoir 1 shows higher overall stresses, possibly because the behavior has changed to being elasticity-driven. And again, there appears to be very little difference between the 350 and 3.5 million year models with respect to the behavior of Reservoir 2. Ductile 2 shows a slight increase in stress with the shorter time frame, which will be examined when reviewing the development of stresses over time.

Figure 60 demonstrates the development of stresses over time for the 100 μ strain model simulated for 3.5 million years.

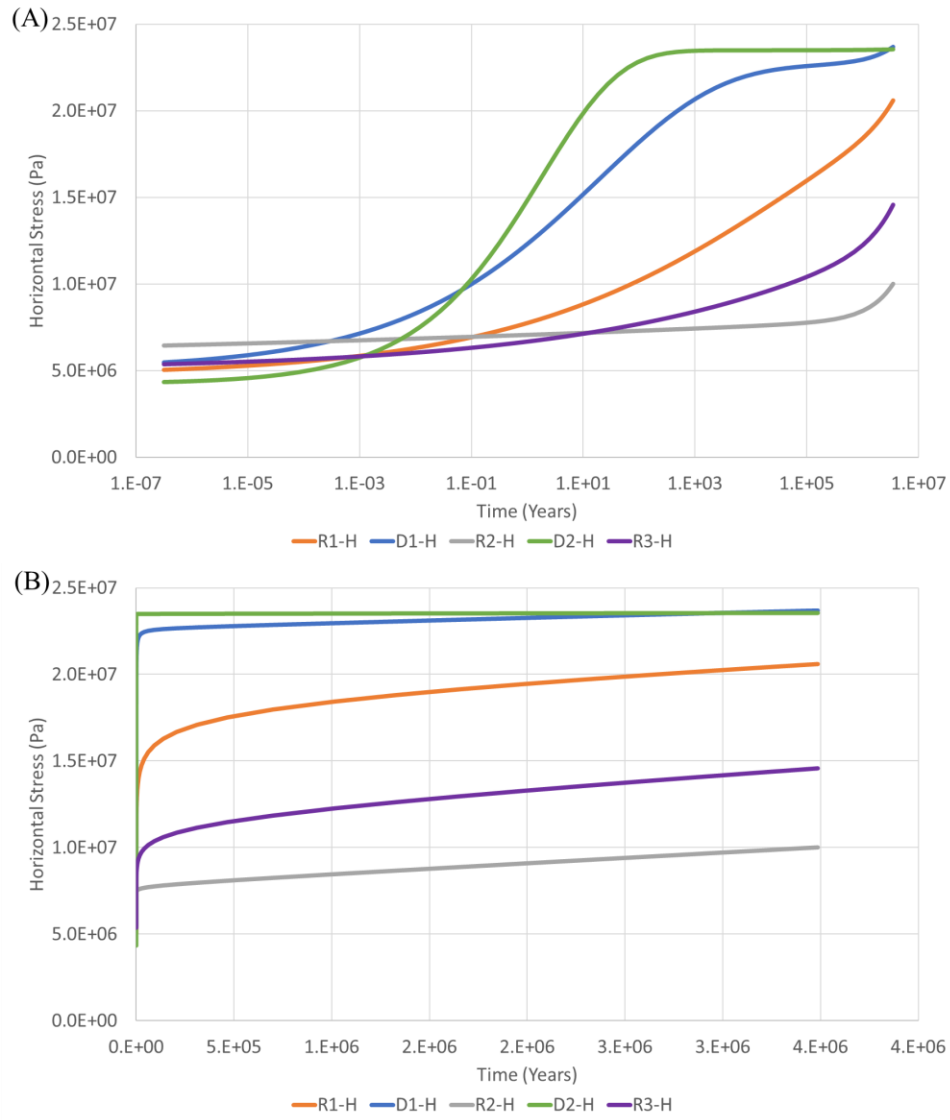


Figure 60 Stress development over time for 100 μstrain model simulated over 3.5 million years, (A) with logarithmic time scale and (B) with linear time scale

The trends seen in the 3.5 million year model resemble those of the 350 million year model. Ductile 1 and Ductile 2 appear to quickly relax, and the Reservoir zones clearly transition into elasticity-based behavior as the tectonic stress increases. The difference mainly lies in the faster increase in tectonic strains. For example, Ductile 2 barely spends any time in a relaxed state before transitioning to elasticity-based behavior as the tectonic strain quickly increases. Similarly, the

two Reservoir zones, which still show some relaxation, are also quicker to transition to purely elastic behavior.

A faster application of tectonic strain also emphasizes the differences in elastic behavior between the formations. There is significantly greater difference between the zones, and where with the longer time frame Reservoir 1 approached the stresses of the two ductile zones, for the shorter time frame the difference is more significant. Another trend of note is the faster transition to elasticity-based behavior of Ductile 2 shows the lower Ductile zone increasing to a stress above Ductile 1 before the end of the simulation. If the simulation were continued for a longer time period using the same rate of tectonic strain increase, this difference would be expected to become more significant.

Finally, Figure 61 examines the change in stress over time for the 1000 μ strain model with a simulated formation age of 3.5 million years.

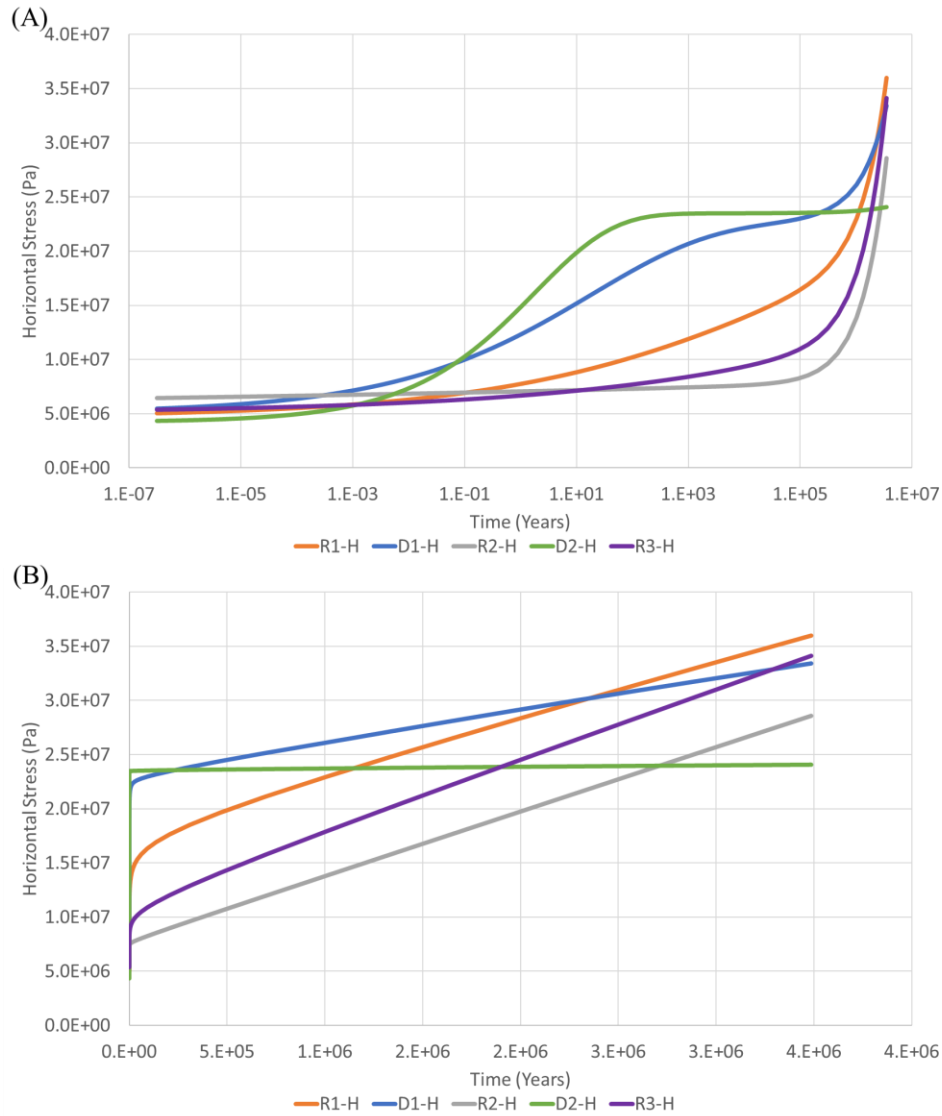


Figure 61 Stress development over time for 1000 µstrain model simulated over 3.5 million years, (A) with logarithmic time scale and (B) with linear time scale

As with the lower strain rate model, the trends are very similar between the 350 million year and 3.5 million year models. Here, the shorter time frame also corresponds to a faster transition to elastic behavior, and the Ductile 2 zone does not spend much time at a constant stress state before the increasing strain rate causes an increase in stress. The trend of increasing stresses over time is clearly seen in Figure 61(B). This also explains why the Reservoir 1 zone is expected

to have higher stresses than the Ductile 1 zone, as the faster increase in total strain of the 1000 μ strain model results in the faster increase in stress for Reservoir 1 compared to Ductile 1 due to their difference in elastic properties.

5.5.2.4 Conclusions of Finite Element Model

The finite element model has demonstrated the importance of accounting for not only tectonic strains, but also the relaxation of the model. At low strain values, the more creep-prone zones tend to increase in stress to a more lithostatic stress state. As the strain increases, a transition occurs and the formation changes from acting in a relaxation-driven behavior to elasticity-driven behavior. Results from these higher strain values correspond to the results as calculated from classical geomechanics, with zones less prone to creep increasing in stress quickly due to being relatively stiffer (higher Young's modulus). This transition between relaxation-driven and elasticity-driven behavior is easiest to see in the 1000 μ strain models, which are used to demonstrate exactly this behavior.

Based on the results from models with varying magnitudes of tectonic strains applied over widely different time scales, there is a threshold strain rate value for each formation. Below this threshold strain rate, the viscoelastic behavior of the formation allows the stress to relax, and the maximum stress will stay relatively constant once the formation has relaxed. Above the threshold strain rate, the formation cannot deform at a fast enough rate to prevent the building of stresses, and the behavior transitions to an essentially elastic behavior due to the applied strain rate. As the strain rate is related to the total strain and the time over which the strain is applied, there is essentially a threshold total strain value applied over a given period of time which is equivalent to the threshold strain rate.

When accounting for creep and relaxation, both the time frame of the applied tectonic stresses and the magnitude of the tectonic stresses must both be considered. A relatively higher magnitude strain applied over a shorter time will result in higher overall stresses, where the relative stresses can be more closely related back to differences in Young's modulus. Smaller strain rates, and rates applied over longer periods of time, allow the formation to relax and therefore result in overall lower stresses with some regions able to remain more relaxed due to higher tendencies to creep.

Most importantly, the model presented in this thesis unifies both the creep-based approach proposed by Sone and Zoback (2014a and 2014b) and the classical geomechanics modeling (see for example Eaton, 1969). The transition between the two is made as the strain increases and the model shifts from being relaxation-driven to being elasticity-driven.

5.6 Conclusions

Predicting the in-situ stresses in a formation is not as simple as applying a gradient based on density or depth. While equations such as the one proposed by Eaton (1969) are able to provide a lower-bound estimate of stress, it does not take into account factors such as the Young's modulus of the formation, the applied tectonic strains, or the age of the formation. A somewhat better method is demonstrated by Sone and Zoback (2014a and 2014b), which accounts for creep in the formation. This thesis develops and proposes a finite element model to predict the in-situ stresses, which accounts not only for the overburden pressure, but also for the elastic and creep properties of different regions of the formation when tectonic strains are applied. The result is a method

which unifies both approaches, as creep is more relevant at low strain conditions and elasticity overtakes the creep to become the dominant influence on in-situ stresses at higher strain values.

Depending on the method used, different zones are identified as barriers to fracture growth (where the stress in a given zone are higher than the stresses in surrounding zones) or as targets for stimulation (where the lower stresses will encourage fracture growth). By reviewing a small test matrix to examine the influence of both the magnitude of an applied tectonic strain and the time frame the tectonic strain is applied over, the finite element model is able to demonstrate the importance of accounting for both the elastic and creep behavior of a formation.

The application of the strain rate is very important for determining the relative stresses as it is related to the total strain applied to the formation. Regardless of if the strain rate was applied over 350 or 3.5 million years, applying a 1000 μ strain tectonic strain rate resulted in Reservoir 2 being noted as a zone of higher stress than Ductile 2. This means if the tectonic strains are of this magnitude, fractures initiated in Reservoir 2 will likely propagate down into Ductile 2. The opposite is true of the 100 μ strain models. In both the 350 and 3.5 million year models, the Reservoir 2 zone is seen as a target for stimulation, and the surrounding Ductile 1 and Ductile 2 zones will prevent fracture growth due to their relatively higher stress rates. This same switch in relative stresses is seen in Reservoir 3, where the 1000 μ strain case predicts this zone as having a higher stress than the overlying Ductile 2 zone, and the 100 μ strain case predicts the Ductile zone will have higher stress and act as a fracture barrier.

These are some of the examples of how the stresses vary with the application of tectonic strains and the time frame those strains are applied over. Higher total strains mean the formation will transition into an essentially elastic behavior. Slower application allows the formation to relax, resulting in lower overall stresses. This can clearly be seen in the 1000 μ strain case of

Ductile 2, where the 3.5 million year model has a much faster strain rate, resulting in Ductile 2 having higher stresses than Reservoir 2. By contrast, the 350 million year model predicts Ductile 2 will have lower relative stresses than Reservoir 2, meaning fractures initiated Reservoir 2 will grow preferentially in both the surrounding ductile zones.

While the exact tectonic strains may not be known for a formation, especially for an exploratory well, the age of a formation can typically be estimated. Knowing an approximate age of the formation, and a range of magnitudes likely for tectonic strains, the upper and lower bounds of the in-situ stresses for a formation could be predicted using a similar test matrix to the one used in this chapter. This will provide a more accurate prediction of in-situ stresses, and uncertainty could be resolved by performing a fracture test. During a fracture test the magnitude of stresses needed to initiate and propagate the fracture can be used to verify the stresses in this zone. If propagation can be mapped then the fracture growth can provide additional insight into what the exact in-situ stresses are based on the bounds provided by the model.

Most importantly, the model presented in this thesis demonstrates a method to include both relaxation-driven behavior, such as described in Sone and Zoback (2014a and 2014b), and classical geomechanics methods to predict stress, such as Eaton (1969). Low tectonic strain values correspond to more relaxation-driven behavior, where the more creep-prone zones experience greater stresses than less creep-prone zones. As the strains increase, the formation transitions to a more elasticity-driven behavior, and the stiffer zones less prone to creep overtake the creep-prone zones, leading to higher stresses. This transition in behavior, from relaxation-driven to elasticity-driven, is also the point when zones which were initially identified as barriers to fracture growth under relaxation are identified instead as potential targets for fracture growth. Again this

emphasizes the importance of accounting for both elastic and creep behavior as well as the applied tectonic strains when predicting the in-situ stresses of a formation.

The applications of this model include predicting induced seismicity due to fracturing or injection activities (Zoback and Hickman, 1982). As fracturing and injection can both cause changes in the stress field which induce seismicity, predicting the in-situ stresses prior to these activities can reduce the risk of inducing fault slipping in a critically stressed crust. The model presented here can also be used with the world stress map (“World Stress Map”, 2023) and properties determined from laboratory testing to estimate the behavior of different tectonic regions of the Earth’s crust and predict induced seismicity anywhere in the world. Induced seismicity is not only important during hydrocarbon extraction, but also in injection of wastewater, CO₂ sequestration, hydrogen storage, and enhanced geothermal systems, meaning this methodology is applicable to almost any activity involving changes in in-situ stresses surrounding a wellbore (Amemoutou et al., 2014, White and Foxall, 2015, Burtonshaw et al., 2022, and Zang et al., 2014).

6.0 Conclusions and Future Work

This thesis presents a characterization-to-prediction workflow for the Caney shale, starting with samples obtained from a core through the formation and ending with a three-dimensional finite element model to predict the in-situ stresses in the formation. Laboratory analysis demonstrated how, while there may be some conflicting results depending on the definition used, Brittleness Index is able to identify the mechanically weaker and more creep-prone “ductile” zones and differentiate them from the more brittle “reservoir” zones. Creep testing was used to provide a power-law description of creep, which can then be used to predict proppant embedment and fracture closure. Finally, a finite element model was created to predict the in-situ stresses in a layered formation which is able to predict the influence of tectonic strains and creep properties.

6.1 Brittleness Index

As discussed in Chapter 3.0, depending on the definition used to determine the brittleness index, a given zone may be deemed more or less brittle than the surrounding zones. For example, while the ductile zones were mechanically weaker than the reservoir zones, the ratio of unconfined compressive to tensile strength results in a brittleness index (BI_{strength}) of approximately the same value for all formations. However, despite the concern over the definitions of Brittleness Index, the identification of nominally “ductile” zones based on elastic properties from well logs did correlate to the layers which are weaker and more prone to creep. This shows there is a usefulness in identifying the formations using these methods, as the more creep-prone formations may act as

barriers to fracture growth. Meanwhile, the reservoir zones were identified as potential targets for stimulation, and these zones were identified as less prone to creep.

6.2 Creep Behavior

The experiments show there is a behavioral difference between the zones identified as “ductile” and “brittle”. This differentiation is made most striking when examining the creep behavior of the formations. The nominally ductile zones experience significantly greater creep than the nominally brittle reservoir zones. Additionally, the importance of bedding planes is clearly seen by the fact the vertical core plugs show more creep than horizontal core plugs, indicating accommodation of creep on bedding planes.

Using a power-law definition of creep behavior, modeling of proppant embedment and fracture closure demonstrate how important the creep properties are with respect to predicting hydrocarbon production. The more creep-prone zones experienced both greater predicted proppant embedment and fracture closure, and in the case of one simulation predicted complete closure of a fracture in the more creep-prone areas of the formation. As a fracture must remain open to allow for hydrocarbon flow, a decrease in the aperture of a fracture can have a significant impact on overall hydrocarbon production. Predicting long-term fracture opening size can help target zones which will have adequate aperture width to allow for hydrocarbon extraction.

6.3 Formation Stress Modeling

The models presented in Chapter 5.0 demonstrate the changes in predicted in-situ stress when both tectonic strain and creep properties are accounted for. Both factors significantly change the predicted in-situ stresses, causing the regions of the formation which may be thought to be targets for stimulation to become potential barriers to fracture growth. Similarly, the regions predicted to be barriers to fracture growth due to a relatively high Young's modulus and Poisson's ratio may experience significantly less creep deformation over time, and therefore when creep and applied tectonic strains are included in the stress prediction, these regions which were originally predicted to be barriers to fracture growth instead become targets for stimulation due to their relatively lower stress magnitudes.

This work presents a unified approach to calculate the power-law creep parameters using laboratory testing, and the implementation of those parameters in a finite element model to predict the in-situ stresses in a formation. This finite element model itself unifies models which include creep, such as the one presented by Sone and Zoback (2014a and 2014b), and classic geomechanics prediction of stresses, such as Eaton (1969).

Creep behavior significantly changes the stress profile when tectonic strains are below a threshold value. Below this threshold, the material is able to relax and the horizontal stress approaches a more lithostatic stress state as the horizontal stress approaches the vertical stress, while above the threshold the material behavior transitions into an elastic behavior driven by the rate of tectonic strain. The final magnitudes of the horizontal in-situ stresses depend not only on the applied tectonic strains, but also the rate those strains are applied, meaning depending on the conditions applied to the formation, a given zone may act more like a barrier to fracture growth or be identified as a target for stimulation. Additionally, most zones will change between having

more or less stress than their neighbors depending on the rate and duration of tectonic loading. This highlights the importance of creep testing and incorporating creep and elastic properties into a model as a way of constraining potential stress scenarios when planning stimulations so fractures will grow in the target zone and not propagate into other unwanted zones.

The model presented in this thesis is more accurate than the currently available models. It combines the relaxation-driven behavior described in the analytical model created by Sone and Zoback (2014a and 2014b) with the elasticity-driven behavior modeled by the work of Eaton (1969). Capturing this behavior, specifically the transition between relaxation-driven and elasticity-driven behavior, is the main advantage of the model presented in this thesis.

For reference, the input file used to generate the 100 μ strain model has been uploaded to the University of Pittsburgh D-Scholarship archive and is available at <http://d-scholarship.pitt.edu/id/eprint/45521>.

6.4 Workflow and Global Impact

During this thesis, a methodology has been presented going from the identification of a formation of interest to an accurate in-situ stress model which includes the mechanical behavior of the formation. Unconfined and triaxial testing provided the elastic properties for the model. Results from triaxial testing were also used to determine the appropriate loading for creep testing at 30% of the expected failure stress. Creep testing provided not only the relative proportions of elastic and plastic strains, but a 72-hour loading stage provided a method to predict the long-term deformation of the samples. The analysis of the creep compliance also provides a method to compare creep tests performed at widely varying conditions, allowing multiple zones in a

formation or entirely different formations to be compared. Finally, the in-situ stress model combined both the relaxation-driven behavior as determined through creep testing and the elasticity-driven behavior from triaxial testing to accurately predict the in-situ stresses in the formation.

This methodology and the accompanying in-situ stress model are applicable to any scenario where the in-situ stresses in a formation will be changed. Any time a well is drilled, the in-situ stresses in the formation will impact operations. This includes not only oil and gas wells but also CO₂ storage, injection of wastewater for disposal, and storage of hydrogen. Geothermal systems are also impacted by the in-situ stresses, meaning this method and model are also applicable to geothermal wells.

6.5 Closing Remarks

Identification of zones which will act as barriers to fracture growth or have lower stresses and will act as targets for preferential growth are key to predicting hydraulic fracture height. Ideally, fractures are located in zones which will produce hydrocarbons and are contained to those zones, not propagating into either unproductive zones or zones which produce unwanted products such as water which significantly complicates the production of an oil or gas well. Although it is recognized the prediction of in-situ stresses is critical, the knowledge base lacks a workflow of how to start with laboratory characterization of a formation and end with a model to predict in-situ stresses which accounts for both tectonic strains and creep behavior.

This thesis uses the Caney shale as an example to demonstrate a workflow to bridge the existing knowledge gap. Starting with laboratory characterization, this thesis presents a finite

element model which predicts the in-situ stresses based on the properties determined during laboratory testing. The novelty of this method is the unified in-situ stress model, which exhibits creep-driven behavior at low strains and elasticity-driven behavior at higher strains. Depending on which mechanism dominates the stresses in the model, a given zone may be identified as a barrier to fracture growth under one behavior regime and as a target for stimulation under a different regime. This work emphasizes how the characterization and modeling of both elastic and creep properties are essential to describe zones in layered rock formations as either low-stress targets for stimulation or high-stress barriers to fracture growth.

In addition to hydraulic fracturing, the methodology and stress prediction model presented in this thesis is applicable to any situation where stresses are changing around a wellbore. For example, the changes in the stress field during hydraulic fracturing are similar to the changes caused by injection of wastewater and CO₂. Other applications include geothermal wells and hydrogen storage wells. Essentially, this research is relevant for any activity involving a drilled well and the surrounding in-situ stresses.

6.6 Future Work

Using results from laboratory testing and modeling, the in-situ stresses and long-term deformation have been predicted. However, to further understand the behavior of the Caney shale and similar formations, several paths are recommended for future examination.

This study of the Caney shale has demonstrated the importance of measuring both mechanical and creep properties in the laboratory. By necessity, resources for laboratory testing are often limited, either in the number of available samples or with time or equipment restrictions.

Currently, the only viable method for testing creep is to load the sample in a load frame and monitor deformation and forces over long periods of time. This has the inherent issue of time restrictions. It is currently unreasonable to expect a creep test to run for months or years, but simulations and numerical models require extrapolating the results from a creep test lasting days out to time frames of hundreds of years or more. If a method could be developed to equate longer-term testing using different test conditions, it may be possible to develop a shorter test which would provide longer-term results, for example the testing of polymers at elevated temperature to simulate long time periods at lower temperatures (see for example Krauklis et al., 2019).

A specific area where future work needs to be focused is the improvement of in-situ stress modeling for formations. The built-in Abaqus finite element software allows for anisotropic elastic properties but requires isotropic creep behavior. Developing a method to allow for an anisotropic power-law description of creep deformation, or ideally a method which allows for any creep law to be modeled, would be extremely beneficial to future modeling of in-situ formation stresses.

In addition to anisotropic creep behavior, a more immediate recommendation would be to fracture test the Caney shale. Not only would this validate the in-situ stress for the model, but it would also provide insight into the relative stresses of the formations. As the model has demonstrated, both the magnitude and time frame of the tectonic strains influence if a given zone is identified as a barrier to fracture growth or a target for stimulation. The relative stresses of the identified zones in the Caney would provide insight into the exact tectonic strain conditions. This in turn would allow for refining of the model from the maximum and minimum bounding approach presented in this thesis to a more precise range.

Bibliography

Abaqus. 2011. Abaqus/CAE User Manual.

Alramahi, B. and M. Sundberg. 2012. Proppant embedment and conductivity of hydraulic fractures in shales. In 46th US Rock Mechanics/Geomechanics Symposium. American Rock Mechanics Association.

Amemoutou, A., Martínez-Garzón, P., Kwiatek, G., Rubinstein, J., and Bohnhoff, M. 2014. Earthquake Source Mechanisms and Stress Field Variations Associated With Wastewater-Induced Seismicity in Southern Kansas, USA. *Journal of Geophysical Research: Solid Earth*, 126.

ASTM D3967-08. 2008. Standard Test Method for Splitting Tensile Strength of Intact Rock Core Specimens. ASTM International.

ASTM D7012-14. 2014. Standard Test Methods for Compressive Strength and Elastic Moduli of Intact Rock Core Specimens under Varying States of Stress and Temperatures. ASTM International.

Awejori, G.A., Doughty, C., Spycher, N. Paronish, T., and Radonjic, M. 2022. Geochemical Reactions of Simple Fracturing Fluids with Caney Shale, *Energy Fuels* 2022, 36, 17, 10064–10081, August 22, 2022.

Awejori, G.A., Luo, G., Grider, C., Katende, A., Radonjic, M. Doughty, C., Spycher, N. Paronish, T. O'Connell, L. Rihn, A. 2021. Fracturing Fluid-Induced Mineralogy Changes and Impact on Elastic Properties for the Caney Shale, Oklahoma. Presented at the 55th US Rock Mechanics/Geomechanics Symposium, Houston, 18-25 June. ARMA-21-2004.

B. Cardott. 2017. Oklahoma Shale Resource Plays. *Oklahoma Geology Notes* 76 (2) 21-30.

- B. Eaton. 1969. Fracture Gradient Prediction and Its Application in Oilfield Operations. *Journal of Petroleum Technology* 21 (10), 1353-1360. SPE 2163.
- Bai, M. 2016. Why are brittleness and fracability not equivalent in designing hydraulic fracturing in tight shale gas reservoirs. *Petroleum* 2.1: 1-19.
- Bandara, K., Ranjith, P., and Rathnaweera, T. 2019. Improved understanding of proppant embedment behavior under reservoir conditions: A review study. *Powder Technology*, 352, 170-192.
- Bažant, Z. 1999. Size effect on structural strength: a review. *Archive of applied Mechanics* 69.9: 703-725.
- Bažant, Z., and Jirásek, M. 2018 *Creep and hygrothermal effects in concrete structures*. Vol. 225. Dordrecht, The Netherlands. Springer, 2018.
- Benge, M., Katende, A., Rutqvist, J., Radonjic, M., and Bungler, A. 2023. Creep Properties of Shale and Predicted Impact on Proppant Embedment for the Caney Shale, Oklahoma. *Rock Mechanics and Rock Engineering* (2023) 56: 5903-5921
- Benge, M., Lu, Y., Jones, J., Bungler, A., Haecker, A., Rihn, A., Crandall, D., Luo, G., and Radonjic, M. 2021a. Mechanical Properties of Nominally Ductile and Brittle Zones Within the Caney Shale Formation. American Rock Mechanics Association. 55th US Rock Mechanics/Geomechanics Symposium, Houston, Texas, June 20-23.
- Benge, M., Lu, Y., Katende, A., Rutqvist, J., Crandall, D., Haecker, A., King, G., Renk, J., Radonjic, M., and Bungler, A. 2021b. Connecting Geomechanical Properties with Potential for Proppant Embedment and Production Decline for the Emerging Caney Shale, Oklahoma. Unconventional Resources Technology Conference, Houston, Texas, July 26-28.

- Bourgoyne, A., Millheim, K., Chenevert, M., and Young, F. 1986. Applied Drilling Engineering. SPE Textbook Series, Volume 2.
- Brotons, V., Tomás, R., Ivorra, S., Grediaga, A., Martínez- Martínez, J., Benavente, D., and Gómez-Heras, M. 2016. Improved correlation between the static and dynamic elastic modulus of different types of rocks. *Materials and Structures*. 2016, 49(8): 3021-3037.
- Burtonshaw, J., Paluszny, A., Thomas, R., and Zimmerman, R. 2022. The influence of hydraulic fluid properties on induced seismicity during underground hydrogen storage. 56th US Rock Mechanics/Geomechanics Symposium, Santa Fe, New Mexico, June 26-29.
- Cardott, B. 2017. Oklahoma Shale Resource Plays. *Oklahoma Geology Notes* 76.2 (2017): 21-30.
- Coates, D. and R. Parsons. 1966. Experimental criteria for classification of rock substances. *International Journal of Rock Mechanics and Mining Sciences & Geomechanics Abstracts*. Vol. 3. No. 3. Pergamon, 1966.
- Deng, S., H. Li, G. Ma, H. Huang, and X. Li. 2014. Simulation of shale–proppant interaction in hydraulic fracturing by the discrete element method. *International Journal of Rock Mechanics and Mining Sciences* 70, 219-228.
- Eaton, B. 1969. Fracture Gradient Prediction and Its Application in Oilfield Operations. *Journal of Petroleum Technology* 21.10 (1969): 1353-1360.
- Economides, M., and Nolte, K. 1987. Reservoir Stimulation. Schlumberger Education Series. Dowell Schlumberger.
- Fadjarijanto, A., Rachmadi, A., Setiawan, A. S., Praptono, A., Suriyo, K., Simatupang, M., Pakpahan, O., Costam, Y. and Zakaria, Z. 2018. "Three Petrophysics Techniques Applied for the Thin Lamination Reservoir: The Impact towards Significant Reserve Addition."

Paper presented at the Offshore Technology Conference Asia, Kuala Lumpur, Malaysia, March 2018.

Frash, L., Hampton, J., Guitierrez, M., Tutuncu, A., Carey, J., Hood, J., Mokhtari, M., Huang, H., and Mattson, E. 2019. Patterns in Complex Hydraulic Fractures Observed by True-Triaxial Experiments and Implications for Proppant Placement and Stimulated Reservoir Volumes. *Journal of Petroleum Exploration and Production Technology* 9.4 (2019): 2871-2792.

Hajiabdolmajid, V., and P. Kaiser. 2003. Brittleness of rock and stability assessment in hard rock tunneling. *Tunnelling and Underground Space Technology* 18.1: 35-48.

Hetenyi, M. 1950. *Handbook of experimental stress analysis*. John Wiley. New York.

Hucka, V., and B. Das. 1974. Brittleness determination of rocks by different methods. *International Journal of Rock Mechanics and Mining Sciences & Geomechanics Abstracts*. Vol. 11. No. 10.

Itasca. 2011. *FLAC3D v5.0, Fast Lagrangian Analysis of Continua in 3 Dimensions, Users Guide*.

Jin, X., S. Subhash, J. Roegiers, and B. Zhang. 2014. Fracability evaluation in shale reservoirs-an integrated petrophysics and geomechanics approach. *SPE hydraulic fracturing technology conference*. Society of Petroleum Engineers.

Kainer, C., Guerra, D., Zhu, D., and Hill, A. 2017. A Comparative Analysis of Rock Properties and Fracture Conductivity in Shale Plays. Paper presented at the SPE Hydraulic Fracturing Technology Conference and Exhibition, The Woodlands, Texas, USA, January. SPE-184877.

- Kamann, P. 2006. Surface-to-subsurface Correlation and Lithostratigraphic Framework of the Caney Shale (Including the "mayes" Formation) in Atoka, Coal, Hughes, Johnston, Pittsburg, and Pontotoc Counties, Oklahoma, MS thesis. Oklahoma State University
- Katende A., Allen C., Rutqvist J., Nakagawa S., and Radonjic M. 2023. Experimental and numerical investigation of proppant embedment and conductivity reduction within a fracture in the Caney Shale, Southern Oklahoma, USA. *Fuel* 341, 127571 (2023).
<https://doi.org/10.1016/j.fuel.2023.127571>.
- Katende, A., O'Connell, L., Rich, A., Rutqvist, J., and Radonjic, M. 2021a. A Comprehensive Review of Proppant Embedment in Shale Reservoirs: Experimentation, Modeling and Future Prospects. *Journal of Natural Gas Science and Engineering*, 95, 104143 2021.
- Katende, A., Rutqvist, J., Bengte, M., Seyedolali A., Bungler, A., Puckette J.O., and Radonjic, M. 2021b. Convergence of Micro-Geochemistry and Micro-Geomechanics Towards Understanding Proppant Shale Rock Interaction: a Caney Shale Case Study in Southern Oklahoma, USA. *Journal of Natural Gas Science and Engineering*, 96, 104296 2021.
- Kovari, K., Tisa, A., Einstein, H. H., and Franklin, J. A. 1983. Suggested Methods for Determining the Strength of Rock Materials in Triaxial Compression: Revised Version. *Intl J of Rock Mech & Mining Sci & Geomechanic Abs*, 20(6).
- Krauklis, A., Akulichev, A., Gagani, A., and Echtermeyer, A. 2019. Time-Temperature-Plasticization Superposition Principle: Predicting Creep of a Plasticized Epoxy. *Polymers* 2019 (11) 1848.
- Kuruppu, M., Y. Obara, M. Ayatollahi, K. Chong, and T. Funatsu. 2014. ISRM-suggested method for determining the mode I static fracture toughness using semi-circular bend specimen. *Rock Mechanics and Rock Engineering* 47(1), 267-274.

- Lecampion, B. 2012. Modeling size effects associated with tensile fracture initiation from a wellbore. *International Journal of Rock Mechanics and Mining Sciences*: 56 67-76.
- Li, Y., and Ghassemi, A. 2012. Creep Behavior of Barnett, Haynesville, and Marcellus Shale. *46th US Rock Mechanics / Geomechanics Symposium 2012*, 1, 641–647.
- Lim, I., Johnston, I., Choi, S., and Boland, J. 1994. Fracture testing of a soft rock with semi-circular specimens under three-point bending. Part 1—mode I. In *International journal of rock mechanics and mining sciences & geomechanics abstracts* (Vol. 31, No. 3, pp. 185-197).
- Loucks, R. G., Reed, R. M., Ruppel, S. C., and Hammes, U. 2012. Spectrum of Pore Types and Networks in Mudrocks and a Descriptive Classification for Matrix-Related Mudrock Pores. *AAPG bulletin*, 96(6), 1071-1098.
- Martínez-Martínez, J., Benavente, D., and García-del-Cura, M. 2012. Comparison of the static and dynamic elastic modulus in carbonate rocks. *Bulletin of Engineering Geology and the Environment* (2012) 71: 263-268.
- Min, K., Rutqvist, J., Tsang, C., and Jing, L. 2004. Stress-dependent permeability of fractured rock masses: a numerical study. *International Journal of Rock Mechanics and Mining Sciences* 41.7 (2004): 1191-1210.
- Ming, C., S. Zhang., L. Ming, M. Xinfang, Z. Yushi, Z. Tong, L. Ning, and L. Sihai. 2018. Calculation method of proppant embedment depth in hydraulic fracturing. *Petroleum Exploration and Development* 45(1), 159-166.
- Nolte, K., and Smith, M. 1981. Interpretation of Fracturing Pressures. *Journal of Petroleum Technology* 33 (09): 1767-1775. SPE 8297.
- Pruess, K., Oldenburg, C., and Moridis, G. 2012. TOUGH2 User's Guide Version 2.1, Report LBNL-43134. Lawrence Berkeley National Laboratory, Berkeley, CA, USA.

- Radonjic, M., Luo, G., Wang, Y., Achang, M., Cains, J., Katende, A., Puckette, J., Grammer, M., and King, G. 2020. Integrated Microstructural Characterization of Caney Shale, OK. Presented at 2021 Unconventional Resources Technology Conference, Houston, 26-28 July. URTeC 2947.
- Rassouli, F., and Zoback, M. 2018. Comparison of Short-Term and Long-Term Creep Experiments in Shales and Carbonates from Unconventional Gas Reservoirs. *Rock Mechanics and Rock Engineering* 51: 1995 – 2014.
- Rickman, R., Mullen, M., Petre, E., Grieser, B., and Kundert, D. 2008. A Practical Use of Shale Petrophysics for Stimulation Design Optimization: All Shale Plays Are Not Clones of the Barnett Shale. Presented at the 2008 SPE Annual Technical Conference and Exhibition, Denver, Colorado, 21-24 September. SPE-115258.
- Roberts, J., Chapman, P., and Arrington, S. 2023. Temperature Effects on Core Mechanics Testing – An Eagle Ford Case Study. 57th US Rock Mechanics/Geomechanics Symposium, Atlanta, Georgia, 25-28 June, 2023. ARMA 23-0307.
- Rutqvist J. 2011. Status of the TOUGH-FLAC Simulator and Recent Applications Related to Coupled Fluid Flow and Crustal Deformations. *Computers & Geosciences* 37: 739–750.
- Rutqvist, J. 2017. An Overview of TOUGH-Based Geomechanics Models. *Computers & Geosciences* 108: 56–63.
- Sasaki, T., and Rutqvist, J. 2022. Effects of Time-Dependent Deformation of Shale on the Integrity of a Geologic Nuclear Waste Repository. *International Journal of Rock Mechanics and Mining Sciences* 158 (2022): 105206.
- Schad, S. 2004. Hydrocarbon Potential of the Caney Shale in Southeastern Oklahoma, MS thesis, University of Tulsa.

- Sone, H., and Zoback, M. 2014a. Time-dependent Deformation of Shale Gas Reservoir Rocks and its Long-Term Effect on the In Situ State of Stress. *International Journal of Rock Mechanics & Mining Sciences* 69 (2014) 120-132.
- Sone, H., and Zoback, M. 2014b. Viscous Relaxation Model for Predicting Least Principal Stress Magnitudes in Sedimentary Rocks. *Journal of Petroleum Science and Engineering* 124 (2014) 413-431.
- Thompson, J., Fan, L., Grant, D., Martin, R., Kanneganti, K., and Lindsay, G. 2010 An Overview of Horizontal Well Completions in the Haynesville Shale. Paper presented at the Canadian Unconventional Resources and International Petroleum Conference, Calgary, Alberta, Canada, October 2010.
- Voltolini, M., Rutqvist, J., and Kneafsey, T. 2021. Coupling Dynamic in Situ X-Ray Micro-Imaging and Indentation: A Novel Approach To Evaluate Micromechanics Applied To Oil Shale. *Fuel* 300: 120987.
- Vulgamore, T., Wolhart, S., Mayerhofer, M., Clawson, T. and Pope, C. 2008. Hydraulic Fracture Diagnostics Help Optimize Stimulations Of Woodford Shale Horizontals. *The America Oil&Gas Reporter* April 15 (2008).
- Wang, Y., Luo, G., Achang, M., Cains, J., Wethington, C., Katende, A., Grammer, G. M., Puckette, J., Pashin, J., Castagna, M., Chan, H., King, G. E., and Radonjic, M. 2021. Multiscale Characterization of the Caney Shale — an Emerging Play in Oklahoma. *Midcontinent Geoscience*, 2, 33–53.
- White, J. and Foxall, W. 2016. Assessing induced seismicity risk at CO₂ storage projects: Recent progress and remaining challenges. *International Journal of Greenhouse Gas Control* 49 (2016) 413-412.

- Wong, R., Schmitt, D., Collis, D., and Gutam, R. 2008. Inherent transversely isotropic elastic parameters of over-consolidated shale measured by ultrasonic waves and their comparison with static and acoustic in situ log measurements. *Journal of Geophysics and Engineering* 5.1 (2008): 103-117.
- “World Stress Map Project.” World Stress Map, November 4, 2023. www.world-stress-map.org
- Xiong F., Rother, G., and Radonjic, M. 2022. Insights into controls of mineralogy and pore structure on the density of adsorption phase in shales under supercritical conditions, *Energy Fuels* 2022, 36, 17, 10110–10122, August 22, 2022.
- Zang, A., Oye, V., Jousset, P., Deichmann, N., Gritto, R., McGarr, A., Majer, E., and Bruhn, D. 2014. Analysis of induced seismicity in geothermal reservoirs – An overview. *Geothermics* 52 (2014) 6-21.
- Zhang, J., Kamenov, A., Zhu, D., and Hill, A. 2014. Laboratory Measurement of Hydraulic-Fracture Conductivities in the Barnett Shale. *SPE Production & Operations* 29 (2014): 216-227.
- Zoback, M. and Hickman, S. 1982. In Situ Study of the Physical Mechanisms Controlling Induced Seismicity at Monticello Reservoir, South Carolina. *Journal of Geophysical Research* 87(B8): 6959-5974